Title
Cation order construction in cation-disordered rocksalt cathodes

Author
Cai, Zijian

Publication Date
2022

Cation order construction in cation-disordered rocksalt cathodes

By

Zijian Cai

A dissertation submitted in partial satisfaction of the

requirements for the degree of

Doctor of Philosophy

in

Engineering – Materials Science and Engineering

in the

Graduate Division

of the

University of California, Berkeley

Committee in charge:

Professor Gerbrand Ceder, Chair
Professor Mark Asta
Professor Bryan D. McCloskey

Fall 2022

Abstract

Cation order construction in cation-disordered rocksalt cathodes

by

Zijian Cai

Doctor of Philosophy in Materials Science and Engineering

University of California, Berkeley

Professor Gerbrand Ceder, Chair

Lithium-ion batteries have achieved tremendous success in energy storage with a broad range of application. The Li-ion industry is growing to 1TWh of production per year for which approximately one million tons of combined cobalt or nickel will be required. The increasing demand has imposed a large strain on nature resources. Compared to traditional commercialized layered $Li(Ni,Mn,Co)O_2$ (NMC) cathodes, which require expensive cobalt and nickel, the recent development of Li-excess cation-disordered rocksalt (DRX) cathodes widely broaden the possible chemical space from which to draw Li-ion cathodes, including some inexpensive and earth-abundant TMs such as Mn, Ti, Fe, V and Cr. Unlike the well-defined 2-D percolation pathway in layered NMC cathodes, the Li percolation in DRX structures relies on the 3-D quasi-randomly distributed 0-TM channels (no transition metal). Although long-range disordered, the DRX structure still contains short-range cation order (SRO), which has significant impact on Li percolation and electrochemical performance. Therefore, extensive research efforts are required to achieve a better understanding of the correlation between cation order and overall electrochemical performance. In this thesis, three strategies to modify local ordering in DRX cathodes, including metal doping on cation sublattices, synthesis condition control and cation partially order, were carefully evaluated by combining electrochemical tests, advanced characterizations and computational investigations.

The first part of the thesis will focus on the cation doping strategy to control the SRO and extractable Li in fluorinated DRX cathodes. Due to the 'locking effect' caused by strong bonding between Li and F, not all the Li can be extracted during charging, which compromises the electrochemical performance. A screening based on the bonding strength and ionic radius was performed to identify a suitable dopant to free the locked Li. Mg was chosen because of its large bonding energy with F and similar ionic radius with Li. A detailed theoretical investigation of Li–F SRO using DFT calculations and cluster expansion (CE) Monte Carlo (MC) simulations confirmed that Mg doping results in a greater fraction of extractable Li ions by reducing the frequency of the Li_6F configuration. We verified our hypothesis by comparing the electrochemical performance of $Li_{1.25}Mn_{0.45}Ti_{0.3}O_{1.8}F_{0.2}$ and $Li_{1.25}Mg_{0.1}Mn_{0.45}Nb_{0.2}O_{1.8}F_{0.2}$. Although both compounds have the same Li-excess and Mn content, the Mg-doped compound delivers higher capacity. Finally, we extended the discussion to a related group of compositions:

$Li_{1.333}Mn_{0.667}O_{1.333}F_{0.667}$ (LMF), $Li_{1.233}Mg_{0.1}Mn_{0.667}O_{1.333}F_{0.667}$ (ls-LMF), $Li_{1.333}Mg_{0.1}Mn_{0.567}O_{1.333}F_{0.667}$ (ms-LMF) and $Li_{1.28}Mg_{0.11}Mn_{0.61}O_{1.333}F_{0.667}$ (ls-LMF) to demonstrate that increased accessible Li, enabled by Mg doping, can also be traded for an improvement of cycle life. The results showed that Mg-doping should be considered in fluorinated DRX cathodes to optimize the performance.

The second part of the thesis reports on the solid-state synthesis mechanism of DRX compounds. The synthesis mechanism of a typical DRX oxyfluoride, $Li_{1.2}Mn_{0.55}Ti_{0.25}O_{1.85}F_{0.15}$ (LMTF), are characterized to investigate the formation of long-range order and short-range order. Experimentally, the formation of long-range disorder followed by short-range order during the synthesis was clearly demonstrated through *in-situ* transmission electron microscopy, *ex-situ* X-ray diffraction and pair distribution function analysis. This phenomenon is further explored by performing *ab initio* calculations for the formation energy of DRX with random structure and with SRO to estimate the reaction kinetics. Based on both experiment and computational results, the SRO feature can be eliminated by simply shortening sintering time and quenching from high temperature. With this strategy, the SRO-free LMTF (35 min) sample exhibited a capacity of >310 mAh g^{-1} and a specific energy close to 1000 Wh kg^{-1} and enabled discharge up to 2 A g^{-1}, which is much better than SRO-rich LMTF (4h).

The third part of the thesis identifies the cation to anion ratio in synthesis as a key parameter for tuning the structure continuously from a well-ordered spinel, through a partially ordered spinel, to a rocksalt. A series of well selected partially-(dis)ordered spinel cathodes with different degrees of cation over-stoichiometry, $Li_{1.4+x}Mn_{1.6}O_{3.7}F_{0.3}$ (x = 0.07, 0.28, and 0.6), was synthesized via a mechanochemical method. The degree of cation disorder continuously varies with cation to anion ratio, which modifies the voltage profile, rate capability, and charge-compensation mechanism in a rational and predictable way. The results indicate that spinel-type order is most beneficial for achieving high-rate performance as long as the cooperative Li migration from 8a to 16c sites is suppressed. We also found that more rocksalt-like disorder facilitates O redox, which can increase capacity. These findings reveal an important tuning handle for achieving high energy and power in the vast space of partially ordered cathode materials.

Table of Contents

List of figures

Figure 1-1. Common rocksalt-type lithium transition metal oxide crystal structures: (a) the disordered rocksalt α -$LiFeO_2$ structure in which all cation sites are equivalent, (b) the layered α-$NaFeO_2$ structure, (c) the spinel-like low-temperature $LiCoO_2$ structure, small gray and black filled circles stand for lithium and transition metal sites, respectively.

Figure 1-2. Average discharge potential (V vs. Li^+/Li) and gravimetric capacity (mAh/g) of selected layered and DRX cathodes. Contour lines represent the gravimetric energy density (Wh/kg). NMCA = NMC (Li-Ni-Mn-Co-O_2) and NCA (Li-Ni-Co-Al-O_2).

Figure 1-3. Natural abundance (blue bars) and price (orange bars) of selected *3d* and *4d* transition metal elements found in disordered lithium transition metal oxide cathodes (on a log scale). The metal price for V, Ti, Nb and Mo was obtained from the metal oxide price, by accounting for the weight fraction of the transition metal element. The oxide precursor cost is more relevant for cathode production, and for some metals, such as Ti, the oxide precursor price is considerably lower than the metal price due to the high cost of extracting the metal from the oxide. However, it is difficult to obtain consistent data for the relevant ores, which is why we have listed the metal price directly obtained from our sources for Mn, Co, Ni, Cr, Fe and Zr. The compositional space of layered oxides is enclosed in a dashed black rectangle, while d^0 species favoring cation disorder (V^{5+}, Ti^{4+}, Zr^{4+}, Nb^{5+} and Mo^{6+}) are enclosed in a solid black rectangle.

Figure 1-4. Li^+ diffusion between neighboring O_h sites in rocksalt-type Li_xTMO_2 takes place via an intermediate T_d site (*o-t-o* diffusion). (a) Layered Li_xTMO_2 compounds exhibit 1-TM and 3-TM T_d sites, corresponding to Li_3TM and $LiTM_3$ clusters, respectively. 1-TM channels are responsible for Li^+ diffusion. (b) Li migration barriers for hops between neighboring O_h sites in layered Li_xTMO_2 are very sensitive to the occupancy of sites adjacent to the intermediate T_d site of the hop. The barrier for hops into isolated vacancies is significantly larger than for di-vacancy hops. Adapted from Van der Ven et al. [1] (c) Cation disorder results in the formation of all types of tetrahedral clusters (0-TM, 1-TM, 2-TM, 3-TM and 4-TM channels). In this case, 0-TM channels (and, to some extent, 1-TM channels) are responsible for Li^+ conduction.

Figure 1-5. Calculated Li migration barriers along 1-TM channels (red squares: one Mo^{4+} neighbor; blue triangles: one Cr^{3+} neighbor), and along 0-TM channels (black circles) as a function of the average tetrahedron height in model disordered Li_2MoO_3 and $LiCrO_2$ structures. Error bars represent standard deviations and the shaded area highlights the typical range of tetrahedron heights in disordered materials.

Figure 1-6. (a) Critical lithium concentrations (x_C) for 0-TM Li percolation, and (b), (c), (d) for one Li per formula unit (1 Li/f.u.) to be accessible via 0-TM channels as a function of the overall lithium content and the degree of cation mixing in $Li_xTM_{2-x}O_2$ compounds with the layered (α-$NaFeO_2$), spinel-like (LT-$LiCoO_2$) and γ -$LiFeO_2$ structure. Structure-specific x_C values are indicated by a thick black contour line. Compositions falling to the left of these contour lines are not 0-TM percolating. Thin lines indicate the compositions at which 1 Li/f.u. becomes 0-TM accessible.

Figure 1-7. (a) Comparison of room temperature and 50°C galvanostatic cycling data for $Li_{1.2}Mn_{0.4}Zr_{0.4}O_2$ (top panel) and $Li_{1.2}Mn_{0.4}Ti_{0.4}O_2$ (bottom panel). (b) Electron diffraction patterns of (i) $Li_{1.2}Mn_{0.4}Ti_{0.4}O_2$ and (iii) $Li_{1.2}Mn_{0.4}Zr_{0.4}O_2$ along the [100] zone axis. The round spots are indexed to the $Fm\bar{3}m$ space group, while the diffuse scattering patterns around the spots are attributed to SRO. Several intensity maxima in the diffuse scattering pattern of $Li_{1.2}Mn_{0.4}Zr_{0.4}O_2$ are highlighted with yellow arrows. Simulations of electron diffraction patterns for (ii)

4 h. Peaks from small amount of unreacted Li_2CO_3 and LiF precursors are marked by triangles and asterisks, respectively. (B) sPDF fitting results of samples sintered at 1000°C for 5 min (upper panel), 35 min (middle panel), and 4 h (lower panel) using a random structure. The experimental data are plotted as black open circles, the fittings are plotted as solid red lines, and the difference between observation and calculation is plotted as solid green lines. (C) Summary of R_w factors obtained from each PDF fitting at various stages of the synthesis. The synthesis profile is also overlaid, with red circles marking the points of data collection. The grey dashed lines are displayed to guide the eye.

Figure 3-4. Additional sPDF fitting results of LMTF samples collected at different stages during the synthesis. SPDF fitting results of samples (A) ramped to 900 °C; (B) ramped to 1000 °C without holding; and (C–D) ramped to 1000 °C followed by holding for (C) 15 min and (D) 1 h using a random DRX structure (without SRO). The experimental data are plotted as black open circles, the fittings are plotted as solid red lines, and the difference between observation and calculation is plotted as solid green lines. The sample sintered for 1 h (Fig. D) shows a larger deviation from a random structural model, as demonstrated by the larger R_w factor relative to those of the rest of the samples, which mainly originates from the small *r* value region between 1.8 and 4.5 Å. This suggests the growth of SRO upon extended heating during the synthesis.

Figure 3-5. Schematic of the reaction energy in the LMTF synthesis process. The grand potential evolution of the total system is computed *ab initio* for the random rocksalt and the short-range ordered rocksalt (simulated at 1273 K), and schematically interpolated (with dashed line). Note that two different energy scales are used (separated at −4.5eV) to highlight the small energy decrease in the SRO formation.

Figure 3-6. Thermogravimetric analysis results during the synthesis of LMTF. The red curve shows the weight change of the precursors upon heating, and the green curve is the heating profile. A ramping rate of 5°C min^{-1} was applied followed by a 4-h holding at 1000°C in an Ar atmosphere. The weight of the powder barely changed after heating at 1000°C for approximately 35 min.

Figure 3-7. SEM images of as-obtained (A) LMTF (35 min) and (B) LMTF (4 h) and shaker-milled (C) LMTF (35 min) and (D) LMTF (4 h) with carbon black. Both samples had similar particle sizes both as-obtained (5–20 µm) and after ball-milling (200–400 nm).

Figure 3-8. Particle size analyses of LMTF (35min) and LMTF (4h). SEM images of as-synthesized (A) LMTF (35min) and (C) LMTF (4h). SEM images of shaker-milled (B) LMTF (35min) and (D) LMTF (4h) without carbon black. Statistical analyses of the particle sizes of (E) LMTF (35min) and (F) LMTF (4h) obtained from Figures (A)-(D), which confirm that LMTF (35min) and LMTF (4h) are similar in particle size both at as-synthesized state and after shaker-mill.

Figure 3-9. *Ex situ* TEM ED patterns. ED patterns were collected for (A) LMTF (35 min) and (B) LMTF (4 h) along the [100] zone axis. The round spots, which originate from the LRO in the materials, are indexed to the Fm-3m space group. The square-like diffuse scattering patterns are attributed to the SRO. Quantifications of the SRO pattern intensity by integrating the counts within the dashed rectangular regions are displayed next to the ED patterns. It can be observed that LMTF (35 min) has significantly less SRO than LMTF (4 h), which further supports our *in situ* observation.

Figure 3-10. Lab XRD patterns and Rietveld refinement of the as-synthesized and shaker-milled LMTF. (A) as-synthesized and (B) shaker-milled LMTF (35min); (A) as-synthesized and (B) shaker-milled LMTF (4h). ZrO_2 phase observed in the shaker-milled samples is from the Spex mill jar and balls. It can be observed that the lattice constant of both materials remains almost

shown in red dots, calculated pattern in black line, difference curve in blue line and Bragg position in olive vertical bars.

Figure 4-6. SEM, STEM/EDS and HRTEM/ED of two partially-(dis)ordered spinel compounds. SEM images of the as-synthesized (a) $Li_{1.47}Mn_{1.6}O_{3.7}F_{0.3}$ and (b) $Li_2Mn_{1.6}O_{3.7}F_{0.3}$ (scale bars, 200 nm). STEM images and EDS mapping of the elements Mn, O and F (c) $Li_{1.47}Mn_{1.6}O_{3.7}F_{0.3}$ and (d) $Li_2Mn_{1.6}O_{3.7}F_{0.3}$ (scale bars, 30 nm). HRTEM images of (e) $Li_{1.47}Mn_{1.6}O_{3.7}F_{0.3}$ and (f) $Li_2Mn_{1.6}O_{3.7}F_{0.3}$ (scale bars, 10 nm). Insets: ED patterns (scale bars, 5 nm^{-1}). The selected area electron diffraction patterns can be indexed to a spinel lattice, with the *d* spacings measured to be 4.8, 2.5, 2.1, 1.6, 1.5, 1.2 and 1.0 Å.

Figure 4-7. Scanning electron microscope (SEM) images of (a) $Li_{1.47}Mn_{1.6}O_{3.7}F_{0.3}$ and (b) $Li_2Mn_{1.6}O_{3.7}F_{0.3}$ which shows the agglomeration of primary particles into secondary particles (scale bars, 1 μm).

Figure 4-8. ssNMR spectra obtained on the as-synthesized partially-(dis)ordered spinel materials. (a) ^{19}F ssNMR spectra obtained by summing multiple spin echo sub-spectra acquired at different excitation frequencies to ensure homogeneous excitation of the broad lineshape. For comparison, a ^{19}F spectrum collected on LiF powder is overlaid. (b) ^7Li spin echo (line) and pj-MATPASS (shaded, for clarity) ssNMR spectra of the as-synthesized materials. All spectra are scaled according to the moles of Li in the rotor and number of scans. The asterisks indicate the spinning sidebands.

Figure 4-9. Galvanostatic charge and discharge performance. (a) voltage profile during first cycle and the second charge of $Li_{1.47}Mn_{1.6}O_{3.7}F_{0.3}$ (black dash dot), $Li_{1.68}Mn_{1.6}O_{3.7}F_{0.3}$ (blue dot) and $Li_2Mn_{1.6}O_{3.7}F_{0.3}$ (red dash). (b) Corresponding dQ/dV curves when cycled between 1.5 and 4.8 V at 50 mA g^{-1}.

Figure 4-10. Galvanostatic cycling performance. Voltage profiles during the first 5 cycles of (a) $Li_{1.47}Mn_{1.6}O_{3.7}F_{0.3}$, (b) $Li_{1.68}Mn_{1.6}O_{3.7}F_{0.3}$, and (c) $Li_2Mn_{1.6}O_{3.7}F_{0.3}$. The initial discharge capacity, energy density and average discharge voltage are denoted in each figure. Capacity retention and Coulombic efficiency over 30 cycles of (d) $Li_{1.47}Mn_{1.6}O_{3.7}F_{0.3}$, (e) $Li_{1.68}Mn_{1.6}O_{3.7}F_{0.3}$, and (f) $Li_2Mn_{1.6}O_{3.7}F_{0.3}$, in two voltage ranges, 1.5 – 4.8V (red open squares) and 2 – 4.4 V (blue open circles).

Figure 4-11. Operando DEMS results for (a) $Li_{1.47}Mn_{1.6}O_{3.7}F_{0.3}$ and (b) $Li_2Mn_{1.6}O_{3.7}F_{0.3}$. Voltage profile, amount of O_2 and CO_2 evolved during the first cycle are shown in black solid lines, red dots and blue dots. The current density for galvanostatic cycling during the operando DEMS is 0.1 f.u. of Li^+ h^{-1} (i.e. 16.44 mA g^{-1} for $Li_{1.47}Mn_{1.6}O_{3.7}F_{0.3}$ and 16.08 mA g^{-1} for $Li_2Mn_{1.6}O_{3.7}F_{0.3}$).

Figure 4-12. Structural and electrochemical characterization of mechanochemically synthesized $LiMn_2O_4$. (a) XRD pattern of the as-synthesized $LiMn_2O_4$, with peaks matching the expected Bragg positions for a cubic $LiMn_2O_4$ spinel. (b) Electron diffraction pattern of the as-synthesized $LiMn_2O_4$. Scale bar, 5/nm. The selected area electron diffraction patterns can be indexed to a spinel lattice, with the *d* spacings measured to be 4.8, 2.5, 2.1, 1.6, 1.5, 1.2 and 1.0 Å. (c) Voltage profiles during the first 5 cycles for $LiMn_2O_4$. The initial discharge capacity, energy density and average discharge voltage are denoted.

Figure 4-13. Rate capability measurements. (a) Galvanostatic voltage profiles of (top to bottom) $LiMn_2O_4$, $Li_{1.47}Mn_{1.6}O_{3.7}F_{0.3}$, $Li_{1.68}Mn_{1.6}O_{3.7}F_{0.3}$, $Li_2Mn_{1.6}O_{3.7}F_{0.3}$, and $Li_{2.4}Mn_{1.6}O_{3.7}F_{0.3}$ at various rates, from 100 to 7,500 mA g^{-1}. (b) Ragone plot comparing the specific energy and power. The loading density of the cathode films was 2-3 mg cm^{-2}, containing 70 wt% active materials, 20 wt% carbon black and 10 wt% Teflon.

List of figures and tables

Acknowledgement

First of all, I would like to thank my Ph.D. advisor, Professor Gerbrand Ceder, for his continuous guidance and support during my graduate study. I truly appreciate his enthusiasm, immense knowledge, and patience. This thesis cannot be possible without his encouragement and his faith in me.

I would also like to thank my qualifying exam and dissertation committee members, Professor Mark Asta, Professor Bryan McCloskey, Professor Mary Scott and Doctor Wanli Yang. Thank you for your invaluable time and help for my research.

The help and company from my mentors in CEDER Group, Professor Zhengyan Lun and Professor Huiwen Ji, can never be appreciated enough. It is my great honor to learn from them and work with them. I appreciate all the inspiring conversations we had. Special thanks to Professor Zhengyan Lun for his guidance even starting from the first year of my undergraduate school.

I want to thank my collaborators in the CEDER Group, Prof. Zhengyan Lun, Prof. Huiwen Ji, Prof. Bin Ouyang, Prof. Raphaële Clément, Prof. Alex Urban, Prof. Mary Scott, Dr. Yan Zeng, Dr. Deok-Hwang Kwon, Dr. Haegyum Kim, Dr. Hyunchul Kim, Dr. Tina Chen, Dr. Jingyang Wang, Dr. Guobo Zeng, Peichen Zhong, Xinye Zhao, Yingzhi Sun, Yu Chen, Han-Ming Hau, Tucker Holstun, Zheren Wang and Nathan Szymanski, as well as those outside the group, Professor Bryan McCloskey, Dr. Mahalingam Balasubramanian, Dr. Yang Ha, Dr. Jue Liu, Dr. Wanli Yang, Dr. Raynald Giovine, Dr. Linze Li, Dr. Dr. Chongmin Wang, Dr. Yaqian Zhang, Dr. Krishna Prasad Koirala, Dr. Lu Ma, Tzu-Yang Huang and Emily E. Foley.

I am grateful to have all my friends who help me go through the tough moments during the past five years. In particular, I would like to thank Fei Wang for her company, accepting all aspects of me and being my best friend. Thanks to my peer, Yu Chen and Chuanhao Wang, for the joy they brought me. I also feel fortunate to meet many new friends at Berkeley. Thank you all for making my life at Berkeley enjoyable and memorable.

Finally, I want to thank my father and grandmother for their unconditional love and encouragement. Although from a small town, my family always give me the best they can to support my education.

Chapter 1 Introduction

1.1 Motivation

The tremendous growth of lithium-based energy storage has put new emphasis on the discovery of high-energy-density cathode materials. Although state-of-the-art layered Li(Ni,Mn,Co)O_2 (NMC) cathodes achieve good power and energy density, further improvements in these type of materials are limited. In addition, fully electrifying the current light-duty vehicle fleet of 1.3 billion cars with 60-100 kWh batteries with current technologies requires tens of megatonnes of Ni and Co, yet current supply for all use is ~ 2.5 Mt and ~140 kt per year, respectively. [2,3] Layered cathodes are limited to Ni, Co and Mn as they are very few transition metals that do not migrate to Li sites when a large amount of Li is removed from the structure upon charge. [4] Therefore, new cathodes with high volumetric and gravimetric energy density made from earth-abundant materials are crucial to sustain further growth in Li-ion battery field. Therefore, major global research efforts are aiming to reduce and even eliminate Co and Ni from cathodes compositions.

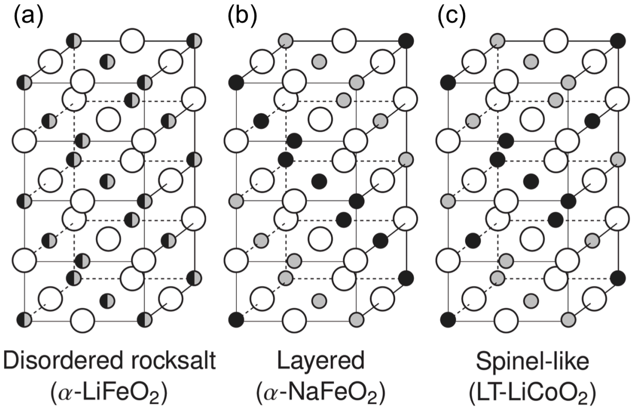

Figure 1-1. Common rocksalt-type lithium transition metal oxide crystal structures: (a) the disordered rocksalt α -$LiFeO_2$ structure in which all cation sites are equivalent, (b) the layered α-$NaFeO_2$ structure, (c) the spinel-like low-temperature $LiCoO_2$ structure, small gray and black filled circles stand for lithium and transition metal sites, respectively. Adapted from Urban et al.[22]

In the layered structure with formula unit $LiTMO_2$ (TM = transition metals), oxygen atoms occupy the sites of a face-centered cubic (FCC) lattice, and the cations (lithium and other metals atoms) occupy the FCC sub-lattice of octahedral interstices in an ordered way so that Li and TM ions segregate into layers in the (111) direction to form the α-$NaFeO_2$ structure (**Figure 1-1b**). In such layered structure, there is no intermixing between the Li and the TM sublattice, which is generally considered important for obtaining high-capacity cathodes materials with good cycle life. [5,6] The spinel-like low temperature structure of $LiCoO_2$ (**Figure 1-1c**), where Li and TM segregate into 16c and 16d sites, is another example that shows the importance of cation order and Li/TM segregation. For decades, cation disorder, where the Li and TMs mix on each other's position in the layered or spinel $LiTMO_2$ structure, has been considered detrimental to Li^+ transport, hence to the reversible capacity of intercalation-type electrodes.[7] Indeed, several cation-disordered rocksalt (DRX) cathodes, with a disordered arrangement of Li and M on the cation lattice (**Figure 1-1a**), have been made and show limited reversible capacity. [8] However, recent theoretical and experimental studies have demonstrated the feasibility of DRX cathodes. [9-44] This finding is important as it broadens the chemical space in which cathode materials can be designed. The criteria for DRX to be feasible cathodes will be discussed in **Section 1.2**.

Rather than leading to performance degradation, intrinsic cation disorder in DRX cathodes results in small and isotropic volume change on Li insertion/extraction. It can also remedy issues related to structural degradation upon cycling. **Figure 1-2** compares the performance of representative DRX and layered cathodes, in terms of average working potential, gravimetric capacity and energy density. Compared to commercial layered cathodes, including NMC, $Li(Ni,Co,Al)O_2$ (NMC) and standard $LiCoO_2$ (LCO), the capacity and energy density of DRXs is at least as good or superior.

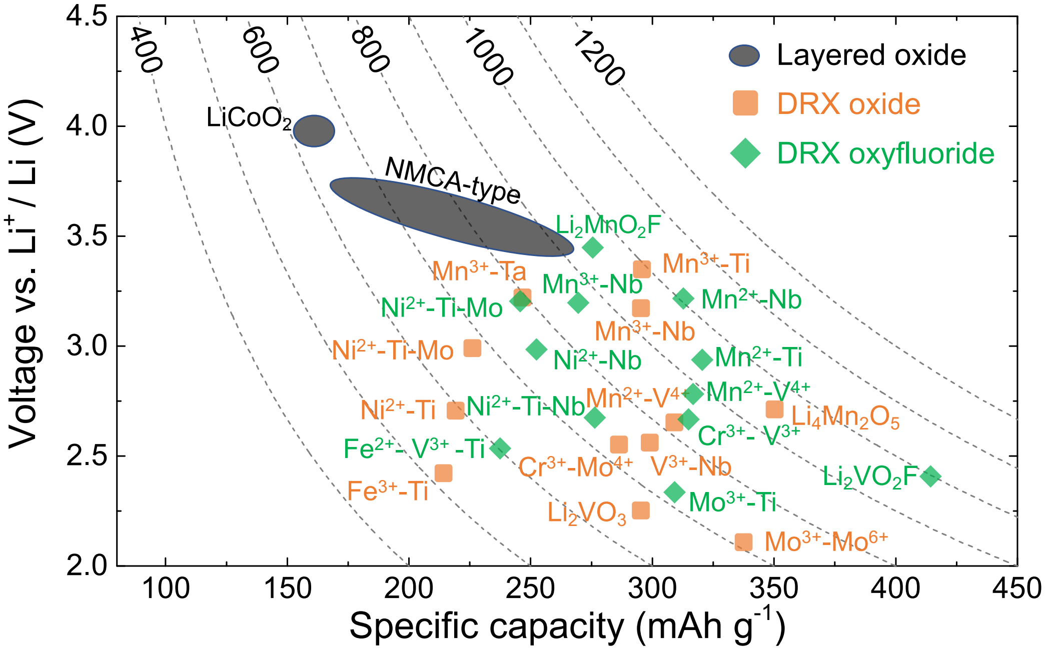

Figure 1-2. Average discharge potential (V vs. Li^+/Li) and gravimetric capacity (mAh/g) of selected layered and DRX cathodes. Contour lines represent the gravimetric energy density (Wh/kg). NMCA = NMC (Li-Ni-Mn-Co-O_2) and NCA (Li-Ni-Co-Al-O_2).

The discovery of DRXs as candidate Li-ion cathode materials enables the use of a large range of 3d and 4d metals, including those species which, in layered structure, are prone to migrate from the transition metal layers to octahedral (O_h) and Tetrahedral (T_d) sites in the interlayer space during electrochemical cycling and thereby impede Li^+ diffusion. The natural abundance and metal price of selected transition metal species present in DRX compounds reported to date is shown in Figure 1-3. It is clear that DRXs based on earth-abundant Mn, Fe and Ti are promising candidate in terms of sustainability and cost.

However, DRXs are not nearly as well optimized as currently commercialized cathode materials. A better insight into the relation between chemistry, structure and performance is required in order to create competitive DRX cathodes.

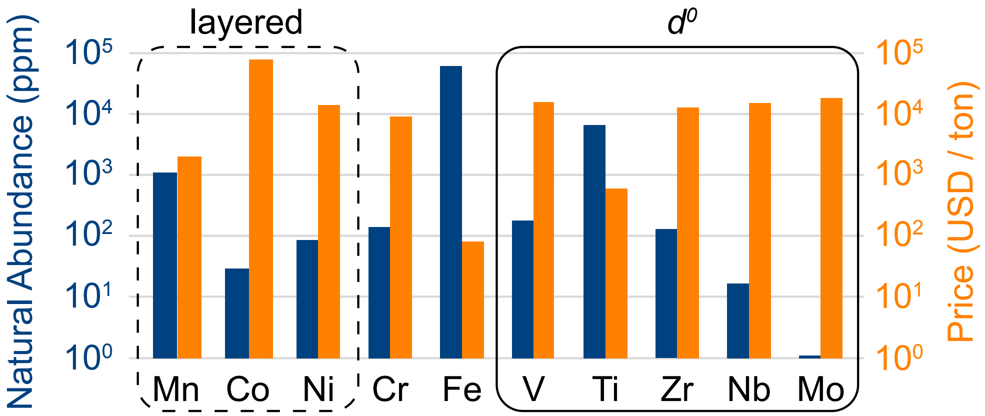

Figure 1-3. Natural abundance (blue bars) and price (orange bars) of selected *3d* and *4d* transition metal elements found in disordered lithium transition metal oxide cathodes (on a log scale). The metal price for V, Ti, Nb and Mo was obtained from the metal oxide price, by accounting for the weight fraction of the transition metal element. The oxide precursor cost is more relevant for cathode production, and for some metals, such as Ti, the oxide precursor price is considerably lower than the metal price due to the high cost of extracting the metal from the oxide. However, it is difficult to obtain consistent data for the relevant ores, which is why we have listed the metal price directly obtained from our sources for Mn, Co, Ni, Cr, Fe and Zr. The compositional space of layered oxides is enclosed in a dashed black rectangle, while d^0 species favoring cation disorder (V^{5+}, Ti^{4+}, Zr^{4+}, Nb^{5+} and Mo^{6+}) are enclosed in a solid black rectangle. Sources: www.webelements.com; www.metalary.com (accessed Aug. 2019); U.S. Geological Survey 2019[24].

1.2 Li transport in DRX cathodes

In a FCC anion framework, Li^+ diffuses between two O_h sites via an intermediate T_d site, hereafter referred to as *o-t-o* diffusion. [1,45-47] Both the size of the T_d site and the electrostatic interaction between Li^+ in the activated T_d site and the four cations in face-sharing O_h (**Figure 1-4**), forming a so-called 'tetrahedral cluster', have a strong impact on the Li^+ diffusion barrier. [48,49] When the cation lattice is filled with Li and TM species, five types of T_d clusters can be present: Li_4, Li_3TM, Li_2TM_2, $LiTM_3$ and TM_4 (**Figure 1-4c**). *o-t-o* Li^+ diffusion requires that at least two O_h Li are connected via the activated T_d site, which excludes LiM_3 and M_4 environments. The remaining two face-sharing O_h sites determine whether diffusion channels are open (low barrier) or closed (high barrier), which are hereafter referred to as 'gate sites'. [34]

In cation ordered stoichiometric layered $LiTMO_2$ and Li-rich layered $Li_{1+x}TM_{1-x}O_2$, there are two types of gate sites: $LiTM_3$ clusters (3-TM channels) in the TM slabs are not involved in Li^+ diffusion, while Li_3TM clusters (1-TM channels) in the Li slabs support the Li^+ migration (**Figure 1-4a**). The size of the activated T_d site is controlled by the layer spacing of the Li slab, [48,49] which is primarily determined by the Li content in the Li layers without varying significantly with the nature of the TM species. When Li^+ is extracted on charge, face-sharing octahedral sites initially occupied by Li in 1-TM channels are progressively emptied. Typical migration barriers computed for a 1-TM channel with a single Li vacancy and a di-vacancy are shown in **Figure 1-4b**. The single vacancy hop results in strong Coulombic interactions between Li^+ in the activated site and Li^+ in the face-sharing octahedral site. On the other hand, the di-vacancy hop has no such repulsion and the Li^+ diffusion barrier is lower than for hops into isolated vacancies. [1,45-47] Upon charge, the activation energy for *o-t-o* diffusion is modified by two oppositely acting mechanisms. The increase in the oxidation state of transition metals in gate sites increases the electrostatic interaction with the migrating Li^+ ion, but an increase in slab spacing for the initial part of the charge counteracts this by allowing the distance between Li^+ in the T_d site and the gate metals to remain larger. Typically, for $0.5 <\approx x<1$ in Li_xMO_2, this leads to an increase in Li diffusivity with charge. For $x < \approx 0.5$ the layer spacing decreases with charge, causing an increase in the activation barrier. At very low Li content, the slab spacing contracts due to increased hybridization and Van der Waals interactions between the oxygens across the slab, leading to an abrupt increase in the Li^+ migration barriers. [1] This geometric change is observed for all layered oxides, although the extent to which it influences Li diffusivity depends somewhat on the nature of the transition metal species and type of bonding to oxygen, which in turn determines how much the oxygen can hybridize across the empty slab. To a good approximation, Li^+ diffusion is dominated by a di-vacancy mechanism at all practical Li concentrations in layered Li_xMO_2 compounds. This results in a Li^+ diffusion coefficient that depends on the overall concentration of Li in the material; this dependence is particularly pronounced at high Li concentrations, where the vacancy concentration is low. [1] In fact, at $x\approx 1$, the di-vacancy mechanism is activated by a finite number of intrinsic vacancy defects always present in these materials. [45]

The ability to diffuse Li in other ordered rocksalts can be analyzed in the similar way. For example, the γ-$LiFeO_2$ structure shows no reversible Li deintercalation because it only contains 2-TM T_d environments making Li migration extremely high in energy. In contrast, spinel-type $LiMn_2O_4$ shows good Li diffusivity as all the Li^+ ion sites are connected with 0-TM environments. [34]

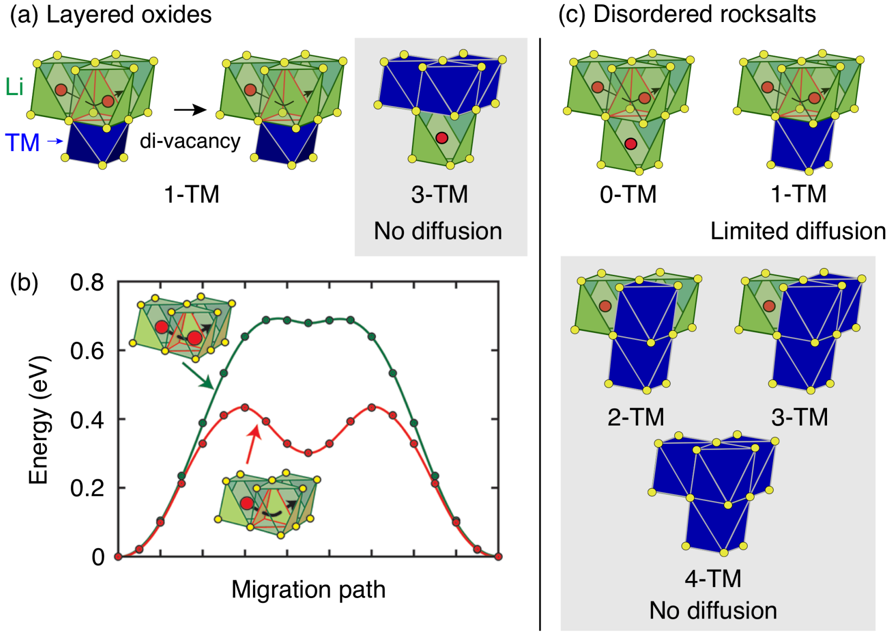

Figure 1-4. Li^+ diffusion between neighboring O_h sites in rocksalt-type Li_xTMO_2 takes place via an intermediate T_d site (*o-t-o* diffusion). (a) Layered Li_xTMO_2 compounds exhibit 1-TM and 3-TM T_d sites, corresponding to Li_3TM and $LiTM_3$ clusters, respectively. 1-TM channels are responsible for Li^+ diffusion. (b) Li migration barriers for hops between neighboring O_h sites in layered Li_xTMO_2 are very sensitive to the occupancy of sites adjacent to the intermediate T_d site of the hop. The barrier for hops into isolated vacancies is significantly larger than for di-vacancy hops. Adapted from Van der Ven et al. [1] (c) Cation disorder results in the formation of all types of tetrahedral clusters (0-TM, 1-TM, 2-TM, 3-TM and 4-TM channels). In this case, 0-TM channels (and, to some extent, 1-TM channels) are responsible for Li^+ conduction.

In a DRX structure, the 1-TM cannot be activated because of the significant reduction of the tetrahedral size. Therefore, if only the 1-TM diffusion mechanism is considered, Li^+ mobility in DRX structure is expected to be negligible. However, this analysis does not account for other types of clusters forming on disordering, as shown in **Figure 1-4c**. In 0-TM channels, for instance, the absence of TMs in the face-sharing O_h leads to a reduction of the electrostatic repulsion. As a result, while disordering causes poor Li^+ diffusivity through the 1-TM site, it also forms active 0-TN channels. 0-TM and 1-TM migration barriers computed from first principles are shown in **Figure 1-5**, which indicates that while the 0-TM barrier does not exceed 300 meV even for a small average tetrahedron height (*e.g.*, 2.35 Å). [35] A 1-TM jump, on the other hand, shows a 500 meV migration barrier, which is much larger than the typical calculated 300 meV barriers in layered oxides. [49] Furthermore, Li extraction from nearest-neighbor octahedral sites during charge leads to a progressive decrease in the 0-TM T_d site energy, eventually stabilizing T_d Li once all face-sharing octahedral Li sites are empty. [35] The relatively low barrier for Li migration between two 0-TM T_d sites, ca. 415 meV, indicates that Li can escape the T_d sites created at the end of charge and T_d Li formation has little impact on the overall Li^+ diffusion rate.

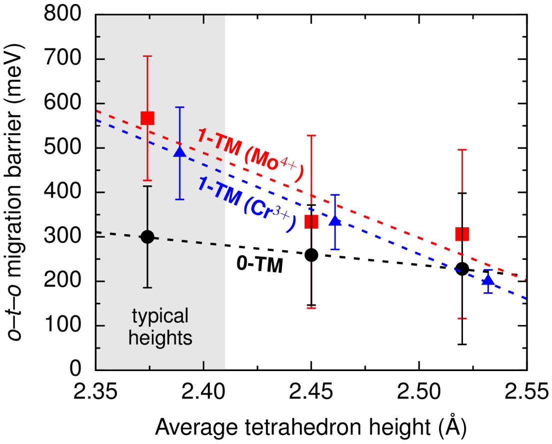

Figure 1-5. Calculated Li migration barriers along 1-TM channels (red squares: one Mo^{4+} neighbor; blue triangles: one Cr^{3+} neighbor), and along 0-TM channels (black circles) as a function of the average tetrahedron height in model disordered Li_2MoO_3 and $LiCrO_2$ structures. Error bars represent standard deviations and the shaded area highlights the typical range of tetrahedron heights in disordered materials. From Lee et al.[9]

Therefore, microscopic *o-t-o* Li^+ diffusion in layered Li_xMO_2 compounds proceeds via a Li di-vacancy mechanism and relies on 1-TM channels with a Li^+ diffusion coefficient determined by the Li slab spacing and the oxidation state of the transition metal face-sharing with Li^+ in the activated site. In contrast, Li^+ migration in DRX compounds is primarily mediated by 0-TM channels with a diffusion barrier that is almost independent on the average tetrahedron height and on the transition metal composition. [34]

Macroscopic Li^+ diffusion requires that the microscopic diffusion channels form an interconnected or percolating network. While the percolating network in layered structure is obvious (i.e., two-dimensional 1-TM network with low Li^+ migration barriers in Li slab), the percolation network in DRX structure is nontrivial. This explains why DRXs have long been considered electrochemically inactive and were only recently found to be percolating under certain conditions. [35] Although 0-TM channels have a low diffusion barrier, they are distributed in a statistical way in the disordered structure. If these channels do not form a continuous network, Li^+ diffusion is localized to percolating regions within the structure and does not lead to a measurable macroscopic current. Li^+ ions that are part of the percolating network should be extractable on charge, while those that are separated from the network may require multiple high energy hops before they can join the percolating diffusion network. Hence, they may not contribute to the reversible capacity, and we define the amount of extractable Li as the amount of Li that is in the percolating cluster. To determine whether a given rocksalt-type LiTMO structure is percolating to Li, two criteria should be considered: 1) the distribution of Li_4, Li_3M, Li_2M_2, LiM_3 and M_4 tetrahedral clusters (equivalently, the distribution of 0-, 1-, 2-, 3- and 4-TM channels) in the structure, which in turn results from the degree of cation disorder, the type of (short-range) order present, if any, and the Li to M ratio; 2) the connectivity of open diffusion channels.

Using Monte Carlo simulations, Urban et al. [34] investigated the impact of cation disorder and Li content x on Li percolation via 0-TM channels in $Li_xTM_{2-x}O_2$ ($0 \leq x \leq 2$) structures. Since the number of Li_4 clusters increases with x, 0-TM channels become percolating at a critical Li concentration x_C. The graphs in **Figure 1-6** depict the level of Li excess corresponding to the threshold for 1) Li percolation, and 2) for one Li per formula unit (1 Li/f.u.) to be accessible via 0-TM channels, as a function of cation mixing in layered (α-$NaFeO_2$), spinel-like (LT-$LiCoO_2$) and γ-$LiFeO_2$ structures. **Figures 1-6a** and **1-6c** clearly show that the spinel-like structure has the best 0-TM percolation properties, with low critical Li concentrations for percolation ($x_C = 0.77$) and for access to 1 Li/f.u. ($x_C = 1.016$); this can be explained by the segregation of Li in 0-TM channels in the structure. [34] A steady increase in the Li concentration thresholds is observed upon increasing cation disorder in the spinel-like structure, and the critical Li excess levels reach values of $x_C = 1.092$ for 0-TM percolation and $x_C = 1.257$ for access to 1 Li/f.u. in the fully random limit. For the layered structure, the critical lithium concentration for 0-TM percolation is maximal in the fully ordered structure, with a value $x_{C,max} = 1.14$, and reaches a minimum at ca. 50 % cation mixing, $x_{C,min} = 1.05$, due to the formation of 0-TM channels, before increasing again slightly upon further disordering. The lithium concentration threshold required for access to 1 Li/f.u., $x_C = 1.233$ in the ordered structure, reaches a minimum $x_{C,min} = 1.22$ for 24 % cation disorder. [34] The γ-$LiFeO_2$ structure only possesses 2-TM channels, leading to very poor percolation properties with Li concentration thresholds $x_C = 1.33$ for 0-TM percolation and $x_C = 1.417$ for access to 1 Li/f.u. With the formation of 0-TM channels, a steady decrease in the percolation thresholds is observed on cation disordering. As expected, the fully disordered limit is common to all three structure-types and corresponds to a normal distribution of Li_4, Li_3TM, Li_2TM_2, Li_3TM and TM_4 clusters based on the Li/TM ratio in the material.

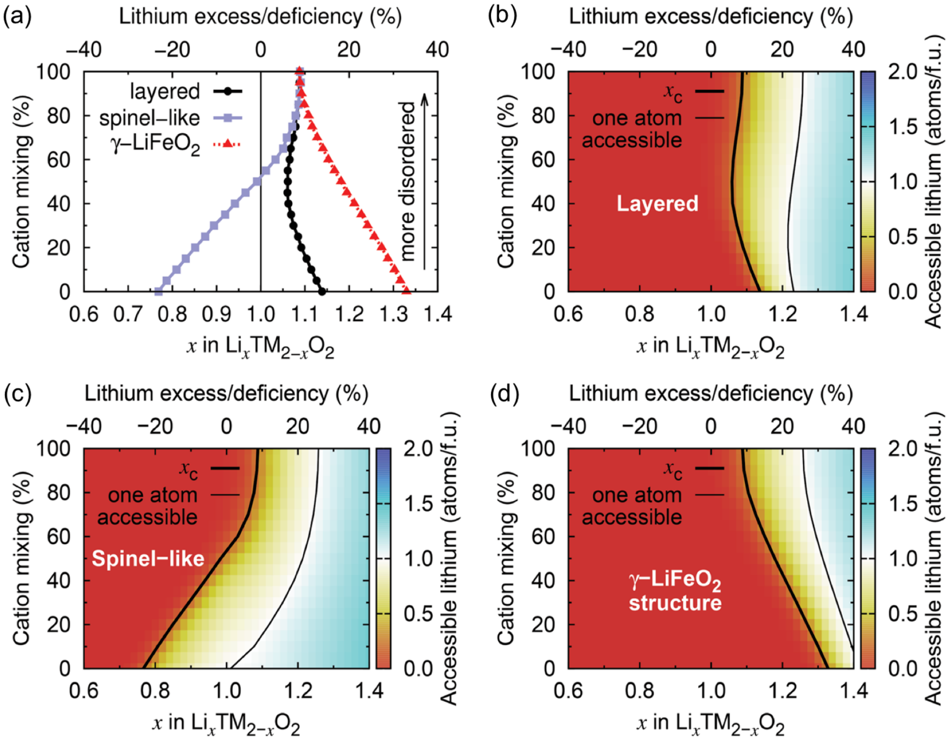

Figure 1-6. (a) Critical lithium concentrations (x_C) for 0-TM Li percolation, and (b), (c), (d) for one Li per formula unit (1 Li/f.u.) to be accessible via 0-TM channels as a function of the overall lithium content and the degree of cation mixing in $Li_xTM_{2-x}O_2$ compounds with the layered (α-$NaFeO_2$), spinel-like (LT-$LiCoO_2$) and γ-$LiFeO_2$ structure. Structure-specific x_C values are indicated by a thick black contour line. Compositions falling to the left of these contour lines are not 0-TM percolating. Thin lines indicate the compositions at which 1 Li/f.u. becomes 0-TM accessible. Adapted from Urban et al. [34]

Urban et al.'s study [34] demonstrates that, even in the fully disordered limit, rocksalt-type LTMOs can sustain long-range 0-TM Li^+ diffusion as long as Li is present in excess (Li/TM > 1). Only 10% Li excess is needed for Li percolation, and approximately 26% Li excess is required to extract 1 Li/f.u. It is important to maintain relatively low Li excess levels in these materials, as too high a Li/TM ratio results in limited transition metal redox capacity, which negatively impacts the energy density of the cathode and the overall reversibility of the charge compensation mechanisms during cycling. [34] We note that, while the results reported here describe Li^+ diffusion supported by 0-TM channels only, in reality, Li migration may occasionally involve 1-TM channels for which the tetrahedron height is sufficiently large (2-TM channels have very high migration barriers and are never involved in macroscopic Li^+ diffusion), hence the percolation thresholds in Figure 1-6 are likely overestimated.

1.3 Short-range order in DRX cathodes

Although long-range disordered, DRXs show short-range order (SRO) of cation distribution. [10,14,44,50] The probability of a given cation to occupy a specific site in a random solution of DRX structure is simply the mole fraction of that species, which is unrelated to the nature of the cations occupying neighboring sites. However, in reality, short-range spatial correlations exist between cation site occupancies, driven by energetic preferences to have some species closer together or farther apart. In metallic alloys, such SRO has been extensively studied [51,52] and related to the underlying interactions between different species. [53] Both elastic and electrostatic interactions are likely to contribute to the SRO of cations in DRX materials. Indeed, several studies have argued that SRO is prevalent in DRX compounds and may significantly impact Li^+ transport, providing another, but uncommon handle, to modify the performance of DRX cathode materials. [10,14,44,50] It should be noted that SRO is fundamentally different from long-range order and should not be confused with a poorly-formed long-range order with a small domain size. SRO is instead an equilibrium phenomenon above the order-disorder transition temperature and the truly random disordered state is expected at infinite temperature. Experimentally, SRO does not show additional peaks in XRD pattern, but shows diffuse scattering patterns in electron diffraction.

Kan et al. [14] showed that MRO in $Li_xNb_{0.3}Mn_{0.4}O_2$ is introduced by thermodynamically favorable Nb-rich O sites (i.e. ONb_6 and ONb_5Mn configurations), which perturbs the percolating Li^+ diffusion network. Jones et al. [44] use XRD/PDF, magnetic susceptibility and NMR techniques to investigate cation SRO in two $Li_{1.25}Nb_{0.25}Mn_{0.5}O_2$ samples that was synthesized via solid-state reactions at different cooling rates. The XRD patterns show low intensity superstructure reflections for both fast-cooled and slow-cooled samples, which can be accounted for by short-range or medium range ordering of cation species akin to the $\gamma-LiFeO_2$ structure. The correlation length for fast-cooled and slow-cooled sample are 30 Å and 125 Å, respectively. ^7Li nuclear magnetic resonance (NMR) measurements on both samples indicated different distributions of Li, Mn and Nb among cation sites in the structure, with a more ordered arrangement forming on slow cooling. Compared to the broad, featureless ^7Li NMR data obtained on the fast-cooled sample, the reduced range of local Li environments in the more ordered, slow-cooled sample gives rise to distinct features around 240 and 70 ppm, which also confirms that the slow-cooled sample has a longer correlation of cation order. The authors rationalize such phenomenon by a general tendency towards local electroneutrality where OLi_3Mn_3 and OLi_4NbMn clusters form preferentially, resulting in a local $\gamma-LiFeO_2$-like local arrangement of cations. The presence of 2-TM channels in $\gamma-LiFeO_2$-like domains leads to higher average Li^+ diffusion barriers. As a results, the more ordered, slow-cooled sample suffers from severer capacity and voltage fade than the more ordered, fast-cooled sample.

Ji et al. [10] found that the performance of DRX highly relies on the choice of the high-valent d^0 TMs, although it does not contribute to the redox reaction. Two DRX compositions with the same Li and Mn content and a similar concentration of d^0 TMs (Ti^{4+} and Zr^{4+}), $Li_{1.2}Mn_{0.4}Ti_{0.4}O_2$ (LMTO) and $Li_{1.2}Mn_{0.4}Zr_{0.4}O_2$ (LMZO), were compared. While these two compounds are extremely similar, they exhibit different electrochemical performance. In **Figure 1-7a**, there are 0.79 Li per formula unit (f.u.) can be extracted from LMTO at room temperature, while the value goes down to ~ 0.52 Li/f.u. for LMZO. When temperature increases to 50 °C, LMZO shows a 54% increase in reversible capacity, which clearly suggests that its room temperature capacity is limited by Li^+

transport kinetics. In contrast, LMTO shows less capacity increase when the temperature is increased, which indicates Li^+ transport is better in LMTO than LMZO at room temperature. In **Figure 1-7b**, electron diffraction patterns, together with neutron pair distribution function analysis and Monte Carlo simulations, indicate the presence of different types of SRO in the two long-range-disordered rocksalt cathodes. SRO is particularly pronounced in LMZO and plays a negative role in Li^+ transport. **Figure 1-7c** summarizes the occurrence of various tetrahedral clusters calculated by Monte Carlo simulations at 1000 °C in LMTO and LMZO relative to a random case. The occurrence of Li_4 tetrahedral clusters (i.e., 0-TM channels) is significantly lower in LMZO than in LMTO, although both materials have lower Li_4 population than for a random cation distribution. Concurrently, the population of Li_3M tetrahedral clusters (i.e., 1-TM channels) is much higher in LMZO than in LMTO, which is detrimental for Li transport in LMZO. **Figure 1-7d** visualize the Li diffusion pathways in LMTO and LMZO, respective Monte Carlo structures. The highlighted 0-TM Li networks are well connected in LMTO, whereas LMZO lacks 0-TM channels, therefore impeding Li diffusion. Overall, Ji et al.'s study proves the existence of SRO in long-range-disordered rocksalt cathodes and its significant impact on Li diffusivity, which in turn impacts electrochemical performance.

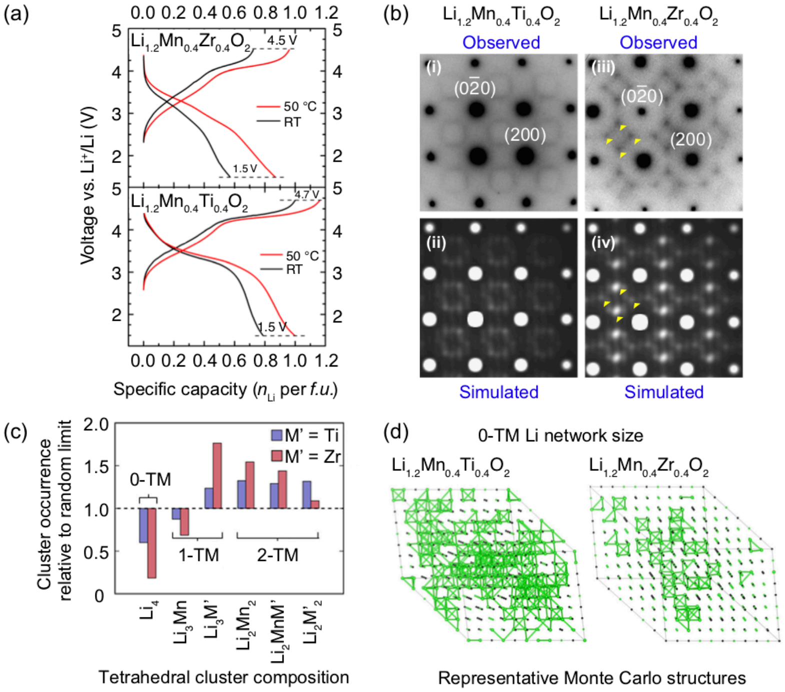

Figure 1-7. (a) Comparison of room temperature and 50°C galvanostatic cycling data for LMZO (top panel) and LMTO (bottom panel). (b) Electron diffraction patterns of (i) LMTO and (iii) LMZO along the [100] zone axis. The round spots are indexed to the $Fm\bar{3}m$ space group, while the diffuse scattering patterns around the spots are attributed to SRO. Several intensity maxima in the diffuse scattering pattern of LMZO are highlighted with yellow arrows. Simulations of electron diffraction patterns for (ii) LMTO and (iv) LMZO along the same zone axis are consistent with experimental observations. (c) Occurrence of various tetrahedron clusters (0-TM, 1-TM, 2-TM) in LMTO (blue) and LMZO (red), as compared to the random limit (dotted line). The analysis is based on structures derived from Monte Carlo simulations at 1000°C. (d) Representative Monte Carlo structures for LMTO and LMZO. Li^+ ions are labeled with green spheres and 0-TM connected Li sites are bridged with green bonds.[21] Figures adapted from Ji et al. [14]

All studies discussed above reveal that DRX structures may exhibit a certain degree of SRO, which impacts the Li transport properties. Therefore, manipulating SRO is another degree of freedom that can be introduced in DRXs to modify the electrochemical performance. The previous studies have emphasized the importance of chemistry, specifically, the charge and size of TMs, on SRO. [10] On one hand, the high-valent TMs (e.g, Mn^{3+}, Ti^{4+}, Nb^{5+}) in DRXs tend to repel each other and intimately mix with Li^{+} in order to keep local electroneutrality, thereby inhibiting Li segregation into Li_4 tetrahedra. On the other hand, the size mismatch between high-valent TMs and Li^{+} facilitates Li segregation in order to minimize strain. This effect can be well demonstrated when comparing LMTO and LMZO, where Ti^{4+} (0.605 Å) is much smaller than Li^{+} (0.76 Å) while the size of Zr^{4+} is similar to that of Li^{+}.

As illustrated in previous sections, SRO plays an crucial role in determining whether a DRX $Li_{1+x}M'_{1-x-y}M''_{y}O_2$ structure (where M' = redox active TMs and M'' = d^0 TMs) is percolating to Li, and what the proportion of Li ions is that are connected to the percolation network because it controls the fraction and connectivity of 0-TM units, as is summarized in Figure 1-8. Understanding, characterizing and manipulating SRO in DRX structures thus, become important topics to be addressed in the research of DRX cathodes.

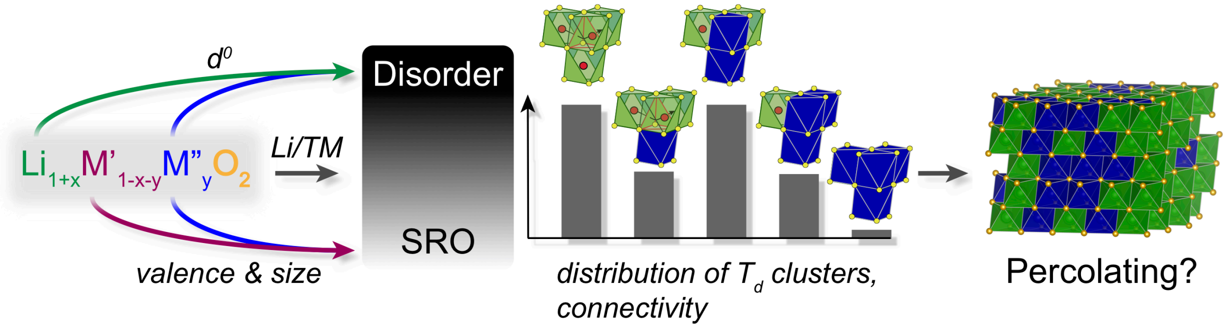

Figure 1-8. Factors contributing to the Li^{+} transport properties of a DRX lithium transition metal oxide structure.

1.4 Partially disordered spinel

When designing cathode materials, a face-centered-cubic anion framework is most beneficial for achieving dense energy storage because it is a close-packed crystalline arrangement. To obtain fast Li-ion transport and a high power density, the cations, which include Li and TM ions, should be optimally positioned within this anion framework. It is particularly important to optimize the cation arrangement to achieve better connection of Li-percolation pathways with low migration barrier (i.e., 0-TM channels) in a compact structure. It has been shown that a spinel-type cation order is more efficient at creating and percolating 0-TM channels through the structure than other common ordering types. [34] Conventional ordered spinel cathodes have been extensively studied. However, the perfectly ordered spinel (i.e., $LiMn_2O_4$) can only be practically cycled between Mn_2O_4 and $LiMn_2O_4$ compositions at ~ 4 V, that is, only over half the Li content per TM of layered analogues, and therefore provides a limited energy density of about 480 Wh kg^{-1}. [54,55] Further lithiating $LiMn_2O_4$ would cause a collective Li migration from 8a tetrahedral sites to 16c octahedral sites. [54] The first-order phase transition that occurs near 3 V, coupled with the Jahn-Teller distortion of Mn^{3+}, causes poor kinetics and poor cyclability. Ni-for-Mn substitution leads to a high-voltage spinel $LiNi_{0.5}Mn_{1.5}O_4$ with an improved energy density, while both spinels have limited capacities as they cannot reliably cycle over the low-voltage plateau between $LiTM_2O_4$ and $Li_2TM_2O_4$. [56] Substituting Mn with Li is more efficient in tuning the reaction thermodynamics. Li-rich $Li_4Mn_5O_{12}$ can be cycled between $Li_2Mn_5O_{12}$ and $Li_{6.5}Mn_5O_{12}$ with some capacity coming from oxygen redox. [57] Nevertheless, the two-phase behavior still appears when the Mn valence drops below 3.5. [58]

Ji et al [59] demonstrate two bulk disordered rocksalt oxyfluorides with partial spinel-like medium-range order, $Li_{1.68}Mn_{1.6}O_{3.7}F_{0.3}$ (LMOF03) and $Li_{1.68}Mn_{1.6}O_{3.7}F_{0.3}$ (LMOF06), which achieve a high energy density, > 1100 Wh kg^{-1}, and ultrafast rate capability. The excess Li is used to increase the concentration of 0-TM channels and active oxygen redox for a larger capacity and better Li transport kinetics, whereas the tunability in F substitution allows for lower valences of Mn and improved cyclability. [19] Importantly, the unconventionally high Li-excess and fluorination levels are achieved through mutual facilitation: the excessive amount of Li is charge-balanced by F substitution, while the concentrated fluorination is only feasible because of the presence of the Li-rich local environments. [60] Finally, different from typical ordered spinel $LiMn_2O_4$ with cation to anion ratio equals 3:4, both LMOF03 and LMOF06 are cation over-stoichiometric (cation to anion ratio equal 3.28:4). The cation over-stoichiometry induces partial TM disorder so that the voltage step and first-order transition are removed. Remarkably, we found that the ultrahigh rate performance is accomplished with half of the capacity coming from reversible oxygen redox, which suggests that the participation of anionic redox is not an intrinsic limitation to rate capability. This work shows the tremendous potential of designing high-performance and resource-efficient cathode materials in the large space between fully ordered compounds and random solid solutions.

1.5 Overview of the thesis

In this thesis, I will demonstrate two general strategies to improve the electrochemical performance of DRX system: 1) engineering the cation SRO in DRX cathodes through compositional design and synthesis control; 2) introduce spinel-type order into the disordered system. Combining electrochemical tests, advanced characterizations and computational investigations, we achieved a large improvement and better understanding of DRX cathodes.

Chapter 2 investigates the SRO in fluorinated DRX systems using both computations and experiments. The strong Li-F interaction modifies the cation SRO in DRX materials by forming Li-rich enviorments around F ions. We demonstrate that Mg-doping can reduce the amount of Li in the fluorinated DRX compounds that is strongly bound to F and thereby increases the accessible Li and capacity. We verify our hypothesis by characterizing the structure of $Li_{1.25}Mn_{0.45}Ti_{0.3}O_{1.8}F_{0.2}$ and $Li_{1.25}Mg_{0.1}Mn_{0.45}Nb_{0.2}O_{1.8}F_{0.2}$ and evaluating the electrochemical performance. Though both compounds have the same Li-excess and Mn content, the Mg-doped compound has higher accessible Li. Finally, we extend the discussion to a related group of compositions: $Li_{1.333}Mn_{0.667}O_{1.333}F_{0.667}$ (LMF), $Li_{1.233}Mg_{0.1}Mn_{0.667}O_{1.333}F_{0.667}$ (ls-LMF), $Li_{1.333}Mg_{0.1}Mn_{0.567}O_{1.333}F_{0.667}$ (ms-LMF) and $Li_{1.28}Mg_{0.11}Mn_{0.61}O_{1.333}F_{0.667}$ (ls-LMF) to demonstrate that the improved accessible Li, enabled by Mg doping, can also be traded to improve cycle life. The results show that Mg-doping strategy should be considered in fluorinated cathodes, to optimize DRX oxyfluoride cathodes.

Chapter 3 investigates the solid-state synthesis mechanism of Li-excess DRX oxyfluoride, $Li_{1.2}Mn_{0.55}Ti_{0.25}O_{1.85}F_{0.15}$ (LMTF). Experimentally, through *in-situ* transmission electron microscopy, *ex-situ* X-ray diffraction and pair distribution function analysis, we observed the sequential formation of long-range disorder and short-range order during the synthesis. We proposed an optimized strategy for the synthesis protocol, which leads to a remarkably enhanced capacity and rate capability.

Chapter 4 demonstrates a series of well selected partially-(dis)ordered spinel cathodes, $Li_{1.4+x}Mn_{1.6}O_{3.7}F_{0.3}$ ($x = 0.07$, 0.28, and 0.6), in which different degrees of cation disorder are used to suppress the two-phase reaction. We reveal that the over-stoichiometry of cations in the synthesis is the key to control the amount of Mn 16c/16d disorder in the structure and its electrochemical performance.

Chapter 2 Increasing capacity in DRX cathodes by Mg doping

The work presented in this chapter is based, often verbatim, on the following publication: Zhong, Peichen, et al. "Increasing capacity in disordered rocksalt cathodes by Mg doping." Chemistry of Materials 32.24 (2020): 10728-10736.

2.1 Introduction

The continued growth of the Li-ion battery industry depends on the discovery of high-energy-density cathode materials based on non-precious elements.[2,61] Conventionally, NMC-class cathode materials composed of the redox-active elements Ni and Co and the stabilizer Mn^{4+} are mostly used in industry.[62] Recently, facile Li transport has also been demonstrated in cation disordered rocksalt (DRX) cathode materials, where Li-ion diffusion occurs via a percolating network of Li-rich environments.[35] As these materials do not require the cation chemistry to favor any particular ordering, they can be synthesized with a wide variety of metals.[50] **Figure 2-1a** presents the typical DRX crystal structure with interpenetrating cation and anion fcc sublattices . In DRX materials, Li-ions diffuse between neighboring octahedral (Oh) sites via an intermediate tetrahedral (Td) site as illustrated in **Figure 2-1a**. A 0-TM channel is formed when no transition metal surrounds the Td site. This 0-TM channel has a low lithium migration barrier energy compared to other types of clusters and is thus beneficial for Li-ion transport.[35] When sufficient Li-excess is present in a compound 0-TM channels can be long-range connected, enabling percolation. Lee et al.[35] showed that a certain amount of Li-excess (Li1+x>1.09 in case of randomly distributed cations) is required to enable Li percolation in a $Li_{1+x}TM_{1-x}O_2$. The percolating Li content can be used as a metric to evaluate the Li capacity of DRX cathodes.

However, the higher Li content in DRX cathodes results in a decrease in available transition metal (TM) redox, and increased reliance on oxygen redox, which is detrimental to long-term capacity retention. [11,23,28,30] Hence, a key objective in DRX cathode design is to maximize the TM redox capacity while maintaining a high level of Li excess. Fluorination of Li-TM oxides is one such strategy as it can lead to increased capacity by reducing the transition metal valence in the discharged state.[12,32,33,63] In addition, fluorine substitution has been found to protect the surface of DRX particles.[19,64] While the solubility of fluorine in a layered $LiTMO_2$ phase is extremely low, fluorine substitution is thermodynamically favorable in the disordered rocksalt phase, due to the statistical occurrence of anion environments predominantly coordinated by Li.[60] Using density functional theory (DFT) and solid-state nuclear magnetic resonance (NMR) spectroscopy, Clément et al.[50] demonstrated the exis- tence of Li-F short-range order (SRO) and its coupling to unusual modes of nickel redox in DRX cathodes. More recently, Mozhzhukhina et al.[65] confirmed the existence of Li-F SRO by Raman spectroscopy. Lun et al.[66] argued that the degree of fluorination has a significant impact on cathode material design, by improving the Li percolating network and thus achieving faster ionic diffusion. In addition, Ouyang et al.[67] recently showed that fluorination can substantially affect SRO and, at sufficiently high concentrations, is beneficial to Li-ion transport.

Though fluorination brings several performance improvements to DRX materials, Li-F SRO also has some negative effects on the capacity and energy density of DRX cathodes. One problem in Li-TM oxyfluorides is the Li-F “locking effect”. This effect manifests itself as a high voltage required to extract all Li-ions from the Li-rich environment that coordinates with F (**Figure 2-1b**). Using DFT calculations, Kitchaev et al.[13] reported that the voltage is greater than 5.0 V to extract the Li from a fluorine coordination shell and make the fluorine uncoordinated. The voltage is well above the typical electrolyte stability limit, which means a fraction of Li is “locked” to fluorine. To illustrate the significance of the Li locking effect in oxyfluorides, we show in Figure 1c the frequency with which Li6X and Li5MX (X=anion) environments are found in $Li_{1.25}Mn_{0.45}Ti_{0.3}O_{1.8}F_{0.2}$ and $Li_{1.25}Mn_{0.25}Ti_{0.5}O_2$. These results were obtained by averaging over structures obtained from Monte Carlo simulations at 1000 °C, using a cluster expansion Hamiltonian parameterized by DFT. In **Figure 2-1c**, the orange and green bars represent the oxyfluoride and pure oxide compounds, respectively. The frequency with which these two types of anion environments occur in oxyfluorides are much higher than in pure oxides; in particular, the presence of Li6X is almost never found in the oxide but occurs frequently in the oxyfluoride. At least one Li ion is impossible to be extracted from the Li6F environment, which limits “extractable lithium” capacity.[13] Thus, to achieve higher capacity and energy density, one of the key factors is to reduce the number of “locked” lithium ions around fluorine.

Here, I will demostrate a solution to this issue, which consists in adding another inactive cation that displaces some Li from the F environments to an environment from which it can be extracted. This requires a cation with similar or stronger F-bonding preference, and similar ionic radius as Li. As the doped cation is not extractable, it also prevents the formation of under-coordinated fluorine after the removal of Li ions. In this study, we first screen various main group elements in terms of (1) bonding energies in metal-fluorides and (2) ionic radius difference with Li+, selecting species that are comparable to lithium. The results indicate that magnesium (Mg) satisfies both criteria and is a promising element to substitute into fluorinated DRX materials. A detailed theoretical investigation of Li–F SRO using DFT calculations and cluster expansion (CE) Monte Carlo (MC) simulations confirms that Mg doping results in a greater fraction of extractable Li ions by reducing the frequency of the Li6F configuration. We verify our hypothesis by characterizing the structure of $Li_{1.25}Mn_{0.45}Ti_{0.3}O_{1.8}F_{0.2}$ and $Li_{1.25}Mg_{0.1}Mn_{0.45}Nb_{0.2}O_{1.8}F_{0.2}$ and evaluating the electrochemical performance. Though both compounds have the same Li-excess and Mn content, the Mg-doped compound has higher capacity. Finally, we extend the discussion to a related group of compositions: $Li_{1.333}Mn_{0.667}O_{1.333}F_{0.667}$ (LMF), $Li_{1.233}Mg_{0.1}Mn_{0.667}O_{1.333}F_{0.667}$ (ls-LMF), $Li_{1.333}Mg_{0.1}Mn_{0.567}O_{1.333}F_{0.667}$ (ms-LMF), and $Li_{1.28}Mg_{0.11}Mn_{0.61}O_{1.333}F_{0.667}$ (LMMF), to demonstrate that the improved Li use, enabled by Mg doping, can also be traded to improve cycle life.

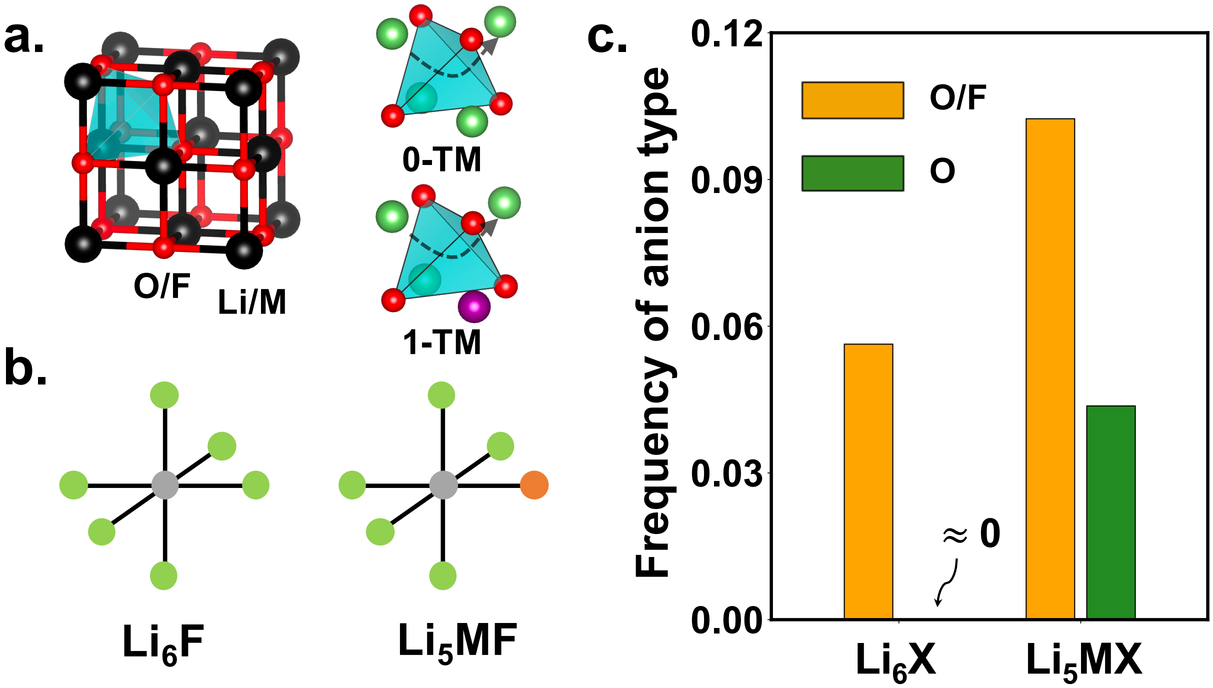

Figure 2-1. (a) Crystal structure of DRX cathodes. The black spheres represent metal cations (including lithium, TM, and doping metal), and the red spheres represent anions (including oxygen and fluorine). Both cations and anions are in octahedral coordination (Oh). The blue tetrahedral site (Td) is an intermediate site on the pathway that Li takes when it migrates between two octahedral sites. The 0-TM and 1-TM tetrahedrons are illustrated. (b) Schematic illustration of two frequently occurring cation configurations (Li6X and Li5MX (X=anion) around a fluorine atom). (c) Frequency of configuration Li6X and Li5MX in simulated pure oxide and oxyfluoride compounds. The orange and green bars represent the fluorinated and unfluorinated composition of $Li_{1.25}Mn_{0.45}Ti_{0.3}O_{1.8}F_{0.2}$ and $Li_{1.25}Mn_{0.25}Ti_{0.5}O_2$, respectively.

2.2 Methodology

2.2.1 Experimental methodology

2.2.1.1 Synthesis

$Li_{1.25}Mn_{0.45}Ti_{0.3}O_{1.8}F_{0.2}$ (LMTF) and $Li_{1.25}Mg_{0.1}Mn_{0.45}Nb_{0.2}O_{1.8}F_{0.2}$ (LMMNF) were synthesized by solid-state reaction. Li_2CO_3 (Alfa Aesar, ACS, 99%), Mn_2O_3 (Alfa Aesar, 98%), TiO_2 (Anatase, Alfa Aesar, 99.9%), Nb_2O_5 (Alfa Aesar, 99.9%), MgF_2 (Alfa Aesar, 99.9%) and LiF (Alfa Aesar, 99.99%) were used as precursors. The precursors were stoichiometrically dispersed into ethanol in a 50-mL stainless-steel jar with five 10-mm (diameter) stainless-steel balls (except that 10% excess Li_2CO_3 was added to compensate for possible loss during synthesis). After ball milling at 250 rpm for 12 h, the precursors were dried overnight in an oven. The mixture of the precursors was pelletized and then sintered at 600 °C for 2 h in Ar to decompose the carbonates, followed by calcining at 1000 °C for 4 h in Ar. The pellet was transferred to a glovebox after furnace cooling to room temperature. After the calcination, the pellets were manually ground into fine powder.

$Li_{1.333}Mn_{0.667}O_{1.333}F_{0.667}$ (LMF), $Li_{1.28}Mg_{0.11}Mn_{0.61}O_{1.333}F_{0.667}$ (LMMF), $Li_{1.333}Mg_{0.1}Mn_{0.567}O_{1.333}F_{0.667}$ (ms-LMF) and $Li_{1.233}Mg_{0.1}Mn_{0.567}O_{1.333}F_{0.667}$ (ls-LMF) were synthesized by mechanochemical ball milling. Li_2O (Alfa Aesar, ACS, 99%), MgF_2 (Alfa Aesar, 99.9%), MnO (Sigma- Aldrich, 99.99%), Mn_2O_3 (Alfa Aesar, 99%), MnO_2 (Alfa Aesar, 99.9%), and LiF (Alfa Aesar, 99.99%) were stoichiometrically added into a 50-mL stainless-steel jar with five 10-mm (diameter) and ten 5-mm (diameter) stainless-steel balls. The total amount of precursors was 1 g. The jars were sealed with a safety closure in an Ar-filled glovebox after ball milling at 500 rpm for 40, 40, 35 and 35 h, for LMF, LMMF, ms-LMF and ls-LMF, respectively.

2.2.1.2 Electrochemistry

To prepare a cathode film for each material, 210 mg of active material and 60 mg of Super C65 carbon black were mixed and shaker-milled for 1 h in Ar atmosphere using a SPEX 800M Mixer/Mill. Then, 90 mg of the mixture was manually mixed with 10 mg of PTFE manually and rolled into a thin film in a glovebox. Coin cells (CR2032) were assembled by using commercial 1M LiPF6 in ethylene carbonate (EC) and dimethyl carbonate (DMC) solution (volume ratio 1:1) as the electrolyte, glass microfiber filters (Whatman) as separators and Li metal foil (FMC) as the anode. The coin cells were tested on an Arbin battery cycler at room temperature. The loading density of the cathode films was approximately 3 mg/cm^2 based on the active materials.

2.2.1.3 Characterization

X-ray diffraction (XRD) patterns of the as-synthesized compounds were obtained using a Rigaku MiniFlex diffractometer (Cu source) in the 2θ range of 5° − 85°. Rietveld refinement was performed using PANalytical X'pert HighScore Plus software. SEM images were obtained using a Zeiss Gemini Ultra-55 analytical field-emission scanning electron microscope at the Molecular Foundry at Lawrence Berkeley National Lab (LBNL). High-angle annular dark-field scanning transmission electron microscopy (HAADF-STEM) and energy-dispersive X-ray spectroscopy (EDX) mapping were performed on a FEI TitanX 60-300 microscope equipped with a Bruker windowless EDX detector at an acceleration voltage of 200 kV at the Molecular Foundry at LBNL.

2.2.1.4 Solid-state nuclear magnetic resonance (NMR) spectroscopy

^{19}F ssNMR data were collected on the LMTF, LMMNF, LMF and LMMF pristine powders using a Bruker Avance 300 MHz (7.05 T) super wide-bore NMR spectrometer with Larmor frequencies of 282.40 MHz at room temperature. The data were obtained at 30 kHz magic-angle spinning (MAS) using a 2.5 mm double-resonance HX probe. ^{19}F NMR data were referenced against pure lithium fluoride powder (LiF, $\delta(^{19}F) = 204$ ppm) and these samples were also used for pulse calibration. Lineshape analysis was carried out within the Bruker Topspin software using the SOLA lineshape simulation package.

Due to the wide frequency range covered by ^{19}F resonances in LMTF, LMMNF, LMF and LMMF, it is impossible to excite the entire ^{19}F NMR spectrum with a single radio frequency (RF) pulse. Instead, nine spin echo sub-spectra were recorded, with the irradiation frequency varied in steps of 425 ppm or 120 kHz from −1700 ppm to 1700 ppm, and these sub-spectra were added together to obtain the final sum spectrum for each sample. For this, each individual sub-spectrum was processed using a zero-order phase correction so that the on-resonance signals are in adsorption mode. The nine sub-spectra were then added together to give an overall sum spectrum with no further phase correction required. This "frequency stepping" [68,69], "spin-echo mapping" [70], or "variable offset cumulative spectrum" (VOCS) [71] methodology provides a large excitation bandwidth with uniform excitation of the broad ^{19}F signals. Individual ^{19}F rotor-synchronized spin echo spectra ($90^\circ - \tau R - 180^\circ - \tau R$) were obtained using 90° and 180° RF pulses of 0.7 μs and 1.4 μs at 200 W, respectively, and 10240 scans collected using a 30 ms recycle delay.

2.2.2 Computational methodology

2.2.2.1 Computational methods for Li-Mg-Mn-Ti-O-F compounds

To evaluate the equilibrium ordering of multicomponent DRX compounds, we constructed a cluster expansion Hamiltonian in the configurational space LiF-MgO-$LiMnO_2$, LiF-MgO-$LiMnO_2$-Li_3NbO_4 and LiF-$LiMnO_2$-Li_2TiO_3 on a rocksalt lattice. The cluster expansion technique is used to study the configurational thermodynamics of materials featuring a mixture of species on cation sites, and has been applied to study Li-vacancy configurations in layered materials. [72] As in the LiF-$LiMnO_2$-Li_2TiO_3 system, the anion fcc lattice com- prises O^{2-} and F^-, while the lattice of octahedral cation is composed of Li^+, Mn^{3+}, and Ti^{4+}/Nb^{5+}. A coupled sublattice approach was therefore used. [73] We fitted a cluster expansion model consisting of pair interactions up to 7.1 Å, triplet interactions up to 4.0 Å and quadruplet interactions up to 4.0 Å based on a primitive cell of the rocksalt structure with lattice parameter a = 3 Å. Effective cluster interactions (ECIs) were obtained from $\ell 1$-norm regularized linear regressions with the best regularization parameter selected to minimize the cross-validation (CV) score. [74,75] The root-mean squared (RMS) CV errors were converged to below 8 meV/atom.

All the DFT calculations were performed with the Vienna ab initio simulation package (VASP) [76] using the projector-augmented wave method,[77] a plane-wave basis set with an energy cutoff equal to 520 eV, and a reciprocal space discretization of 25 k-points per Å. All calculations were converged to 10−6 eV in total energy for electronic loops and 0.02 eV/Å in interatomic forces for ionic loops. We used the Perdew–Burke–Ernzerhof (PBE) generalized gradient approximation exchange-correlation functional [78] with rotationally-averaged Hub- bard U correction (GGA+U) to compensate for the self-interaction error on all transition metal atoms except titanium.[79] The U parameters were obtained from the literature, where they were calibrated to transition metal oxide formation energies (3.9 eV for Mn and 1.5 eV for Nb). The GGA+U computational framework is believed to be reliable in determining the formation enthapies of similar compounds. [80]

Monte Carlo simulations on these cluster expansion Hamiltonians were performed in a canonical ensemble using Metropolis-Hastings sampling on a 8 × 8 × 10 supercell (1280 atoms) of the primitive unit cell of the rocksalt structure. All the statistical quantities were obtained from

1000 sampled structures of the equilibrium ensemble. Percolation analysis was completed on these sampled structures using the dribble package. [35]

2.3 Results

2.3.1 Screening results

The M-F bonding energy is calculated from the formation enthalpy per F atom, ΔHf /y, of the metal fluoride MFy. The values of $\Delta H_f/y$, where ΔHf is obtained from the Materials Project, [81] are shown in **Figure 2-2**. As a baseline, the bonding energy of Li per F is −3.18 eV. No other element has stronger bonding with F than Li. The fluorides of the [Sc, Y] and [B, Al, Ga] groups have less negative enthalpy than the [Be, Mg, Ca] group. Thus, only group-II elements have comparable interaction with F to Li.

Another criterion is the ability to accommodate the dopant in the disordered rocksalt structure. Empirically, the Hume-Rothery rule predicts that species with similar electronegativity form a solid solution when their atomic radii differ by no more than 15%. [82] Even though this criterion is determined for metallic alloys, we adopt it here to determine whether a candidate element might be substituted in the cation-disordered phase. In **Figure 2-2**, the red squares represent the percentage of ionic radii difference with Li^+, and the red dashed line represents 15% difference. [83] Only Mg^{2+} and Sc^{3+} satisfy this criterion, although Y^{3+} and Ga^{3+} are only slightly above the 15% line. Combining the radius information with the energetic preferences points at Mg^{2+} being a suitable cation.

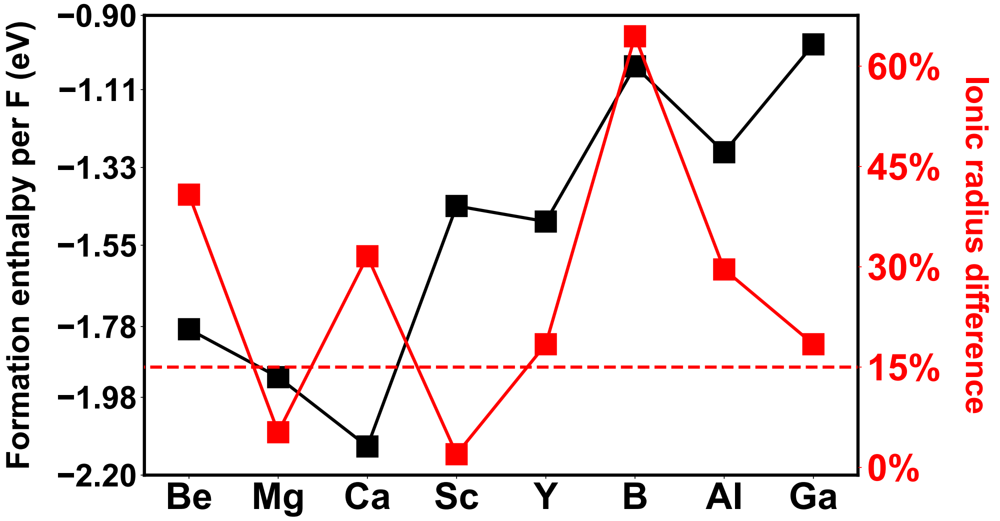

Figure 2-2. Screening of main group elements on bonding preference with F and ionic size difference with Li. The black and red lines represent formation enthalpy per F and percentage of ionic radius difference with Li ion, respectively. The dashed red line corresponds to a 15% radius difference.

2.3.2 Computational predictions

To characterize in more detail how Mg addition affects cation ordering and Li-F short-range order in DRX materials, we computationally investigated two compounds, $Li_{1.25}Mn_{0.45}Ti_{0.3}O_{1.8}F_{0.2}$ (LMTF) and $Li_{1.25}Mg_{0.1}Mn_{0.45}Nb_{0.2}O_{1.8}F_{0.2}$ (LMMNF) with identical Li-excess, redox active TM and fluorination amount. Canonical cluster expansion Monte Carlo (CEMC) simulation was applied at 1000 °C to simulate the as-synthesized samples. [13] The frequency of different cation configurations around F and their percolation properties were averaged over 1000 structures sampled from the equilibrium ensemble.

Figure 2-3a shows the frequency with which several types of cation environments around F occur. The Li6F and Li5MF environments dominate both LMTF and LMMNF. In LMTF, without Mg-doping, over 50% of F ions are surrounded by six Li-ions. However, the peak of the distribution shifts to Li5MF in LMMNF, and the Li6F frequency is lowered to 35%. In particular, the LiMg5F environment, shown as the brown dashed bar, makes up around 37% of the Li5MF environments. This finding indicates that modifying the DRX composition with Mg can effectively reduce the number of Li6F environments and render Li-ions more accessible.

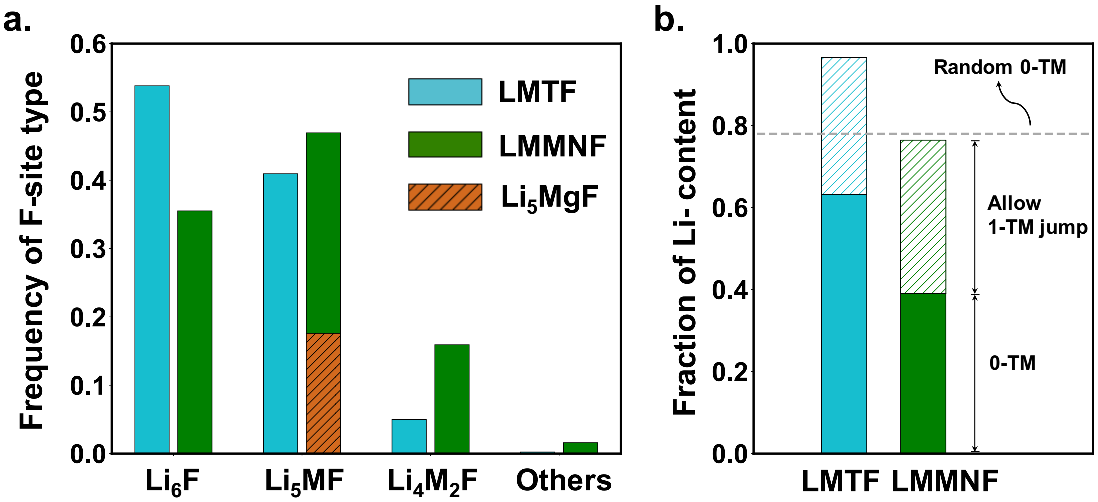

Figure 2-3. (a) Frequency of different types of fluorine environments averaged over 1000 sampled structures from the equilibrium ensemble. LMTF/LMMNF is represented by the blue/green bar, respectively. The brown dashed bar represents the LiMg5F environment in LMMNF. (b) Percolation analysis of LMTF and LMMNF. The solid bar represents percolating Li-content in the 0-TM percolating network, and the dashed bar (1-TM) represents additional percolating Li-content when one jump through a 1-TM barrier into the 0-TM network is included.

LMTF and LMMNF also differ in their d^0 charge compensating element. Although Ti^{4+} and Nb^{5+} are both electrochemical inactive, they can affect atomic ordering and thus the percolating Li-content of DRX cathodes. [17,84] To rule out that the capacity improvement of LMMNF is caused by the change in charge compensator, the fraction of Li content in the percolating network of each compound is plotted in **Figure 2-3b**. The gray dashed line indicates that a percolating Li content of approximately 78% is achieved when the cations are randomly arranged. The solid bar represents the fraction of Li content in the 0-TM network, and the dashed bar represents the Li that can reach the 0-TM network with a single 1-TM hop. LMTF has a higher fraction of Li content in both the 0-TM and 1-TM networks, as compared to LMMNF. These results are consistent with percolation predictions in previous work [10] on Li-TM oxides. Thus, the larger fraction of accessible Li ions in LMMNF more likely originates from the fact that Mg displaces Li from the F-bonded position than from the percolating Li content. Compared with LMTF, Mg-doped LMMNF has a much lower frequency of Li6F environments, leading us to predict a higher achievable electrochemical capacity for LMMNF than for LMTF.

2.3.3 Experimental verification

LMTF and LMMNF were synthesized as described in the Methods section. The X-ray diffraction (XRD) pattern (**Figure 2-4a**) indicates that both materials form a disordered rocksalt structure (space group: Fm-3m) without any detectable impurity phases. The Rietveld refinement

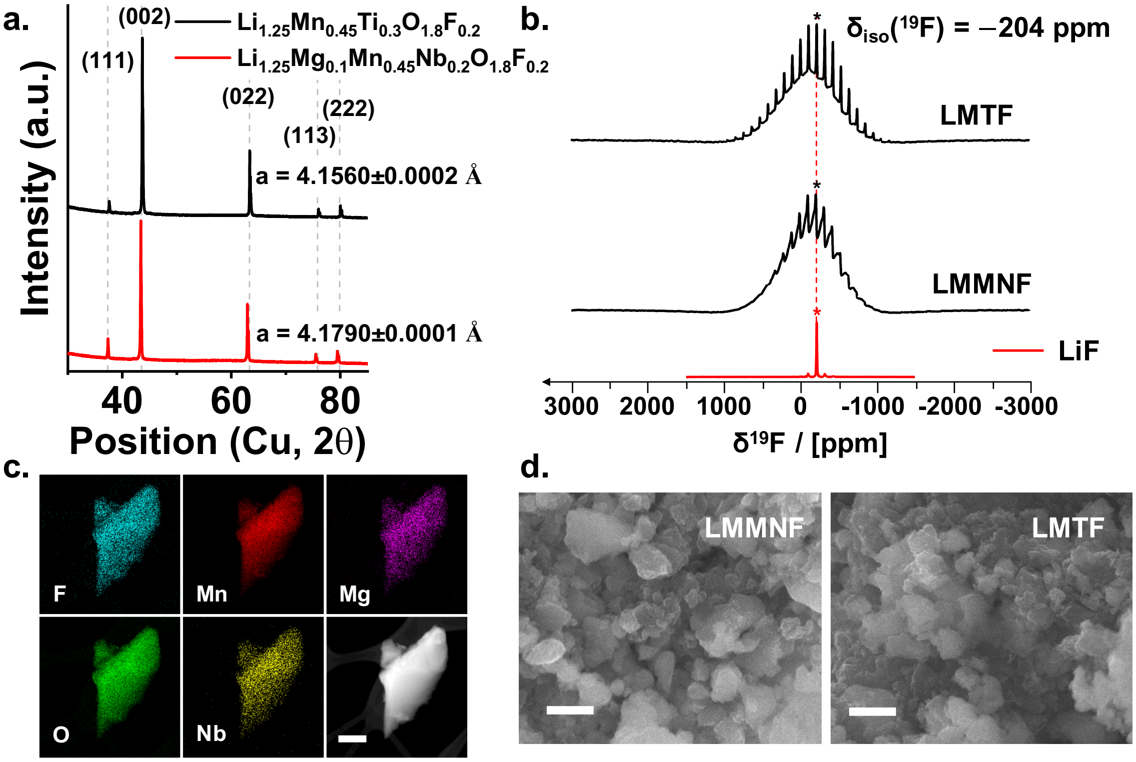

Figure 2-4. Structural and morphological characterization of LMTF and LMMNF. (a) XRD patterns of LMTF and LMMNF indexed according to the rocksalt structure. (b)^{19}F spin echo magic angle spinning (MAS) NMR spectra of LMTF and LMMNF recorded at B_0 = 7.05 T. For comparison, ^{19}F spin echo spectra collected under similar experimental conditions on a LiF powder sample are shown in red. The isotropic shift of the sharp resonance corresponding to ^{19}F nuclei in LiF-like environments in the ^{19}F NMR spectra is denoted with an asterisk. Spinning sidebands due to fast rotation of the samples during data acquisition are observed on either side of the isotropic signals. (c) TEM-EDS mapping of the element distribution in a representative particle of as-synthesized LMMNF (scale bar: 300 nm). (d) SEM images of as-synthesized LMTF and LMMNF (scale bar: 400 nm).

reveals a simple disordered rocksalt structure (**Figure 2-5a,b**) and gives a lattice parameter of 4.1560 Å(LMTF) and 4.1790 Å(LMMNF). As the only change from LMTF to LMMNF is the substitution of Ti^{4+} (74.5 pm) by Mg^{2+} (86 pm) and Nb^{5+} (78 pm) the increase in lattice parameter is expected.

High-angle annular dark-field scanning transmission electron microscopy (HAADF-STEM) images and the corresponding energy-dispersive X-ray (EDX) elemental mapping of LMTF and LMMNF are presented in **Figure 2-4c** and **Figure 2-6**, respectively. The elemental mapping of LMTF and LMMNF reveals that all elements are homogeneously distributed in representative particles, without surface segregation or phase separation, indicating that Mg and F are successful incorporated into the bulk. Scanning electron microscopy (SEM) images shown in **Figure 2-4d** indicate an average primary particle size of ~ 400 - 500 nm for both LMTF and LMMNF samples. The agglomeration of primary particles into secondary particles around ~ 1 μm in size is observed.

^{19}F solid-state nuclear magnetic resonance (ss-NMR) measurements were conducted to verify the bulk integration of F. The ^{19}F NMR spectra obtained on LMTF and LMMNF (**Figure 2-4b**) exhibit a broad signal, spanning more than 2000 ppm, overlapping with a sharp signal comprised of a centerband at the isotropic shift (−204 ppm, indicated with an asterisk) and a series of sidebands on either side of the centerband resulting from fast spinning of the sample during data acquisition. The broad signal is comprised of several broad and overlapping signals characteristic of ^{19}F nuclei incorporated in the bulk DRX structural framework, as has been reported for related systems. [9,12,41,50,85] This broad signal corresponds to ^{19}F nuclei in the bulk of the material, which is the result of (i) a distribution of chemical shifts due to the large number of F local environments in the cation-disordered structure, and (ii) NMR line broadening caused by strong paramagnetic interactions between F nuclei and nearby unpaired d electrons on Mn ions within the DRX structure. The sharp signal at −204 ppm resonates at the same frequency as ^{19}F nuclei in pure LiF (spectrum shown in red in **Figure 2-4b**) and is therefore attributed to ^{19}F nuclei in LiF-like diamagnetic environments. LiF-like ^{19}F signals in the spectra collected on DRX samples exhibit many more sidebands than the pure LiF signal collected under similar conditions. The greater number of sidebands signifies an increase in the chemical shift anisotropy of ^{19}F nuclei in LiF-like environments in the DRX samples, resulting from their close proximity to Mn centers and long-range anisotropic paramagnetic interactions. These observations suggest that LiF-like ^{19}F environments either arise from Li-rich F local environments in the rocksalt cathodes or from a thin layer of LiF rocksalt impurity phase at the surface of the DRX particles. It is important to note that, when F is directly bonded to a Mn ion, the paramagnetic interaction becomes so strong that the resulting NMR signal is too broad and too short lived to be detected. [50] Hence, the amount of impurity LiF cannot be determined quantitative from ^{19}F NMR, as part of the signal from the DRX cathode is missing. Assuming that a diamagnetic LiF impurity phase is present, the intensity ratio of the broad paramagnetic signal to the sharp diamagnetic signal (para:dia) still indicates that the great majority of F ions are incorporated into the bulk of both LMTF and LMMNF compounds.

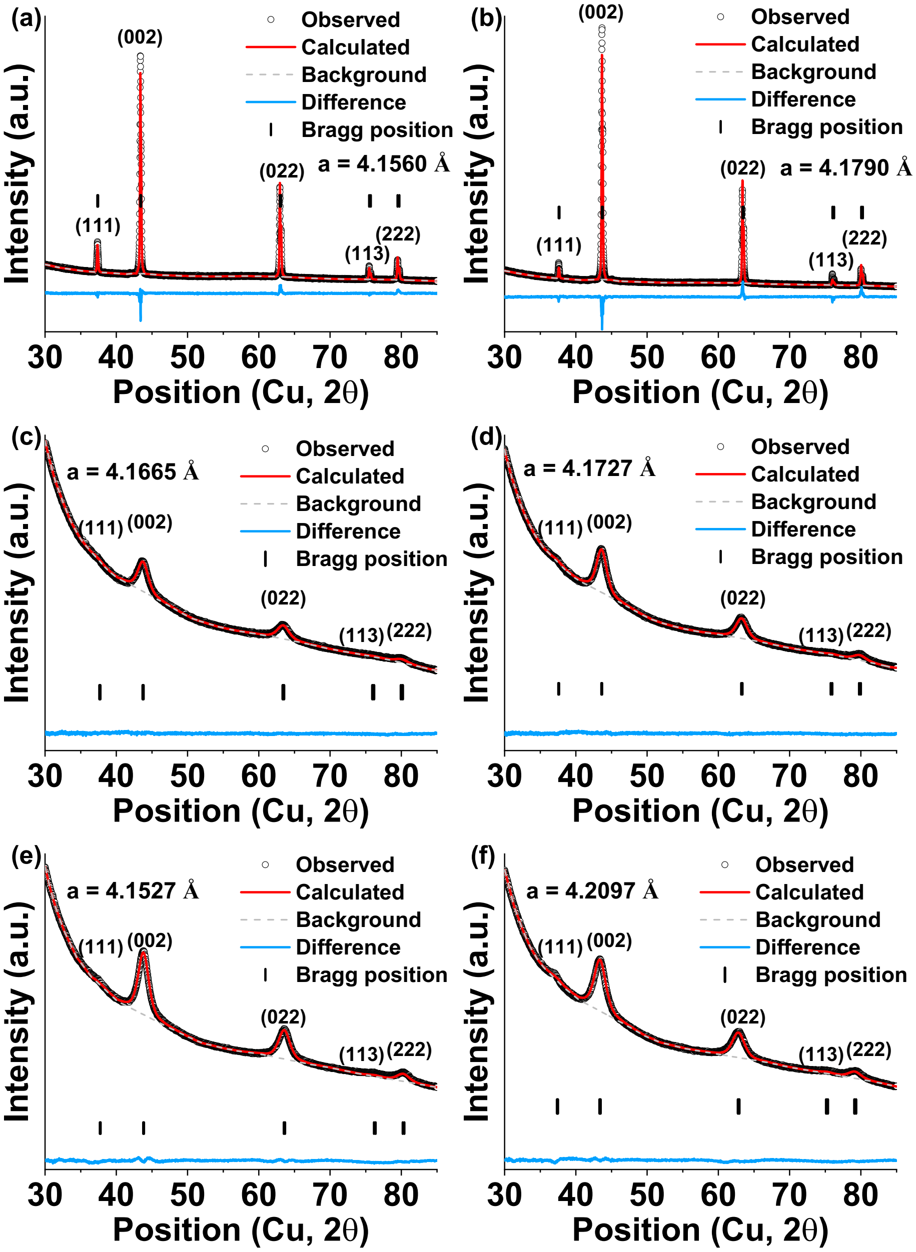

Figure 2-5. XRD refinement of (a) LMTF, **(b)** LMMNF, **(c)** LMF, **(d)** LMMF, **(e)** ls-LMF, and **(f)** ms-LMF.

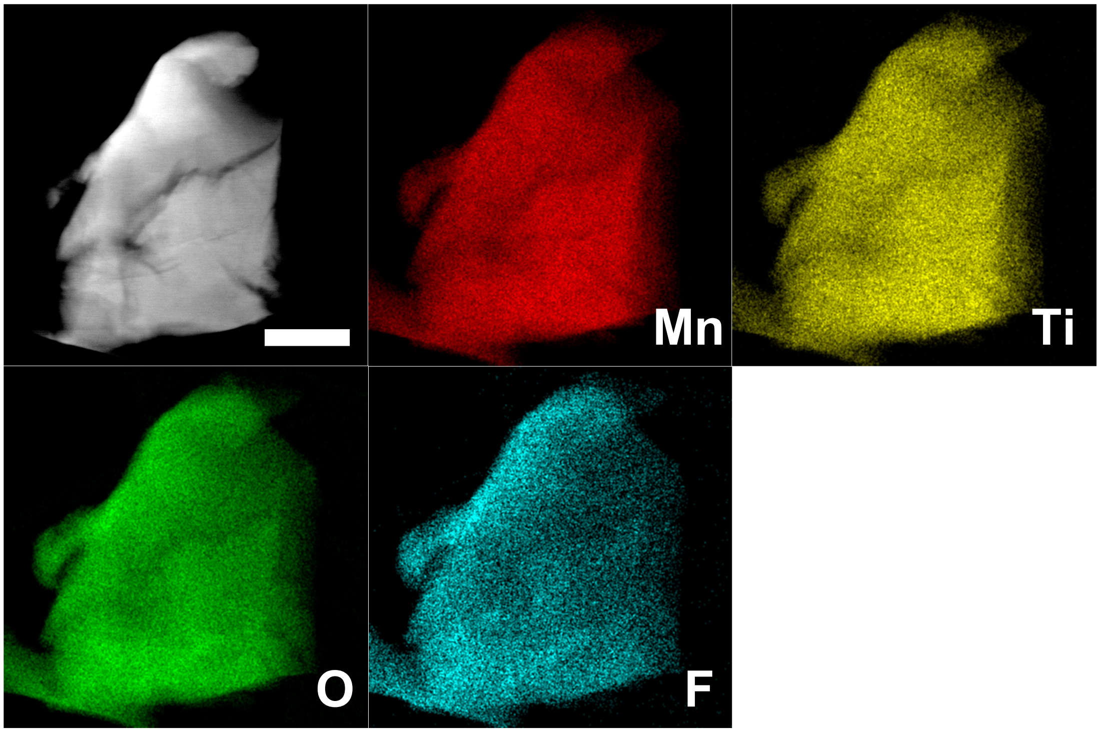

Figure 2-6. TEM-EDS mapping of the element distribution in a representative particle of as-synthesized LMTF (scale bar, 300 nm)

In **Figure 2-7**, the electrochemical properties of LMTF and LMMNF are compared using galvanostatic cycling between 1.5 and 4.8 V at 20 mA g^{-1} and room temperature. The blue dashed lines represent the theoretical capacity based on $Mn^{3+/4+}$ redox in each sample. LMTF delivered a first charge capacity of 337 mAh g^{-1} and a discharge capacity of 279 mAh g^{-1} (899 Wh kg^{-1}). LMMNF delivers a similar initial charge capacity of 332 mAh g^{-1} but a larger discharge capacity of 290 mAh g^{-1} (905 Wh kg^{-1}). Charging extracted 1.01Li and 1.08Li per formula unit (f.u.) from LMTF and LMMNF, respectively. The locked Li content decreases by about 29% from 0.24 per f.u. in LMTF to 0.17 per f.u. in LMMNF with the substitution of Ti by Mg and Nb, as shown in **Figure 2-7c**. To verify that this improvement is not caused by the change in chemistry of the charge-compensating element, $Li_{1.25}Mn_{0.6}Nb_{0.15}O_{1.8}F_{0.2}$ (LMNF) was synthesized and compared with LMMNF. LMNF exhibits a lower initial charge capacity of 293 mAh g^{-1} as compared to LMMNF (**Figure 2-8**), and the amount of non-extractable Li at top of the charge is increased to 0.28 per f.u. in un-substituted LMNF. Therefore, the decrease of locked Li is not caused by the change of high-valent charge compensators.

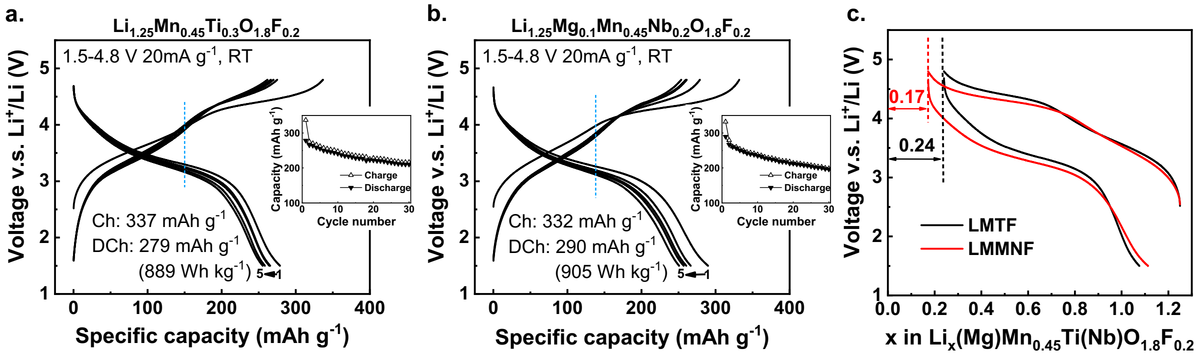

Figure 2-7. Voltage profiles of the first 5 cycles and capacity retention of (a) LMTF and (b) LMMNF within voltage window of 1.5 - 4.8 V at 20 mA g^{-1} at room temperature. The initial charge and discharge capacity and energy density are shown in the figure. (c) Direct comparison of extractable Li ions in LMTF and LMMNF in electrochemical test. The amount of remaining Li content is 0.17/0.24 per f.u. at the top of charge for LMTF/LMMNF, respectively.

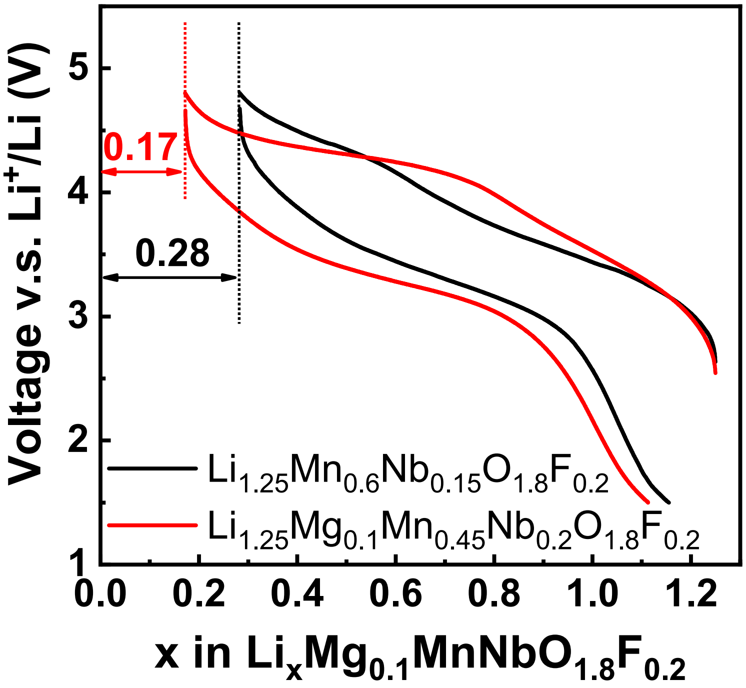

Figure 2-8. Electrochemical performance of Li-(Mg)-Mn-Nb-O-F compounds. First cycle voltage profiles of $Li_{1.25}Mn_{0.6}Nb_{0.15}O_{1.8}F_{0.2}$ (black) and $Li_{1.25}Mg_{0.1}Mn_{0.45}Nb_{0.2}O_{1.8}F_{0.2}$ (red) within voltage window of 1.5 - 4.8V at 20 mA g^{-1} at room temperature. The amount of remaining Li per f.u. at top of charge is shown in the figure.

2.3.4 Extended study on Li/TM substitution

To further illustrate the validity of the Mg-doping strategy and critically examine the Mg-doping effect without the effect of different d^0 TM charge compensators, we further studied the composition $Li_{1.333}Mn_{0.667}O_{1.333}F_{0.667}$ (LMF), [16,66] which shows lower capacity but better capacity retention than the related disordered Li_2MnO_3. LMF delivers a first charge and discharge capacity of 276 mAh g^{-1} and 267 mAh g^{-1} (**Figure 2-9**), respectively, which is lower than that in disordered Li_2MnO_3. [86] This comparison is consistent with our understanding of the role that F plays: its locking effect reduces capacity, but it also mitigates the irreversible oxygen redox process and reduces oxygen loss, which improves cycling. Mg can be introduced in a variety of ways into DRX compounds depending on how charge compensation is achieved. Using the Li-Mn-O-F system as an example, we show below that this degree of freedom can be used to tune the initial capacity versus cyclability, which is summarized in **Table 2-1**. In the previous example, Mg was incorporated by substituting Ti with a charge-equivalent combination of Mg and Nb. Other strategies would be to (1) substitute Mn with Mg, leading to a higher Mn valence and constant Li-excess level; (2) substitute Li with Mg, leading to a lower Mn valence and Li-excess level. To test both strategies, $Li_{1.333}Mg_{0.1}Mn_{0.567}O_{1.333}F_{0.667}$ (ms-LMF) and $Li_{1.233}Mg_{0.1}Mn_{0.667}O_{1.333}F_{0.667}$ (ls-LMF) were prepared by mechanochemical ball-milling. The notation ms-LMF refers to the sample where Mn was substituted by Mg, and the notation ls-LMF refers to the sample where Li was substituted by Mg. To exclude particle size effect on the electrochemical performance, SEM was conducted and these images are shown in **Figure 2-10**.

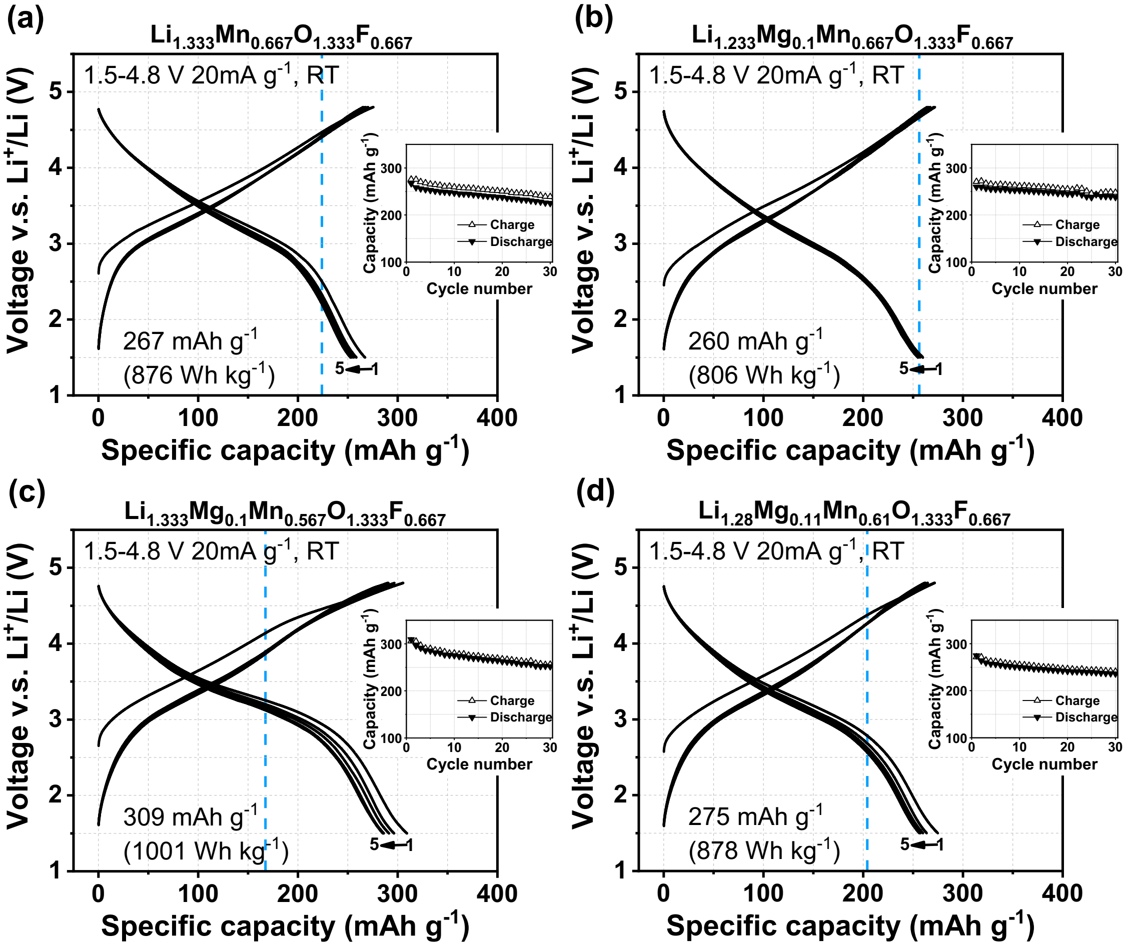

Figure 2-9. Electrochemical performance of Li-(Mg)-Mn-O-F compounds. Voltage profile of the first 5 cycles and capacity retention of (a)LMF, (b) ls-LMF, (c) ms-LMF and (d) LMMF within

voltage window of 1.5 - 4.8V at 20 mA g^{-1} at room temperature. The blue dash lines indicate the theoretical Mn-redox capacity.

Table 2-1: Notation of all compositions chosen in this study. In each case, the compositional design objective is briefly described in the Note.

Notation	Composition	Note
LMTF	$Li_{1.25}Mn_{0.45}Ti_{0.3}O_{1.8}F_{0.2}$	solid-state synthesis, low F content,
LMMNF	$Li_{1.25}$ $Mg_{0.1}Mn_{0.45}Ti_{0.2}O_{1.8}F_{0.2}$	$Ti_{0.3}$ to $Mg_{0.1}Nb_{0.2}$ by charge balanced substitution
LMF	$Li_{1.333}Mn_{0.667}O_{1.333}F_{0.667}$	ball-milling synthesis, high F content,
ls-LMF	$Li_{1.233}Mg_{0.1}Mn_{0.667}O_{1.333}F_{0.667}$	Li to Mg substitution, O redox ↓ , retention ↑
ms-LMF	$Li_{1.333}Mg_{0.1}Mn_{0.567}O_{1.333}F_{0.667}$	Mn to Mg substitution, extractable Li ↑ , capacity ↑
LMMF	$Li_{1.28}Mg_{0.11}Mn_{0.61}O_{1.333}F_{0.667}$	mixed substitution, all Mn3+, non-extractable Li ↓

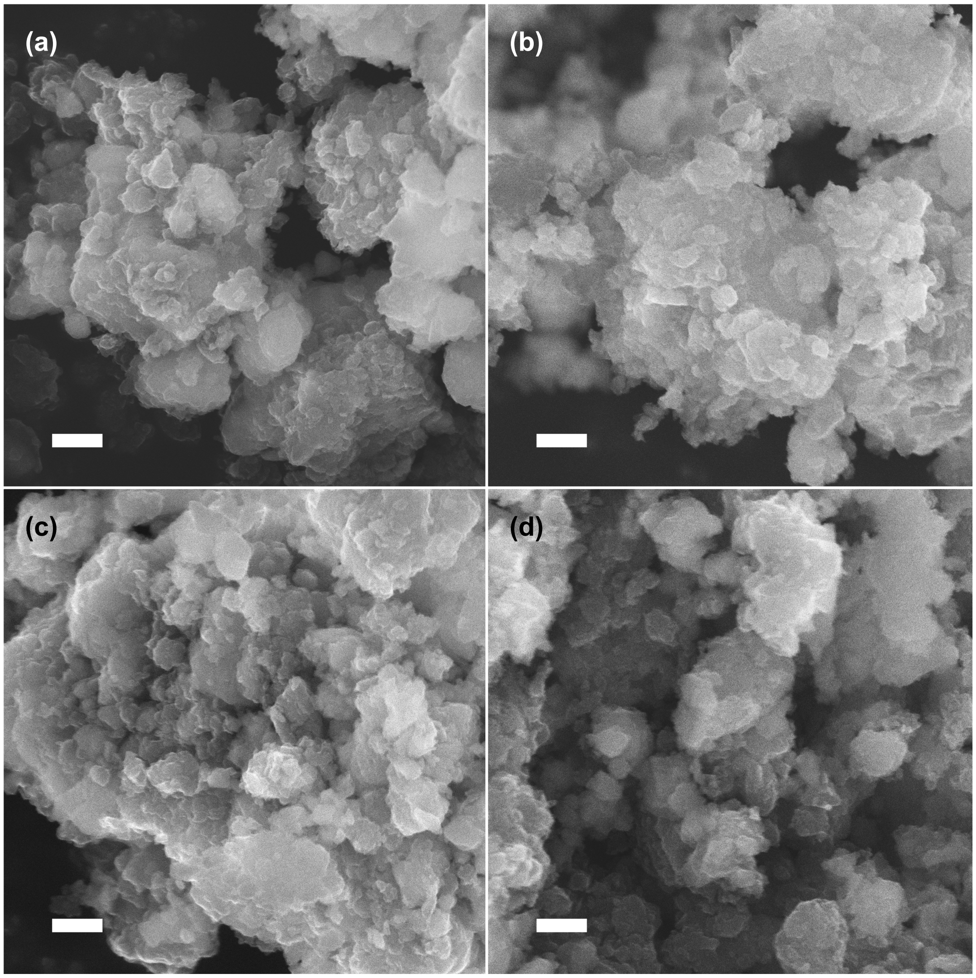

Figure 2-10. Scanning electron microscope (SEM) images of (a) LMF, (b) LMMF, (c) ls-LMF and (d) ms-LMF that show the agglomeration of primary particles into secondary particles (scale bars, 400 nm).

As the Li-excess content remains high in ms-LMF, Mg can free the locked Li to achieve a larger capacity. In agreement with this prediction, ms-LMF exhibits an initial charge (and discharge) capacity of 305 mAh g^{-1} (and 309 mAh g^{-1}), which is larger than for LMF (**Figure 2-9**). Through this substitution strategy, a specific discharge energy of 1001 Wh kg^{-1} can be achieved. With more capacity contribution from anionic redox, a capacity of 252 mAh g−1 is retained (81.6% of the initial capacity) compared to that of LMF (226 mAh g−1, 84.3%) over 30 cycles (**Figure 2-11b**).

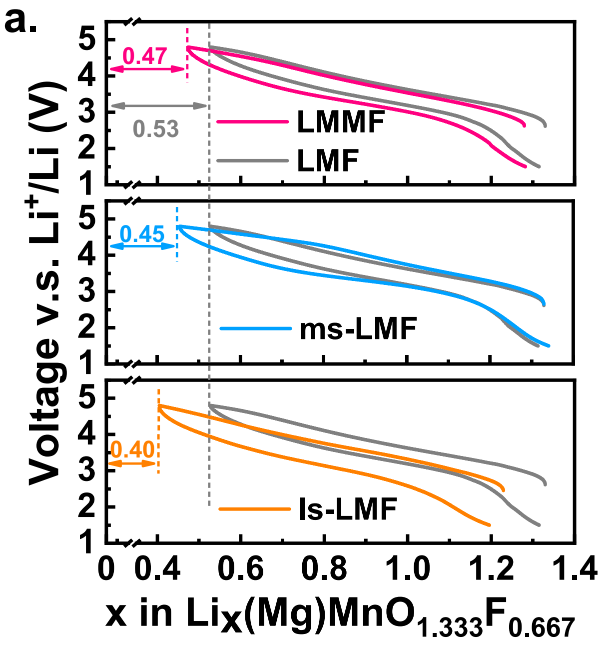

Figure 2-11: (a) Voltage profiles of ls-LMF, ms-LMF, LMMF, and LMF within voltage window of 1.5 - 4.8 V at 20 mA g^{-1} at room temperature. The amount of remaining Li per f.u. at top of charge is shown in the figure. The gray curves represent the first cycle voltage profile of LMF for comparison. (b) Cyclability of all the Li–(Mg)-Mn–O–F compounds at 20 mA g^{-1} at room temperature within a voltage window of 1.5 - 4.8 V.

In contrast, a lower capacity is expected in ls-LMF as it lowers the Li-excess level. Indeed, it delivers initial charge and discharge capacities of 271 mAh g^{-1} and 260 mAh g^{-1} (a specific energy of 806 Wh kg^{-1}), respectively (**Figure 2-9b**). However, the capacity retention of ls- LMF is improved over LMF (248 mAh g^{-1} after 30 cycles, 91.5% of the initial capacity) presumably as a result of the theoretical TM capacity that is gained from Mn by lowering its valence in the as-synthesized sample, leading to less oxygen redox.

These results show the two different Mg substitution strategies in fluorinated Li-excess DRX materials, each serving a different purpose: Mg can either substitute for the TM to free some locked Li, resulting in a higher initial capacity with reasonable capacity retention, or Mg can substitute for Li and lower the TM valence, which increases the theoretical TM capacity and results in improved capacity retention. In both cases, the amount of non-extractable Li is lower than that of undoped LMF. This trade off can be influenced by the fluorination level as show by Lun et al. [66] as a high F content enables one to combine high TM redox capacity with high Li excess. The comparison of cyclability is also shown in **Figure 2-12**.

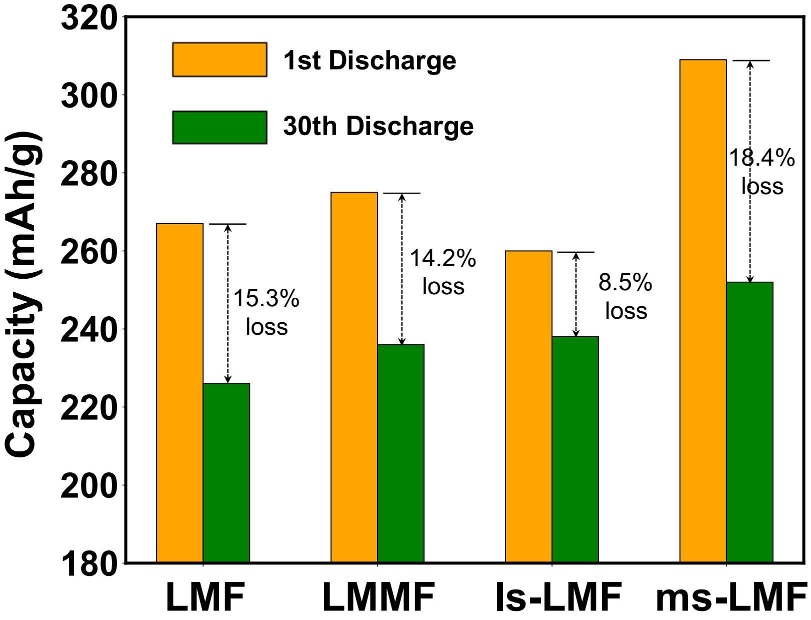

Figure 2-12. Cyclability comparison of LMF-based samples. The first discharge (orange) and the 30th discharge (green) capacity of LMF, LMMF, ls-LMF and ms-LMF samples are shown. The percentage of capacity loss is labeled in figure.

We also considered co-substitution of Li and Mn by Mg. ^{19}F ss-NMR measurements were once again conducted to confirm the bulk incorporation of F (**Figure 2-13**). The voltage profiles of $Li_{1.28}Mg_{0.11}Mn_{0.61}O_{1.333}F_{0.667}$ (LMMF) cycled between 1.5 V and 4.8 V are presented in Figure S4d. LMMF delivered first charge and discharge capacities of 272 mAh g^{-1} and 275mAh g^{-1}, respectively. Over 30 cycles, a capacity of 236 mAh g^{-1} is retained (85.8% of the initial capacity). The capacity retention of LMMF is intermediate between that of ls-LMF and ms-LMF. Although slightly less charge capacity was delivered compared with LMF (276 mAh g^{-1}), the amount of non-extractable Li at the top of charge state decreased from 0.53 Li per f.u. for LMF to 0.47 Li per f.u. for LMMF (**Figure 2-11a**).

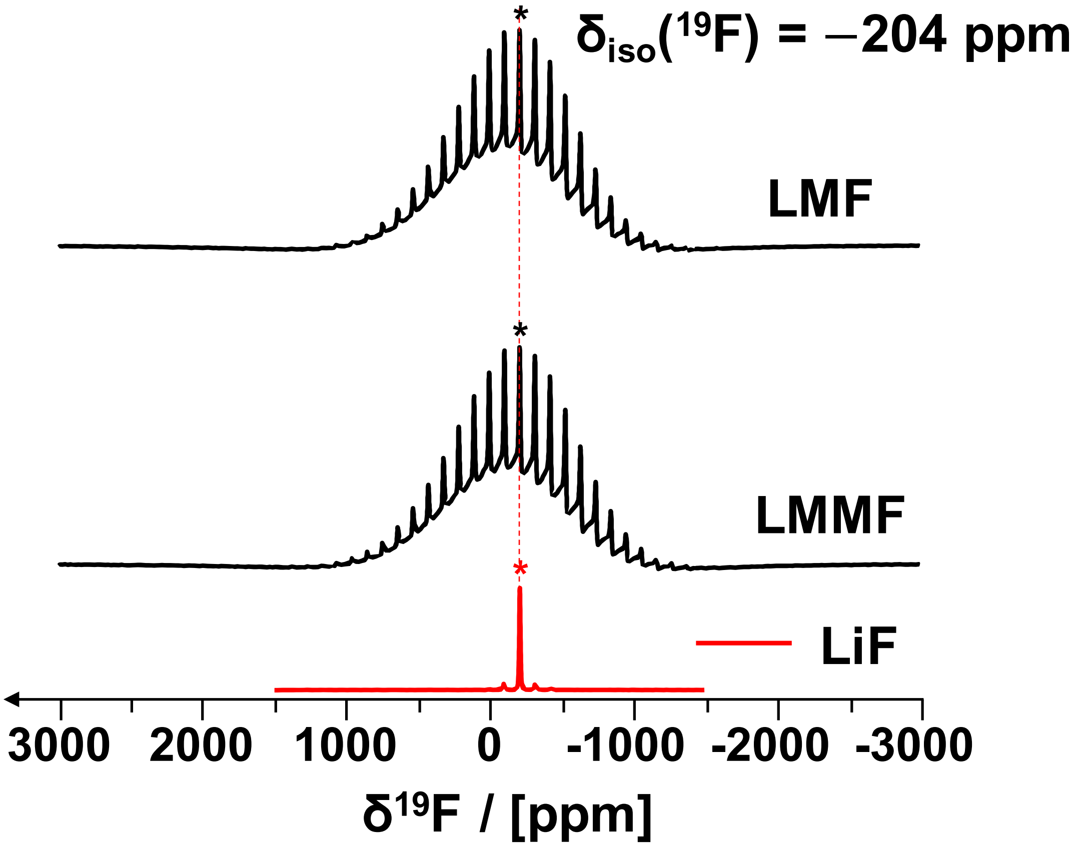

Figure 2-13. ^{19}F spin echo MAS NMR spectra of LMF and LMMF. For comparison, ^{19}F spin echo spectra collected under similar experimental conditions ($B_0 = 7.05$ T) on a LiF powder sample are shown in red. The isotropic shift of the sharp resonance corresponding to ^{19}F nuclei in LiF-like environments in the ^{19}F NMR spectra is denoted with an asterisk. Spinning sidebands due to fast rotation of the samples during data acquisition are observed on either side of the isotropic signals.

To relate the performance of the co-substituted sample to its structure, a CEMC simulation with temperature 1750 °C as a heuristic limit of the mechanical ball-milling condition was run. [9] The transition metals in LMF and LMMF are Mn^{3+} and thus present a simi- lar chemical environment. As shown in **Figure 2-14a**, the frequency of the Li6F configuration is approximately 10% lower in LMMF than in LMF, whereas the frequency of the Li5MF configuration is quite similar in both compounds. The reduced amount of locked Li in Li6F indicates that Li ions have been displaced to other non-locking sites and can thus be effectively extracted within the working voltage window. Considering that the Li-excess amount is different in LMF and LMMF, we introduce a normalized short-range order parameter λ to measure the occurrence of Li6F configuration in the solid solution:

$$\lambda = \frac{P_{calc}(Li6F) - P_{rand}(Li6F)}{P_{max}(Li6F) - P_{rand}(Li6F)}$$

where P_{calc}, P_{rand}represent the calculated and fully random frequency of the Li6F config- uration. P_{max} is the max probability for Li6F that can be achieved for the given Li and F content. For all of our samples, $P_{max} = 1$. In **Figure 2-14b**, the black solid bar represents the direct frequency of the Li6F configuration and the dashed bar represents the normalized SRO parameter λ. The frequency by which the Li6F configuration occurs decreases from 0.41 for LMF to 0.32 for LMMF, and the corresponding SRO parameter λ decreases from 0.35 to 0.28, respectively. Both experimental and computational results confirm that co-substitution of Li/TM with Mg reduces the amount of locked Li.

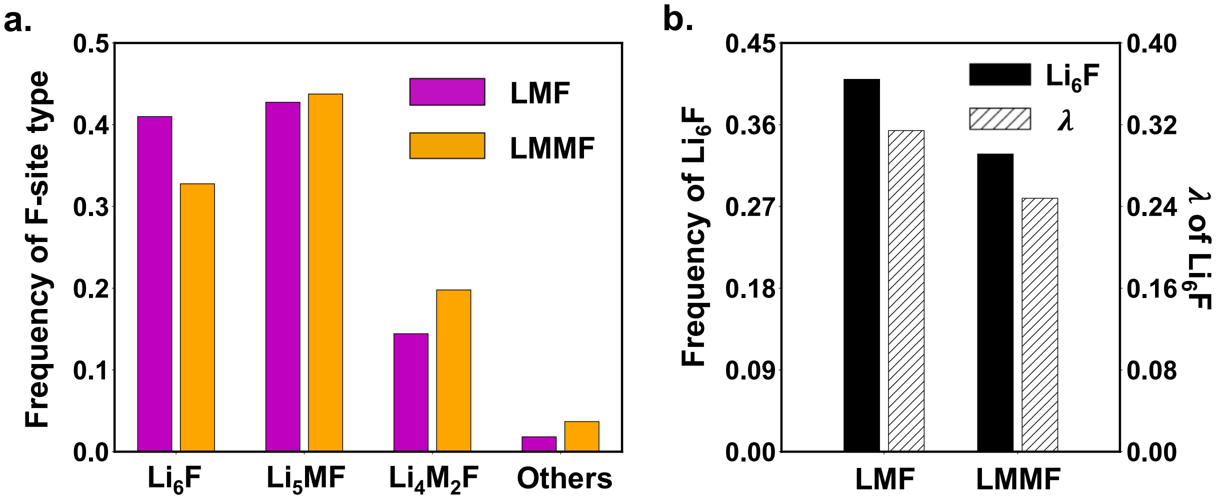

Figure 2-14. (a) Frequency of different types of fluorine environments averaged 1000 sampled structures from CEMC simulation. (b) Frequency and normalized short-range order parameter λ of Li6F environment of LMF and LMMF.

2.4 Discussion

DRX materials require Li excess to achieve a percolating Li diffusion pathway through a low barrier 0-TM migration channel. At least 9% of excess Li is needed when cations are randomly distributed, while more Li content is needed in practical compounds due to short-range order. [9,66] The reduction in electron capacity that this amount of Li excess causes can be countered by the incorporation of high valent metals and by O to F substitution (which both reduce the TM valence state and increase theoretical TM redox), or by relying on oxygen redox to provide extra electron capacity. [17,87] Fluorine substitution is particularly fruitful as it also seems to stabilize the compounds when they have oxygen redox, leading generally to better capacity retention in many systems. [41,85,87]

From previous work it is clear that this strategy is not fully optimized. While the Li-excess is needed for percolation, not all Li near F can be extracted motivating our strategy to displace some of it by adding other metal cations. From our computational investigation we find that Mg is one of the few elements that has the appropriate binding strength with F to displace Li. We find in **Figure 2-7** that when replacing $Ti_{0.3}$ in LMTF with $Mg_{0.1}Nb_{0.2}$ in LMMNF, the non-extractable Li content is reduced by about 30% even though this substitution reduces percolation (**Figure 2-3b**). There are other options to compensate for the introduction of Mg in a DRX materials, such as substituting Li/TM with Mg, and our results show that these different substitution strategies can be used to tune either capacity or capacity retention. Substituting Li leads to better capacity retention because the TM average charge valence is reduced and less irreversible oxygen redox is needed. Substituting the TM leads to higher capacity as the Li-excess level is kept constant and Li-F locking is reduced, resulting in a greater fraction of extractable Li. Particularly, we further demonstrated the validity of Mg doping in the LMMF system by substituting Mg for both Li and TM. Without consideration of the Li-F locking effect, LMMF would be expected to deliver lower capacity because of the lower Li and redox active TM content. However, both computational and experimental results indicate that substituting Mg for both Li and TM effectively unlocks more Li by reducing the frequency of Li6F environments in LMMF, and thus LMMF delivers a comparable charge capacity and higher discharge capacity than LMF. These results unambiguously confirm that it is beneficial to introduce Mg-doping to unlock Li from the Li6F configuration in DRX oxyfluorides.

From our study of the related group of compositions, the best approach to optimize capacity by incorporation of Mg is to (1) keep the Li-excess amount constant, and (2) substitute on the TM (ms-LMF) and/or replace it with a different d0 charge compensator (LMMNF). This strategy leads to an energy density of 905 and 1001 Wh kg^{-1} in the compound LMMNF (solid-state synthesis approach) and ms-LMF (mechanochemical ball-milling approach), respectively.

2.5 Conclusion

In this chapter, we demonstrated the computational prediction and experimental realization of Mg-doped disordered oxyfluoride cathodes with improved electrochemical performance. Although fluorination enhances the long-term performance of DRX materials, the strong attraction of F to Li can make some of the Li ions that are part of a Li6F configuration non-extractable within a reasonable voltage window. Our simulations show that the population of Li6F can be effectively reduced with Mg doping. This is confirmed by experiments on several systematically chosen compositions, successfully demonstrating the validity to unlock Li from the Li6F configuration. From the study of two groups of compositions, we conclude that the amount of locked Li content, should be considered in oxyfluorides to fully optimize the capacity. Mg^{2+} has an ionic radius similar to that of Li^{+} and a strong bonding preference to F, making it a suitable candidate for resolving the Li-F locking effect and increasing the achievable capacity of DRX materials.

Chapter 3 Thermodynamically driven synthetic optimization for DRX cathodes

The work presented in this chapter is based, often verbatim, on the following publication: Cai, Zijian, et al. "Thermodynamically Driven Synthetic Optimization for Cation-Disordered Rock Salt Cathodes." Advanced Energy Materials 12.21 (2022): 2103923.

3.1 Introduction

While composition and structure are typical design handles to modify the properties of materials, it is well established that attributes regulated by the synthesis of a material may also control materials performance in a substantial way. This can include shape and morphology, defects, microstructure, secondary structural variations, etc. How these modify performance depends on the specific properties of interest, but general optimization of these secondary structural features through synthesis is often a process of trial-and-error, with a certain degree of guidance provided by experiment or density functional theory (DFT)-based phase diagram calculation.[13,88-90] Such a "black box" approach to capture the relation between synthesis, products and performance is slow and can miss opportunities to enhance materials properties simply through modifications of the synthesis procedure. Recent advances in the *in situ* observation of materials synthesis foster enhanced understanding towards how it can be controlled by synthesis parameters.[91-96] While most *in situ* synthesis studies performed to date have focused on the phase changes in the synthesis process of the ceramic material itself, we demonstrate in this paper that a more systematic approach can be taken through the convergence of theory and high-resolution characterization methods to relate structural details and performance. Specifically, *in situ* characterization of the synthesis of disordered-rocksalt (DRX) type Li-ion battery cathode materials demonstrates that a crystalline rocksalt forms from the precursors on a very different time scale than the time needed to short-range order the cations in this rocksalt, providing an opportunity for creating DRX materials with enhanced performance by stopping the synthesis early to freeze the material in a metastable state of disorder.

Li-excess DRX materials are a young family of next-generation Li-ion cathode materials, in which there are no well-separated Li or transition metal (TM) sublattices.[28,35,85,97] These materials are promising cathode compounds as they remove the dependence on Co and Ni [61,85], crucial to maintain the structure in layered cathode materials.[98] The performance of DRX materials is strongly connected to details of their structure through the statistics of the local cation environments that form in the structure upon synthesis: Li ions migrate through a percolating network of tetrahedral 0-TM units where a lack of TM presence around the activated state facilitates migration of Li through the tetrahedral site.[34,35] However, DRX cathodes can suffer from poor rate capability when unfavorable local short-range order (SRO) which reduces the amount of 0-TM environments is present.[10,14,65,67,85] SRO has been proven to be crucial in controlling the Li transport and thus the capacity and rate capability in DRX cathodes, the appropriate manipulations of which can lead to significant enhancement of the electrochemical performance.[59,99]

We selected a representative DRX composition of $Li_{1.2}Mn_{0.55}Ti_{0.25}O_{1.85}F_{0.15}$ (LMTF), consisting of earth-abundant and inexpensive transition metals and tracked the structure, especially the generation and evolution of the SRO during the synthesis, using a combination of *in situ* and *ex* *situ* characterization techniques, including transmission electron microscopy (TEM) electron diffraction (ED), X-ray diffraction (XRD), and synchrotron pair distribution function (sPDF) analysis. It is observed that while the long-range DRX structure forms rapidly during synthesis, the generation of SRO occurs over a longer time scale, enabling us to obtain DRX compounds with identical composition but different degrees of SRO by controlling the sintering time at high temperature. Specifically, LMTF sintered at 1000 °C for 35 min [denoted as LMTF (35 min)] displays significantly less SRO than LMTF sintered for 4 h [denoted as LMTF (4 h)], and consequently, LMTF (35 min) exhibits greatly enhanced electrochemical performance in terms of both capacity (specific energy) and rate capability as compared to LMTF (4 h). First-principles calculations are used to clarify the very different timescale for rocksalt and short-range order formation. This example highlights the opportunities in the synthetic optimization of functional ceramic materials by combining computation, *in situ* and multi-modal synthesis observation, and structure-property models for the performance of the material.

3.2 Methodology

3.2.1 Experimental methodology

3.2.1.1 Synthesis

The LMTF compounds were synthesized using a traditional solid-state method with different sintering time. Li_2CO_3 (Alfa Aesar, ACS, 99% min), Mn_2O_3 (Alfa Aesar, 99.9%), TiO_2 (Alfa Aesar, 99.9%), and LiF (Alfa Aesar, 99.99%) were used as precursors. All the precursors were stoichiometrically mixed in ethanol with a Retsch PM 400 planetary ball mill at a rate of 180 rpm for 12 h. 15% excess Li_2CO_3 was added to compensate for possible loss during synthesis, especially during the 600°C-holding process. The precursors were then dried in an oven at 70°C overnight and pelletized. The precursor pellets were first heated to 600°C with Ar gas flow at a rate of 5 °C/min and held for 1 hour to decompose carbonate species. The pre-heated pellets were then covered with Ni foil and sealed in quartz tubes filled with Ar with an ampoule sealing system. The tubes were further heated to 1000°C at a rate of 5 °C/min, followed by different sintering time. This set up allows a more accurate control of the sintering time at 1000°C. The sealed tubes with wrapped pellets were quenched to room temperature at designated time, transferred to a glovebox, and ground into powders.

Lab XRD patterns were obtained using a Rigaku Miniflex 600 or Bruker D8 ADVANCE diffractometer (Cu source) in the 2θ range of 15–90°. Rietveld refinement was performed using PANalytical X'pert HighScore Plus software. Elemental analysis was performed using direct current plasma emission spectroscopy (PerkinElmer Optima 5300 DV Optical Emission Spectrometer) for lithium, titanium, and manganese. SEM images were collected using a Zeiss Gemini Ultra-55 analytical field-emission SEM at the Molecular Foundry at Lawrence Berkeley National Lab (LBNL). Particle size analyses were performed by ImageJ, with more than 100 particles evaluated.

3.2.1.2 Electrochemistry

All the cathode films were free-standing and composed of the active materials, Super C65 (Timcal), and polytetrafluoroethylene (PTFE, DuPont, Teflon 8A) at a weight ratio of 60:30:10. To make the cathode films, 300 mg of the as-synthesized active materials and 150 mg of Super C65 were mixed and shaker-milled for 90 min in an argon atmosphere using a SPEX 800M mixer/mill. PTFE was later added and manually mixed with the shaker-milled mixture for 40 min. The components were then rolled into thin films inside a glovebox. Commercial 1 M $LiPF_6$ in ethylene carbonate (EC) and dimethyl carbonate (DMC) solution (1:1 volume ratio) was used as the electrolyte. A glass microfiber filter (Whatman) was used as the separator. FMC Li metal foil was used as the anode. Coin cells were assembled inside the glovebox and tested on an Arbin battery test instrument at 25°C. The loading density of the films was approximately 3–4 mg cm^{-2} based on the active materials. For the rate-capability tests, a smaller loading density of approximately 2.5 mg cm^{-2} based on the active materials was used. The specific capacities were calculated based on the weight of active materials (60%) in the cathode films. For the GITT measurements, each step in the voltage profiles corresponds to a galvanostatic charge/discharge of 10 mAh g^{-1} at a rate of 20 mA g^{-1} followed by a 6 h relaxation step.

3.2.1.3 TEM characterization

The high-angle annular dark-field scanning transmission electron microscopy (HAADF-STEM), energy dispersive spectroscopy and electron diffraction characterization for both *ex situ* and *in situ* experiments were performed using an FEI TitanX 60-300 microscope equipped with Bruker windowless EDX detector at an accelerating voltage of 300 KV in the Molecular Foundry at LBNL.

The *in situ* heating experiments were performed on a Protochips Fusion Select holder. The pre-heated LMTF pellet (600°C in Ar atmosphere for 1 hour) was grinded into fine powder, diluted in hexane, sonicated to obtain good particle dispersion, and then drop casted on a Protochips Fusion Thermal E-chip. The Thermal E-chips comprise a central conductive ceramic membrane supported by a silicon substrate. Nine 8-micron holes covered with ~18 nm holey carbon film were located in the center of the membrane to provide an electron transparent area for TEM imaging. Joule heating occurs when electrical current is forced across the conductive membrane. For *ex situ* characterization, the TEM samples were prepared by drop casting the dilute LMTF dispersion onto a standard 400 copper mesh TEM grid with lacey carbon support.

3.2.1.4 *Ex-situ* synchrotron XRD and PDF

Synchrotron XRD and PDF measurements were performed at beamline 11-ID-B at the Advanced Photon Source (APS) of Argonne National Laboratory using a constant wavelength of 0.2115 Å. The sample-to-detector distances were 180 mm for PDF and 1000 mm for XRD. All *Ex situ* samples were packed into Kapton capillaries (Cole-Parmer) and sealed with epoxy in an Ar-filled glovebox. The total scattering data was integrated using GSAS-II software to obtain 1D XRD spectra and *G(r)* was obtained using xPDF suite package. A CeO_2 standard was used for calibration and to determine the instrumental parameters. PDF fitting was conducted using PDFGui software package. The PDF spectra were refined against a completely random DRX structure model with Fm-3m space group in a short *r*-range between 1.8 and 15 Å. Only scale factor, lattice constant (a), peak shape factor (δ_1^*), and isotropic thermal displacement parameter (U_{iso}) were allowed to refine. U_{iso} was constrained to be the same on the same lattice position. The site occupancies of different atoms were set to the target values and not refined.

3.2.2 Computational methodology

A cluster expansion model has been constructed to produce the structure with SRO in the $Li_{1.2}Mn^{3+}_{0.55}Ti^{4+}_{0.25}O_{1.85}F_{0.15}$ compound. In such a cluster expansion, the configurational energy dependence is captured by an expansion into different cluster functions, which can be formulated as [100,101]:

$$E = \sum_{i,sp1} J_i^{sp1}\sigma_i^{sp1} + \sum_{i,j,sp1,sp2} J_{ij}^{sp1sp2}\sigma_i^{sp1}\sigma_j^{sp2} + \sum_{i,j,k,sp1,sp2,sp3} J_{ijk}^{sp1sp2sp3}\sigma_i^{sp1}\sigma_j^{sp2}\sigma_k^{sp3} \dots\dots$$

Here, σ_i^{sp} corresponds to the occupancy of a certain site(s) with a certain species *sp* and *J* refers to the effective cluster interactions (ECIs).

In a DRX material, a cation site can be occupied by Li^{+}, Mn^{3+} and Ti^{4+} while the anion sites can be occupied by either O^{2-} or F^{-}. For each system, pair interactions up to 7.1 Å, triplet interactions up to 4.0 Å, and quadruplet interactions up to 4.0 Å based on a rocksalt lattice with a cubic lattice parameter a = 3.0 Å were included in the cluster-expansion formalism. The ECIs were fitted to DFT energies of sampled structures using a L1-regularized least-squares regression approach[102], with the regularization parameters selected to minimize cross-validation error [60,102-106]. The DFT results of 1251 structures are applied to fit the cluster expansion, which end up with a cluster expansion model that has root-mean-squared error of 7.53 meV/atom.

Special quasi-random structures (SQSs) are periodic structures whose atomic distributions are selected such that the cluster correlations approach the expected value in a random atomic arrangement as closely as possible for a given structure size[107]. Given this feature, SQSs are an appropriate choice to investigate the properties of rocksalt materials with full disorder. In the alloy community, for example, SQSs have been successfully used to evaluate mixing enthalpies[108] and to model the electronic structure of random alloys[109]. Our previous studies on DRXs using SQS structures also indicate that these structures can be effective tools for quantifying the phase stability[110], electronic structure[17], and voltage curves[111,112]. To model the random cation distribution of the fully disordered rocksalt materials, we generated SQS structures for the example composition, i.e., $Li_{1.2}Mn^{3+}_{0.55}Ti^{4+}_{0.25}O_{1.85}F_{0.15}$, with a 2×4×5 supercell of rocksalt primitive cell (80 atoms).

First-principles density functional theory (DFT) calculations were performed to obtain an accurate description of the structural energies and oxidation states of the different cathode materials. All the calculations were performed using the projector-augmented wave (PAW) method[113] as implemented in the Vienna Ab initio Simulation Package (VASP)[114]. A rotationally averaged Hubbard U correction[115,116] was used to correct the self-interaction error on the transition metals in the compound. The U parameters were obtained from a previously reported calibration to oxide formation energies[116]. For all the calculations, a reciprocal space discretization of 25 k-points per Å^{-1} was applied, and the convergence criteria were set as 10^{-6} eV for electronic loops and 0.02 eV Å^{-1} for ionic loops. The reaction energy is normalized by the cation amount.

3.3 *In-situ* transmission electron microscopy

TEM ED can detect both the long-range crystal structure and the short-range local ordering in the material and present this information in a visual manner, as demonstrated in previous studies.[10,117] Here, we adopted a Protochips Fusion *in situ* heating TEM holder (shown in **Figure 3-1A**) in the transmission electron microscope, which allows us to simultaneously track the evolution of both the long-range order (LRO) and SRO in the same particle *in situ* upon heating by acquiring ED. The heating profile applied in the experiment is shown in **Figure 3-1B**, with red points indicating when an ED pattern was collected on the same particle (except for the 4 h sample, which was collected *ex situ*). In addition, the elemental distribution of Mn and Ti during the ramping process was tracked using scanning transmission electron microscopy (STEM)–energy-dispersive spectroscopy (EDS) mapping. The result, shown in **Figure 3-2**, indicates that the incorporation of the Mn and Ti precursor mainly occurs above 800 °C, consistent with previous reports that the synthesis of DRX materials usually requires a high temperature of approximately 1000 °C.[85,97]

The structural evolution within a representative particle was tracked during heating at 1000 °C. ED patterns along the [100] zone axis of the particle were acquired at times of 5 min, 15 min, and 35 min, as shown in **Figure 3-1C–E**. The sample that was heated for 4 h at 1000 °C was measured *ex-situ* (**Figure 3-1F**) due to the change of orientation of the particle upon heating, which moved beyond the tilting limit of the holder to track the same zone axis. In the ED patterns, the round Bragg diffraction spots represent long-range crystal structural information, which can be indexed to the *Fm-3m* space group and originate from the average rocksalt structure in all four patterns. This result suggests that the LRO in the DRX compound forms rather rapidly during the synthesis and at a relatively low temperature before reaching 1000 °C. The square-like diffuse scattering intensities in the ED patterns are attributed to SRO. The intensity of the diffuse scattering can be integrated within the dashed rectangular regions and compared during different stages of the synthesis, as displayed by the intensity profiles next to each ED image. It is clearly observed that the diffuse scattering patterns gradually emerge with sintering time. At 5 min, there is barely any diffuse scattering present; however, as the sample spends more time at 1000 °C, the diffuse scattering intensity increases, becoming rather pronounced at 4 h, which is the typical time scale adopted in the synthesis of DRX compounds reported previously.[23,41,85] This observation indicates that the SRO formation in DRX compounds is a slow process, in sharp contrast to the formation of LRO, which occurs rapidly.

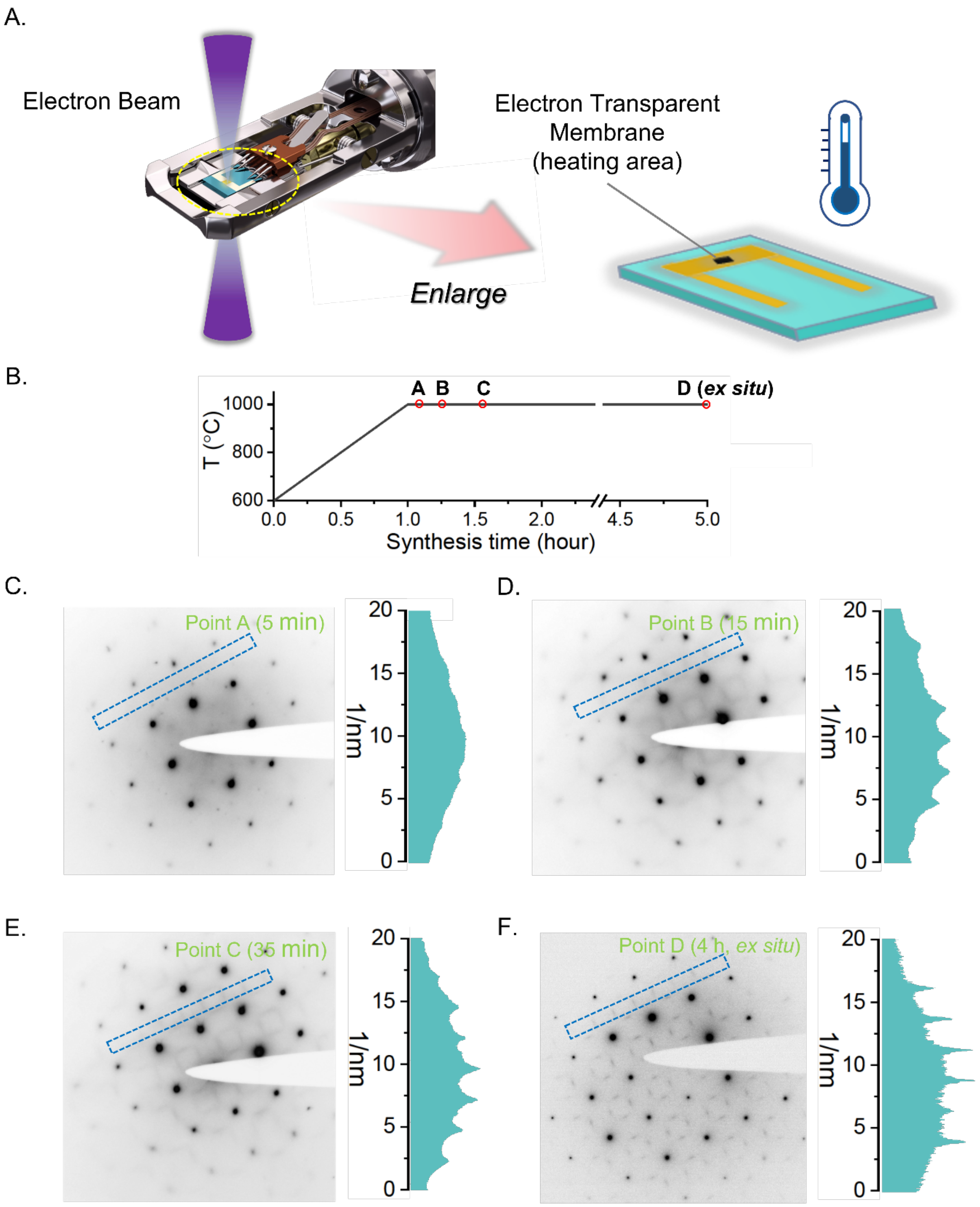

Figure 3-1. ***In situ* temperature-dependent TEM characterization of the synthesis process of LMTF. (A)** Schematic illustration of the *in-situ* temperature-dependent TEM setup. The area of heating with an electron transparent membrane is enlarged. **(B)** Heating profile of pre-heated LMTF 'precursor'. The red circles mark the times at which ED patterns were collected. **(C–E).** TEM–ED patterns collected on the same particle at different times [**(C)** 5 min; **(D)** 15 min; **(E)** 35 min] along the [100] zone axis. **(F)** TEM–ED pattern of the sample with a sintering time of 4 h collected *ex situ*. The round spots, which originate from the LRO in the materials, are indexed to the Fm-3m space group. The square-like diffuse scattering patterns are attributed to the SRO. Quantifications of the SRO pattern intensity by integrating the counts within the dashed rectangular regions are displayed next to the ED patterns.

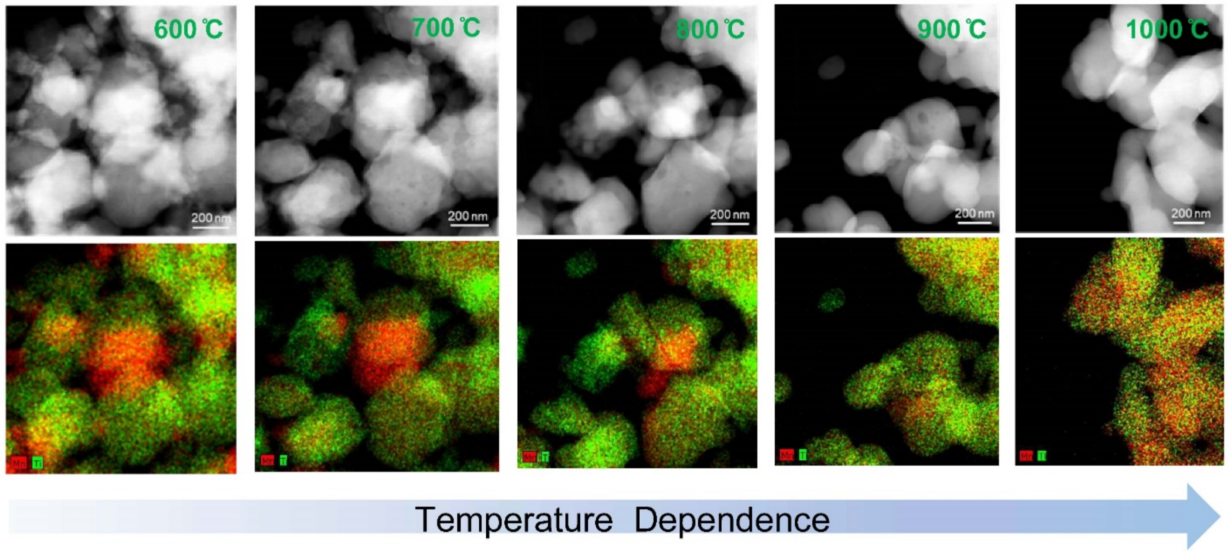

Figure 3-2. STEM images and EDS elemental mapping of Ti and Mn within a fixed region at various temperatures upon heating in *in situ* experiment. Red represents the distribution of Mn, and green represents that of Ti. The incorporation of Mn-rich and Ti-rich particles mainly occurs above 800°C, accompanied by a morphology change. A uniform elemental distribution between Mn and Ti can be observed at 1000 °C. To avoid effect of IR-radiation on the X-ray spectra, all the EDS data is collected after quenching the sample to room temperature.

3.4 Synchrotron-based characterization

To supplement our TEM observations with more bulk sensitive information regarding the structural evolution upon heating, synchrotron-based XRD and PDF were further performed to analyze the long-range crystal structure and short-range local ordering, respectively. This objective would ideally be achieved via an *in situ* experiment; however, this attempt was unsuccessful because of the reactivity between our materials and the quartz capillaries used as sample holders in the *in-situ* flow-cell setup at the beamline.[118] Instead, we probed the LRO and SRO using *ex-situ* XRD and PDF by selecting seven points in the synthesis process, focusing on the region of interest at high temperature: ramped to 900 °C, ramped to 1000 °C (without holding), ramped to 1000 °C followed by holding for 5 min, 15 min, 35 min, 1 h, and 4 h. The details of the sample preparation are described in the methodology section.

Figure 3-3A presents the synchrotron XRD spectra of the seven samples (marked by red circles on the heating profile shown in **Figure 3-3C**). These results confirm that the rocksalt-type LRO forms rapidly and at a temperature before reaching 900 °C. Upon further ramping and sintering at 1000 °C, the LRO of the material no longer changes, as demonstrated in the *ex-situ* XRD spectra, with no observable peak shift observed for all seven samples. Additional Bragg peaks from unreacted Li_2CO_3 and LiF precursors can also be observed in all samples, marked by triangles and asterisks, respectively, which suggests the existence of small amount of Li_2CO_3 and LiF impurities ranging from 3~8%. The degree of SRO at different stages of the synthesis was qualitatively evaluated by fitting the synchrotron PDF results at low r values (between 1.8 and 15 Å) using a random structure. A smaller R_w factor from the fitting would thus suggest a smaller deviation from a random structure, i.e., less SRO. **Figure 3-3B** presents the fitting results for the samples held for 5-min, 35-min, and 4-h as representatives, with the results for the remainder of the samples and refined parameters presented in the supplementary information (**Figure 3-4**, **Table 3-1**). The R_w factors are summarized in **Figure 3-3C** and demonstrate an overall increasing R_w factor as the holding time at 1000 °C increases. Investigating the PDF fit in more detail shows that the largest mismatch between the experiment and fitting for samples held longer occurs at very small r (between 1.8 and 4.5 Å) which originates from the local metal rearrangements to form SRO. The PDF results suggest that SRO in LTMF forms in a comparatively slow manner during the synthesis, which is consistent with our *in-situ* TEM observations.

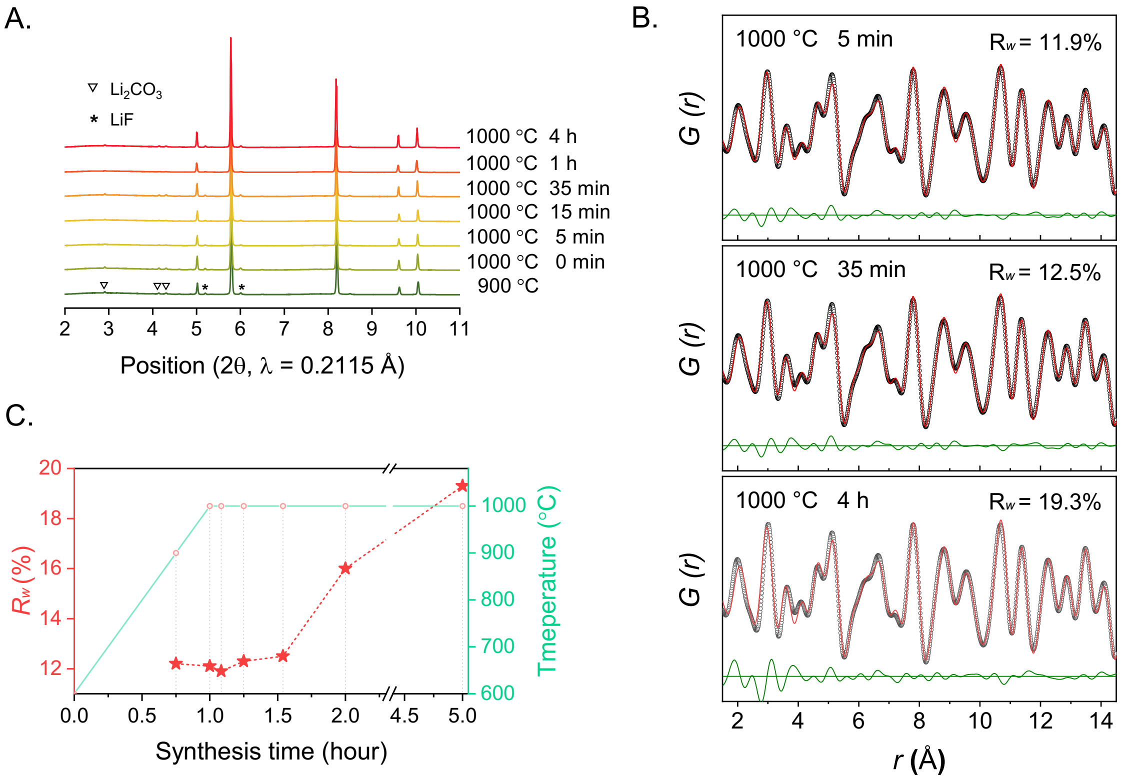

Figure 3-3. Synchrotron-based characterization of LMTF at different stages of synthesis. (A) *Ex situ* XRD results at seven different stages of synthesis: ramped to 900°C, ramped to 1000°C (without holding), and ramped to 1000°C followed by holding for 5 min, 15 min, 35 min, 1 h, and 4 h. Peaks from small amount of unreacted Li_2CO_3 and LiF precursors are marked by triangles and asterisks, respectively. **(B)** sPDF fitting results of samples sintered at 1000°C for 5 min (upper panel), 35 min (middle panel), and 4 h (lower panel) using a random structure. The experimental data are plotted as black open circles, the fittings are plotted as solid red lines, and the difference between observation and calculation is plotted as solid green lines. **(C)** Summary of R_w factors obtained from each PDF fitting at various stages of the synthesis. The synthesis profile is also overlaid, with red circles marking the points of data collection. The grey dashed lines are displayed to guide the eye.

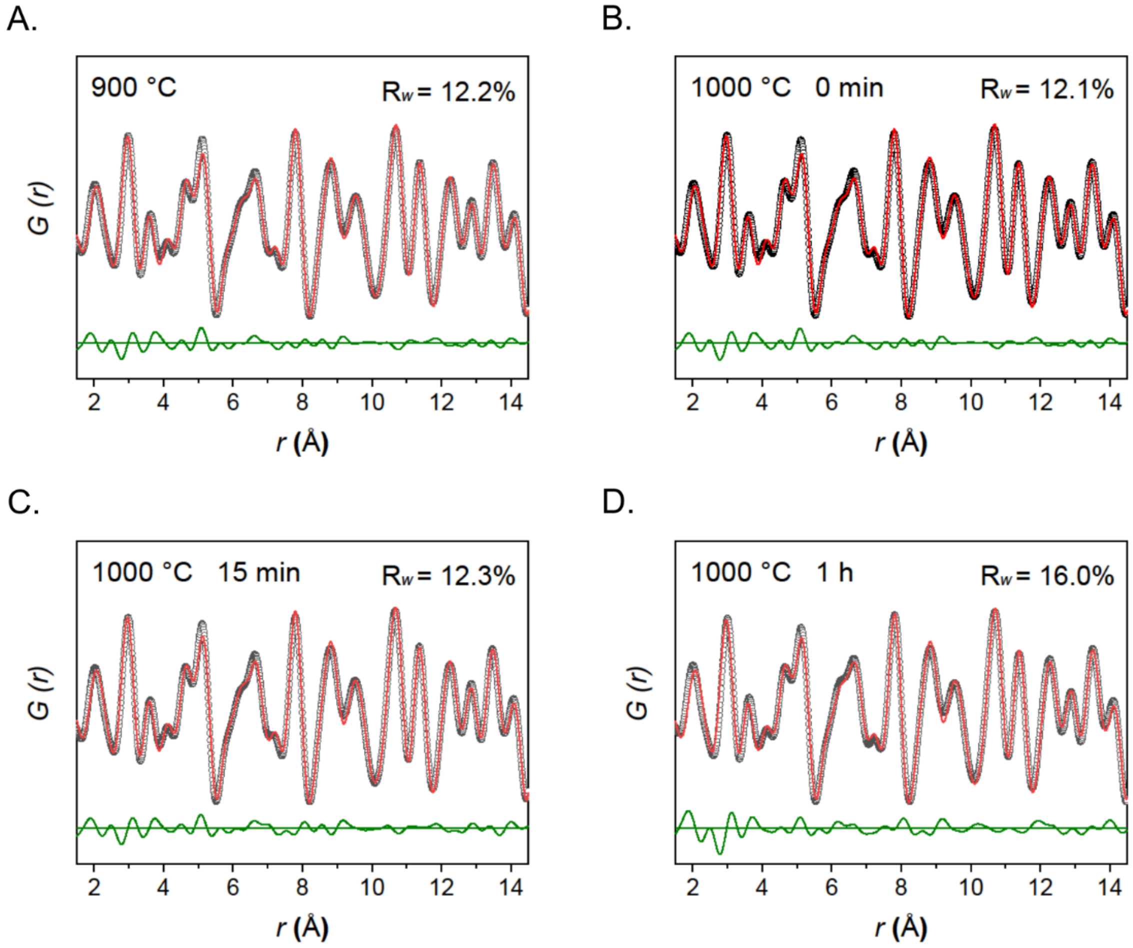

Figure 3-4. Additional sPDF fitting results of LMTF samples collected at different stages during the synthesis. SPDF fitting results of samples (A) ramped to 900 °C; (B) ramped to 1000 °C without holding; and (C–D) ramped to 1000 °C followed by holding for (C) 15 min and (D) 1 h using a random DRX structure (without SRO). The experimental data are plotted as black open circles, the fittings are plotted as solid red lines, and the difference between observation and calculation is plotted as solid green lines. The sample sintered for 1 h (Fig. D) shows a larger deviation from a random structural model, as demonstrated by the larger R_w factor relative to those of the rest of the samples, which mainly originates from the small *r* value region between 1.8 and 4.5 Å. This suggests the growth of SRO upon extended heating during the synthesis.

Table 3-1. Target versus measured atomic ratios of the as-synthesized LMTF (35min) and LMTF (4h).

Materials	Target atomic ratio (Li : Mn : Ti)	Measured ratio (Li : Mn :Ti)
LMTF 35min	1.2 : 0.55 : 0.25	1.221 : 0.541 : 0.238
LMTF 4h	1.2 : 0.55 : 0.25	1.214 : 0.547 : 0.239

3.4 Computational rationalization

Previous work has shown that thermodynamic driving forces, when evaluated under the appropriate conditions, can rationalize the evolution of phases in a synthesis mixture.[94,95,119,120] We calculated the grand potential of the entire system (open to CO_2 release) relative to the precursors in the random rocksalt and the short-range ordered rocksalt. The energy scale was normalized by the number of cations. The random rocksalt was modelled by a special-quasi-random structure with 40 cations (including Li^+, Mn^{3+} and Ti^{4+}) which maximizes cation randomness in the unit cell. The short-range ordered state and its free energy at 1273 K were determined using the cluster expansion technique as detailed in the Methods section. The results are shown in **Figure 3-5** as blue circles at -5.40 eV/cation for the random rocksalt and at -5.48 eV/cation for the short-range ordered rocksalt, enabling us to sketch a semi-quantitative energetic landscape along the reaction pathway of LMTF.

As **Figure 3-5** shows, a very large energy decrease is associated with the formation of the random rocksalt from the precursors (−5.4 eV/cation ≈ 522kJ/cation mole) explaining why it may form rapidly and at a relatively low temperature. In contrast, short-range ordering the cations from the random rocksalt into the LMTF with SRO decreases the energy by only about 0.076 eV/cation (≈ 7.3kJ/cation mole). This low driving force is likely what is responsible for the long time needed to form SRO. These driving forces revealed by the calculations results are well in line with the experimental observations and indicate a thermodynamic origin of the structural evolution observed during synthesis.

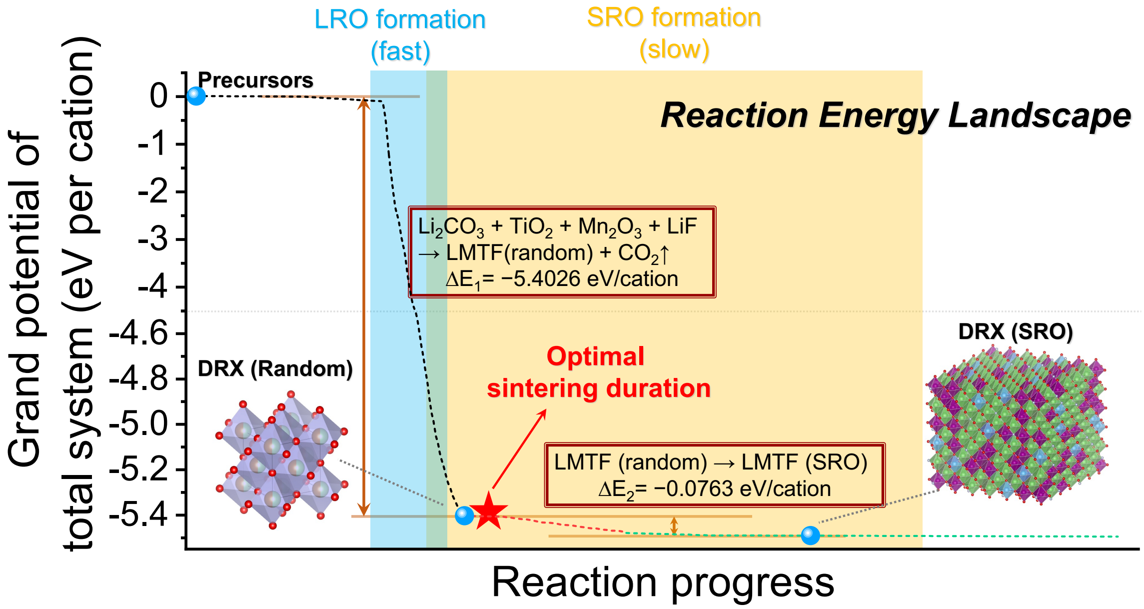

Figure 3-5. Schematic of the reaction energy in the LMTF synthesis process. The grand potential evolution of the total system is computed *ab initio* for the random rocksalt and the short-range ordered rocksalt (simulated at 1273 K), and schematically interpolated (with dashed line). Note that two different energy scales are used (separated at −4.5eV) to highlight the small energy decrease in the SRO formation.

3.4 Demonstration of the synthetic optimization strategy

The different time scales for the formation of the random rocksalt and the short-range ordered structure offers a unique opportunity to optimize the electrochemical performance of the material through modification of its synthesis protocol. Since SRO tends to reduce Li percolation channels and therefore capacity and rate capability in a DRX cathode material [10,66,67,99], we adjusted the synthesis protocol by shortening the sintering time with the objective of obtaining a DRX structure with reduced SRO. We compare the performance of LMTF samples sintered at 1000 °C for 35 min [LMTF (35 min)] and 4 h [LMTF (4 h)]. We selected the LMTF (35 min) sample based on the thermogravimetric analysis (shown in **Figure 3-6**) to keep the overall compositions of the two materials as close as possible, as there was almost no observable weight change of the material (<0.5%) after sintering at 1000 °C for 35 min. Additional elemental analyses were also conducted (shown in **Table 3-2**), which further confirm that LMTF (35 min) and LMTF (4 h) have similar compositions that are close-to-target. Scanning electron microscopy (SEM) and statistical particle size analysis shown in **Figure 3-7** and **3-8**, respectively, demonstrate that the two samples are similar in terms of particle size both in the as-synthesized state and after the shaker milling used for electrode fabrication. We should thus be able to attribute any difference in electrochemical performance to the different degree of SRO present in the two samples (confirmed *ex-situ* as shown in **Figure 3-9**).

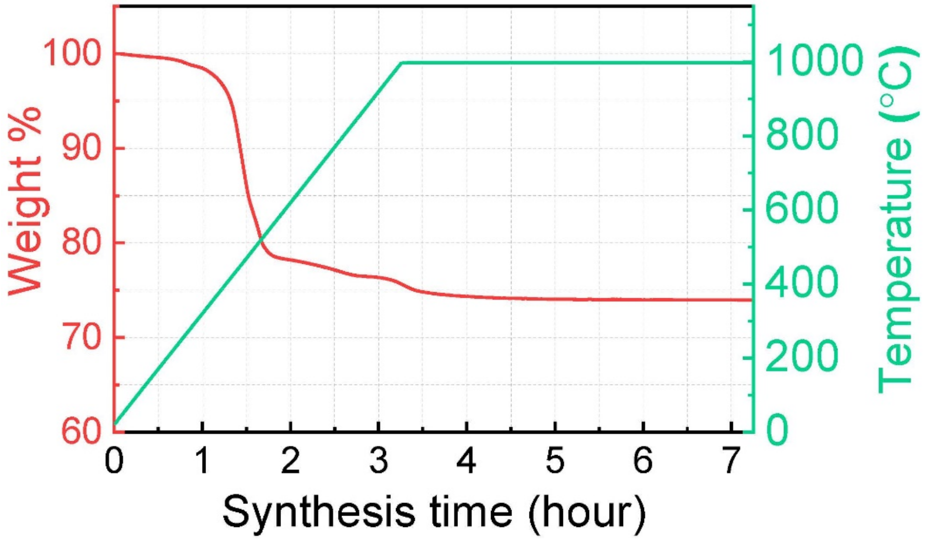

Figure 3-6. Thermogravimetric analysis results during the synthesis of LMTF. The red curve shows the weight change of the precursors upon heating, and the green curve is the heating profile. A ramping rate of 5°C min^{-1} was applied followed by a 4-h holding at 1000°C in an Ar atmosphere. The weight of the powder barely changed after heating at 1000°C for approximately 35 min.

Table 3-2. Refinement results of X-ray PDF data for LMTF compound quenched from different stages during the synthesis. The PDF spectra were refined against a completely random DRX structure model with Fm-3m space group in a short *r*-range between 1.8 and 15 Å.

Samples	Space group	*a* (Å)	δ_1^*	U_{iso} (Å^2)	R_w (%)
900 ˚C	Fm-3m	4.193	0.501	0.0086	12.2
1000 ˚C 0 min		4.194	0.512	0.0090	12.1
1000 ˚C 5 min		4.193	0.505	0.0087	11.9
1000 ˚C 15 min		4.190	0.529	0.0084	12.3
1000 ˚C 35 min		4.191	0.527	0.0096	12.5
1000 ˚C 1h		4.190	0.545	0.0092	16
1000 ˚C 4h		4.193	0.571	0.0084	19.3

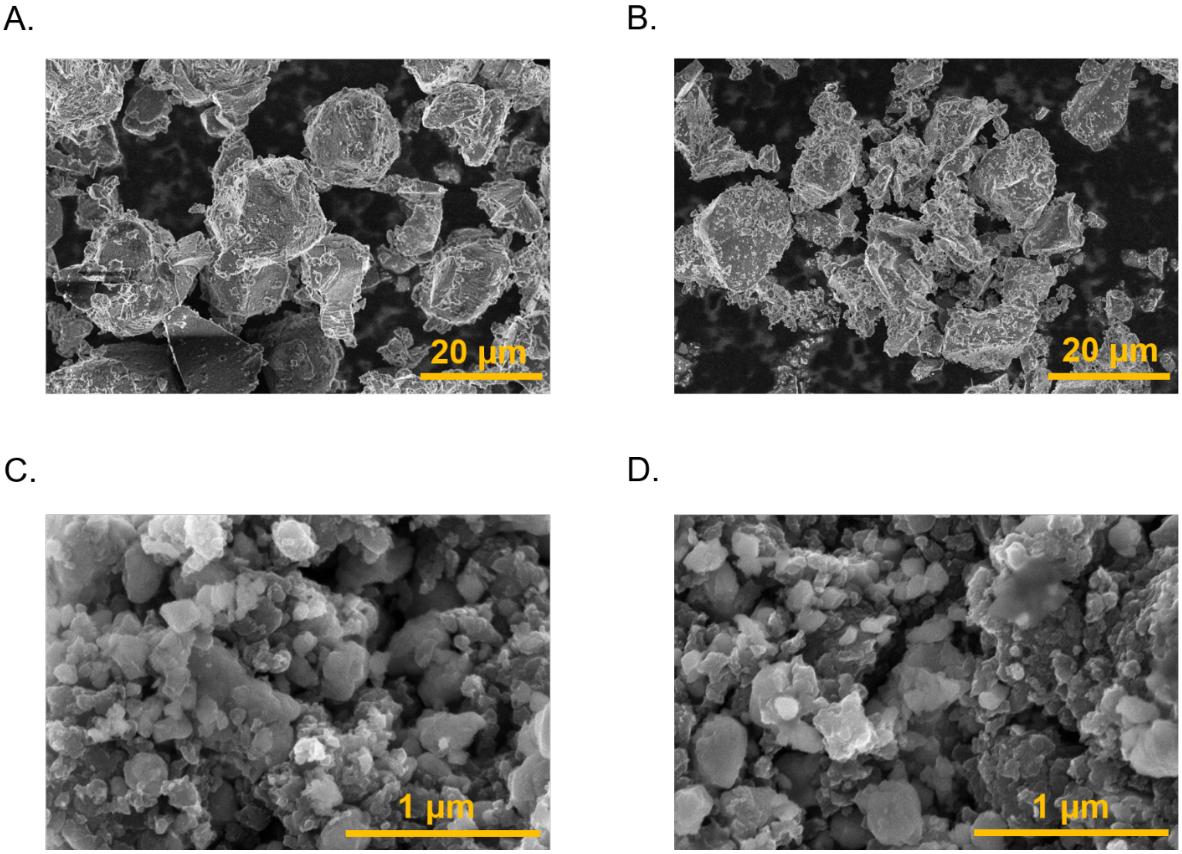

Figure 3-7. SEM images of as-obtained (A) LMTF (35 min) and (B) LMTF (4 h) and shaker-milled (C) LMTF (35 min) and (D) LMTF (4 h) with carbon black. Both samples had similar particle sizes both as-obtained (5–20 µm) and after ball-milling (200–400 nm).

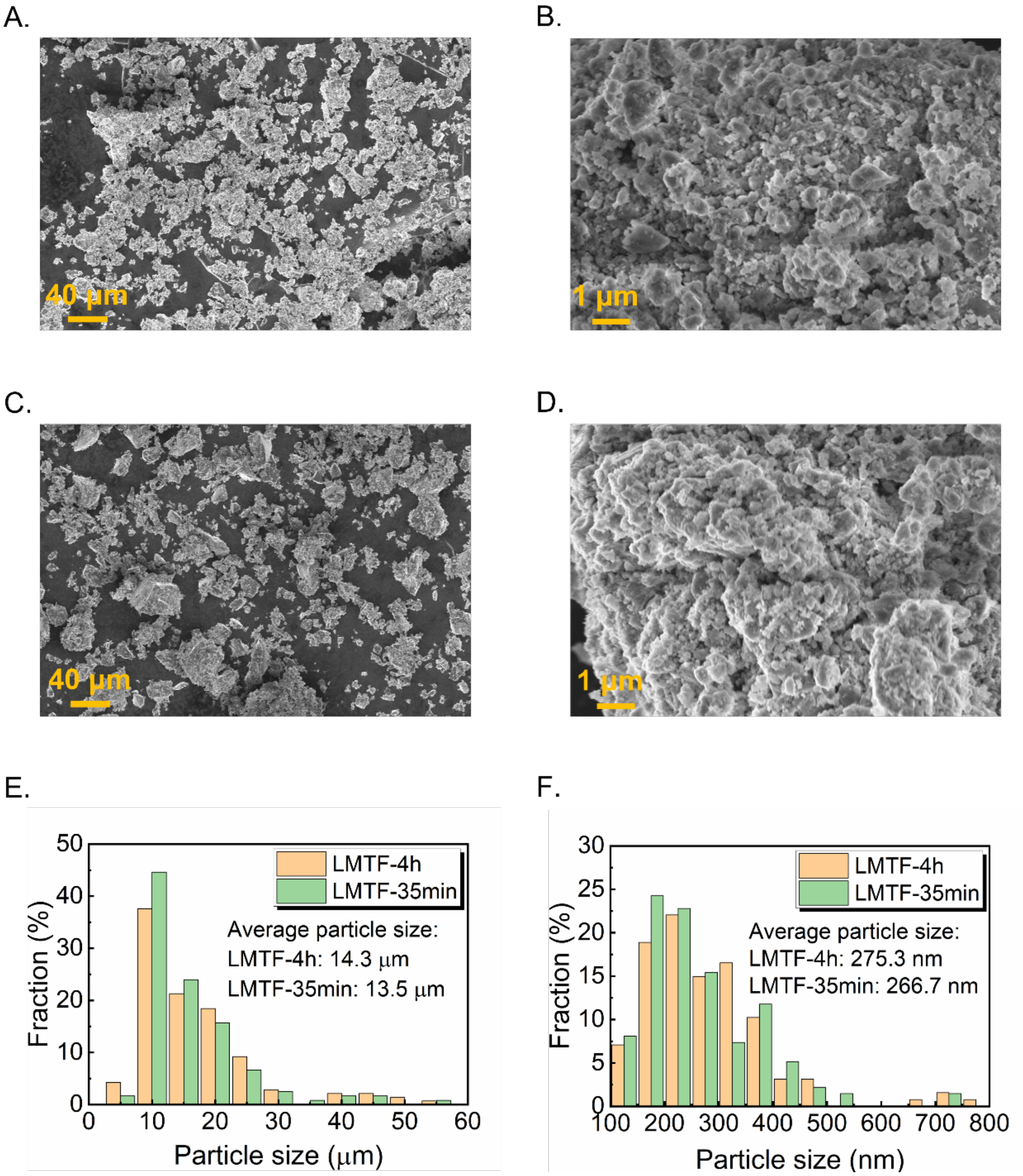

Figure 3-8. Particle size analyses of LMTF (35min) and LMTF (4h). SEM images of as-synthesized **(A)** LMTF (35min) and **(C)** LMTF (4h). SEM images of shaker-milled **(B)** LMTF (35min) and **(D)** LMTF (4h) without carbon black. Statistical analyses of the particle sizes of **(E)** LMTF (35min) and **(F)** LMTF (4h) obtained from Figures **(A)**-**(D)**, which confirm that LMTF (35min) and LMTF (4h) are similar in particle size both at as-synthesized state and after shaker-mill.

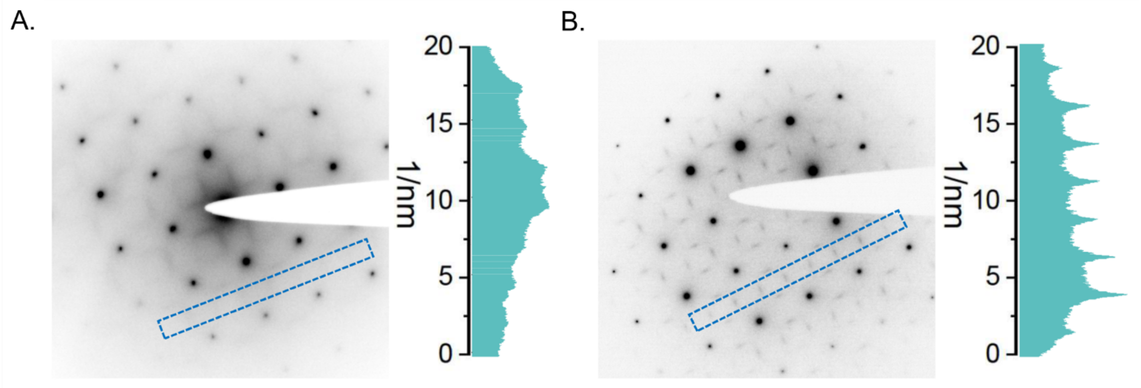

Figure 3-9. *Ex situ* TEM ED patterns. ED patterns were collected for **(A)** LMTF (35 min) and **(B)** LMTF (4 h) along the [100] zone axis. The round spots, which originate from the LRO in the materials, are indexed to the Fm-3m space group. The square-like diffuse scattering patterns are attributed to the SRO. Quantifications of the SRO pattern intensity by integrating the counts within the dashed rectangular regions are displayed next to the ED patterns. It can be observed that LMTF (35 min) has significantly less SRO than LMTF (4 h), which further supports our *in situ* observation.

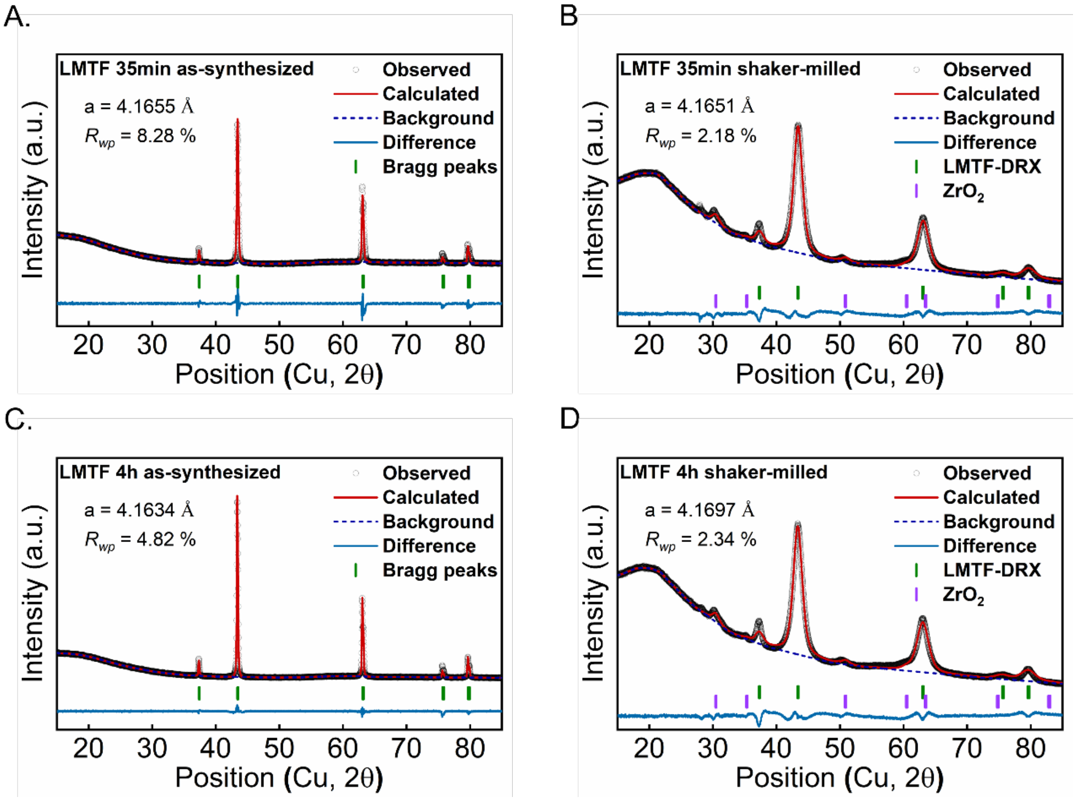

Figure 3-10. Lab XRD patterns and Rietveld refinement of the as-synthesized and shaker-milled LMTF. (A) as-synthesized and **(B)** shaker-milled LMTF (35min); **(A)** as-synthesized and **(B)** shaker-milled LMTF (4h). ZrO_2 phase observed in the shaker-milled samples is from the Spex mill jar and balls. It can be observed that the lattice constant of both materials remains almost unchanged after the milling process. The crystallinity of the materials decreases after the shaker mill process as indicated by the peak broadening and intensity decrease of Bragg peaks.

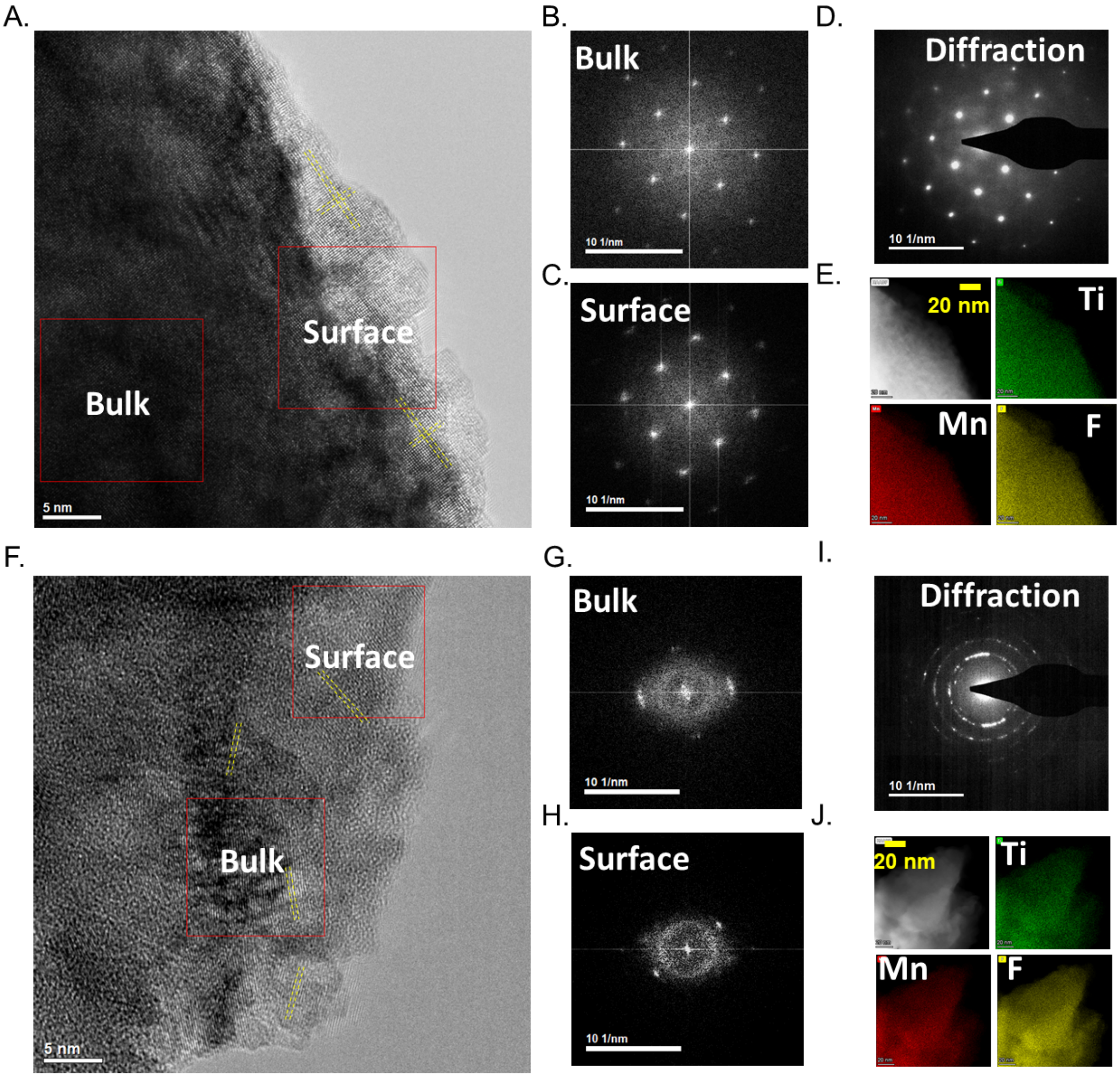

Figure 3-11. TEM characterization of as-synthesized and shaker-milled LMTF (35min). (A) TEM image of an as-synthesized LMTF (35min) particle (close to surface). Yellow dashed lines mark the lattice orientation. Fast Fourier-transformed (FFT) images of the dashed regions close to the particle (B) surface and (C) bulk in Figure (A). (D) Electron diffraction collected on the particle in Figure (A). (E) EDS elemental mapping of Mn, Ti and F in another as-synthesized LMTF (35min). (F) TEM image of a shaker-milled LMTF (35min) particle (close to surface). Yellow dashed lines mark the lattice orientation at different regions of the particle. FFT images of the dashed regions close to the particle (G) surface and (H) bulk in Figure (F). (I) Electron diffraction collected on the particle in Figure (F). (J) EDS elemental mapping of Mn, Ti and F in another shaker-milled LMTF (35min).

Additional XRD and TEM characterizations of LMTF (35min) and LMTF (4h) were conducted to discuss the structural change during the shaker mill process (**Figure 3-10, 3-11**). The as-synthesized LMTF (35min) shows good crystallinity and a clean surface as confirmed by the same crystal orientation at various regions of the particle (**Figure 3-11A**), as well as the sharp signal in the fast Fourier-transformed (FFT) images (**Figure 3-11B-C**) and electron diffraction (ED) pattern (**Figure 3-11D**). STEM EDS mapping demonstrates a uniform elemental distribution of Mn, Ti and F (**Figure 3-11E**). After shaker-mill, the material becomes more poly-crystalline, showing various local domains with different crystal orientations (**Figure 3-11F**). The poly-crystalline feature of the shaker-milled sample is also supported by the ring-like FFT images (**Figure 3-11G-H**) and ED pattern (**Figure 3-11I**). The uniform elemental distribution of Mn, Ti and F (**Figure 3-11J**) is kept during the shaker mill.

The electrochemical performance of the two samples was evaluated using galvanostatic cycling and is shown in **Figure 3-12**. When cycled between 1.5 and 4.8 V at a rate of 20 mA g^{-1}, LMTF (35 min) exhibits a very high capacity (specific energy) of 313 mAh g^{-1} (987 Wh kg^{-1}) (**Figure 3-12A**), which is significantly larger than that of LMTF (4 h) (273 mAh g^{-1} (852 Wh kg^{-1})) (**Figure 3-12B**). This finding is consistent with the design principle of DRX materials that the mitigation of unfavorable SRO improves the overall Li transport by forming a better-extended Li percolation network, thus leading to an improved capacity. Further support for the influence of the synthesis time on performance is given by the high rate performance: LMTF (35 min) delivers 143 mAh g^{-1} at a very high rate of 2,000 mA g^{-1} (**Figure 3-12C**), which is more than 40% larger than that delivered by LMTF (4 h) (101 mAh g^{-1}, **Figure 3-12D**). We also characterize the rate capability of LMTF (35 min) and LMTF (4 h) using a “slow-charge, fast discharge” protocol, i.e., charging both materials to a capacity of 250 mAh g^{-1} at 20 mA g^{-1}, rest for 1 hour and then discharging at 20 mA g^{-1}, 500 mA g^{-1}, and 2 A g^{-1}, respectively (**Figure 3-13**). With the same charge capacity, LMTF (35min) still demonstrates a comparable or larger discharge capacity in all rates, especially at a higher rate. Additional Galvanostatic intermittent titration (GITT) measurements of LMTF (35min) and LMTF (4h) were conducted, as presented in **Figure 3-14**, which confirm that LMTF (35min) generally has a lower overpotential and higher Li diffusivity than LMTF (4h). These results prove the success of the synthetic optimization strategy to shorten the sintering duration at high temperature, uncovered by systematically investigating the structural evolution of the material during the synthesis process. This enhancement in electrochemistry does not require any compositional modification and basically comes ‘for free’ as one only needs to keep the sample in the furnace for a shorter time, which potentially can increase throughput when cathode synthesis is scaled up.

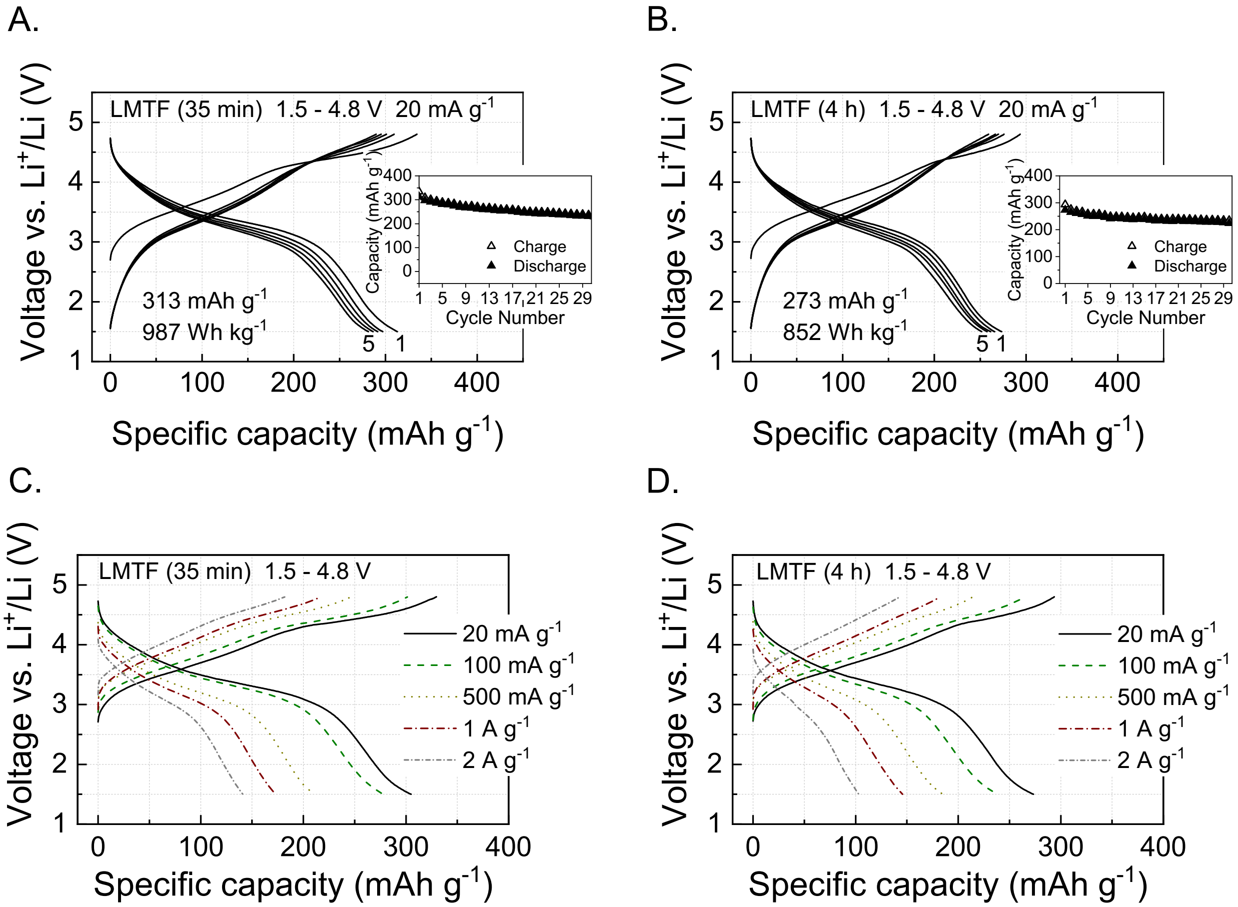

Figure 3-12. Electrochemical performance of LMTF (35 min) and LMTF (4 h). Voltage profiles and capacity retention of **(A)** LMTF (35 min) and **(B)** LMTF (4 h) within the voltage window of 1.5–4.8 V at 20 mA g^{-1} and 25°C. Rate capability of **(C)** LMTF (35 min) and **(D)** LMTF (4 h): the first-cycle voltage profiles when cycled between 1.5 and 4.8 V at 20, 100, 500, 1000, and 2000 mA g^{-1}.

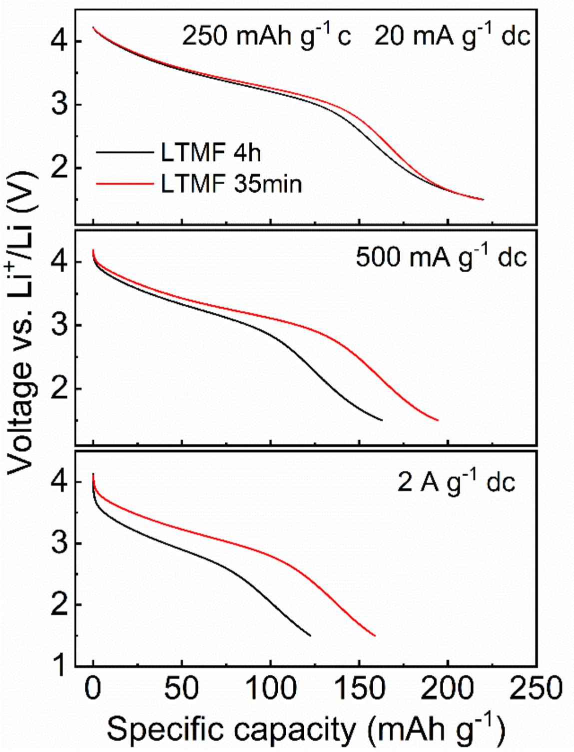

Figure 3-13. Rate capability test of LMTF (35min) and LMTF (4h) using a different protocol. Both materials were charged to a capacity of 250 mAh g^{-1} at 20 mA g^{-1}, rest for 1 hour and then discharged at 20 mA g^{-1}, 500 mA g^{-1}, and 2 A g^{-1}, respectively. All discharge curves are displayed.

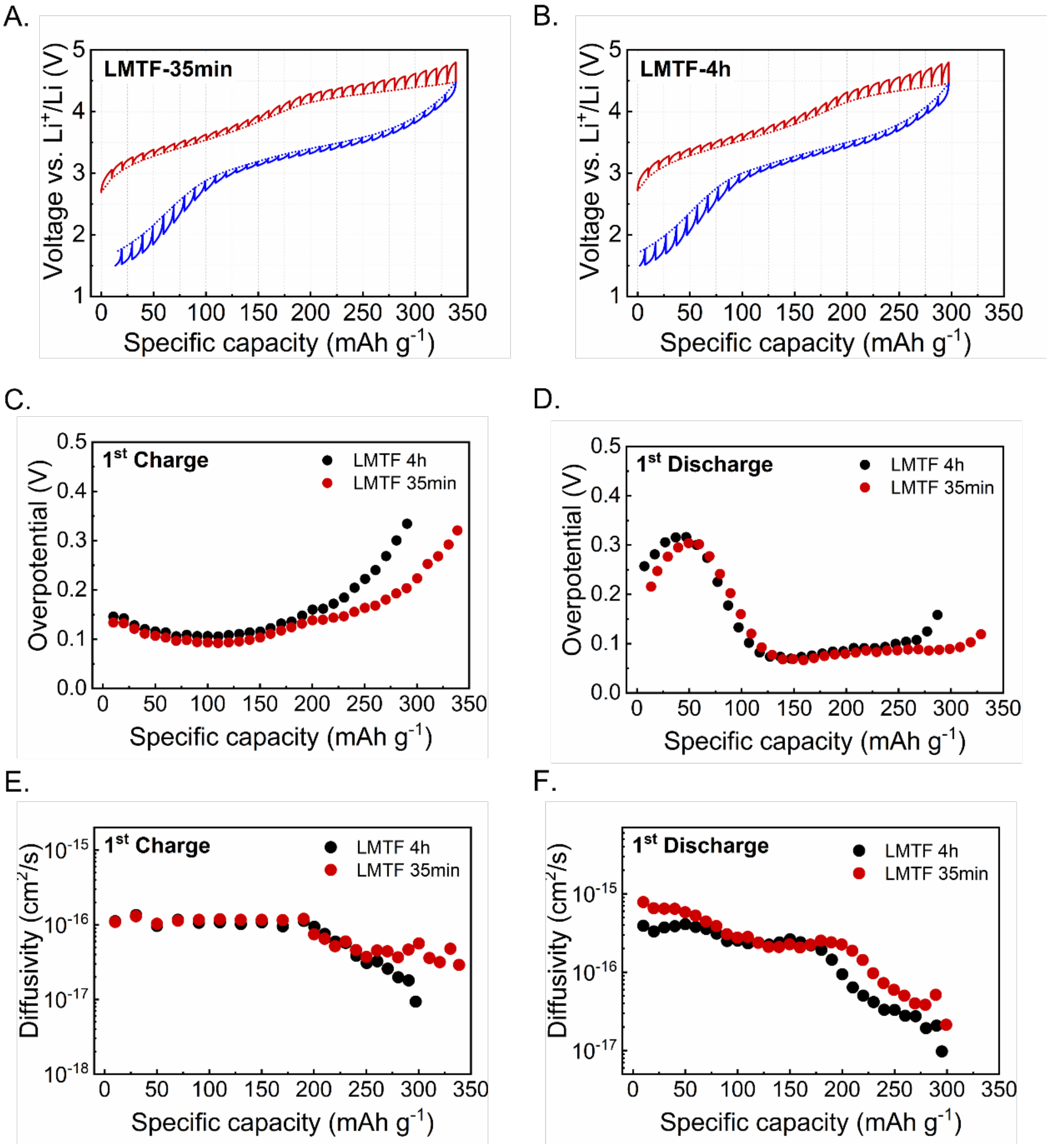

Figure 3-14. GITT analyses of LMTF (35min) and LMTF (4h). First-cycle voltage profiles of **(A)** LMTF (35min) and **(B)** LMTF (4h) from GITT tests. Each step in the GITT voltage profiles corresponds to a galvanostatic charge/discharge of 10 mAh g^{-1} at a rate of 20 mA g^{-1} followed by a 6-h relaxation step. The overpotentials at each step for LMTF (35min) and LMTF (4h) during 1st **(C)** charge and **(D)** discharge. Li diffusivity derived from GITT measurements for LMTF (35min) and LMTF (4h) during 1st **(E)** charge and **(F)** discharge. It can be observed that LMTF (35min) generally shows a lower overpotential and larger Li diffusivity compared to LMTF (4h).

3.5 Conclusion

The performance of functional materials often depends on minor details of their structure such as compositional inhomogeneities, point defects, or in the case presented here, short-range cation order. While computational modeling and high-resolution characterization techniques can be used to identify such structural features, controlling them in the production of materials is often difficult.

Recent advances to track the structural evolution via diffraction or spectroscopy techniques have started to provide a much more detailed picture of how compounds form [92,95,96,119,120], enabling targeted optimization of the synthesis protocol, such as wisely selecting suitable precursor sets, and accurately controlling the temperature and synthesis time to obtain metastable phases. This approach becomes even more instructive when combining synthetic optimization with functional enhancement, as demonstrated in this work. By tracking the detailed structural features of a multi-component oxyfluoride, especially the formation of SRO in DRX materials, we identify that unlike LRO, which forms rapidly and at a relatively low temperature, SRO evolves slowly at high temperature consistent with the very different energy scale associated with SRO and LRO. Taking advantage of this observation, we proposed a synthetic optimization strategy to quench the sample at an early stage of high-temperature sintering when LRO has formed without extensive SRO, creating a DRX material with enhanced capacity and rate capability. The SRO-optimized LMTF (35 min) sample exhibits a capacity of >310 mAh g^{-1} and a specific energy close to 1000 Wh kg^{-1} and enables discharge up to 2 A g^{-1}, making it a promising Li-ion cathode composed of only inexpensive and earth-abundant Mn and Ti.

We also believe such methodology of synthesis-induced functional improvement can be applied to other classes of functional materials and speed up the targeted optimization of their synthetic protocols and functional enhancement. For instance, in Ni-rich Ni–Mn–Co (NMC)-type Li-ion cathodes, the interlayer mixing between Li and Ni has been closely linked to the Li-transport and capacity degradation of the material, which is sensitive to the synthesis condition.[121,122] Systematic tracking of the Li/Ni mixing behavior upon synthesis may enable us to improve the synthesis protocol and mitigate such unfavorable cation mixing. Single-atom doping in 2D materials, such as graphene or MoS_2, has been proven effective to enhance certain functionalities such as catalytic activities.[123-125] *In situ* tracking of the incorporation of the dopant atoms during synthesis using local structural characterization techniques may provide useful insight for controlling the doping sites and concentration into the matrix and ultimately lead to improved functionalities. We are thus eager to see more of such functional optimization of ceramic materials assisted by "opening the black box" of synthesis.

Chapter 4 Realizing continuous cation order-to-disorder tuning in a class of high-energy spinel-type Li-ion cathodes

The work presented in this chapter is based, often verbatim, on the following publication: Cai, Zijian, et al. "Realizing continuous cation order-to-disorder tuning in a class of high-energy spinel-type Li-ion cathodes." Matter 4.12 (2021): 3897-3916.

4.1 Introduction

While Lithium-ion (Li-ion) batteries are the ubiquitous energy storage solution for portable electronics in our modern society. Over the next decade, the demand for Li-ion technology is projected to further grow more than tenfold [2], largely driven by the electrification of transportation. Meanwhile, several other market segments that are still in their early stage of development, including residential and grid-scale storage, may further open up if battery costs continue to drop. The rapid scale-up in Li-ion production brings new challenges of supply and resource sustainability, especially for cobalt and nickel, which are the two major components for cathode fabrication.[2] Most of the conventional cathode materials, including $LiCoO_2$ and $Li(Ni,Co,Mn)O_2$ (NMC), are based on a layered crystal structure, in which Li and TM form alternating layers to enable facile Li transport in a 2D open space. This layered structure necessitates the use of Ni and Co as redox active elements, as other transition metals migrate into the Li layer in either their oxidized or reduced state.[126] To ensure energy security and alleviate supply chain risks, the structural and chemical diversity of cathode compounds needs to be broadened. In this work, we show that considerable opportunity exists in the continuum between well-ordered spinels and disordered rocksalts.

Spinel exhibits the same anion (oxygen) sublattice as the layered structure but a different cation order. In a perfectly ordered spinel $LiTM_2O_4$, Li and TM occupy the tetrahedral 8a and octahedral 16d sites, respectively. The structure is advantageous for transport as Li ions can diffuse in local channels that do not face-share with TM ions [34] and interconnect to form a 3D percolating network. However, for the most common spinel cathode, $LiMn_2O_4$, only half of the potential Li capacity can be practically utilized due to a first-order phase transition that occurs near 3 V (versus Li^+/Li) once the compound is lithiated beyond the $LiMn_2O_4$ composition. This phase transition, coupled with the Jahn-Teller distortion of Mn^{3+}, leads to poor kinetics and poor cyclability.

Converting the two-phase regions into a continuous solid solution is expected to reduce capacity loss (due to the reduction of strain upon cycling) and improve kinetics. Past efforts have focused on partial substitution of Jahn-Teller-inactive elements for Mn^{3+} in the 16d site, keeping the 8a fully occupied by Li. For example, substituting Ni^{2+} for Mn^{3+} results in partial or complete TM mixing in the 16d site and converts the 4 V plateau into a solid-solution region.[127] Yet the two-phase region near 3 V is retained.[56] Substituting Li^+ for Mn^{3+} is more efficient in tuning the reaction thermodynamics. Previous operando neutron studies indicated that $Li_{1.1}Mn_{1.9}O_4$, with 5% Li-for-Mn substitution undergoes a pure solid-solution reaction at the 4 V plateau [128], unlike $LiMn_2O_4$. Further increasing Li substitution leads to the Li-rich limiting composition $Li_4Mn_5O_{12}$, which can be cycled between $Li_2Mn_5O_{12}$ and $Li_{6.5}Mn_5O_{12}$ with some capacity coming from oxygen redox.[57] Nevertheless, the two-phase behavior still appears when the Mn valence drops below 3.5.[58] Recently, it has been demonstrated that ultrahigh energy and power density can be achieved in a class of partially-(dis)ordered Li-Mn-O-F spinels with as much as 20% Li-for-Mn substitution and significant cation over-stoichiometry.[59] Fluorination is applied to reduce the overall Mn valence, thereby increasing the theoretical transition metal capacity. Previous work has also demonstrated that fluorination mitigates irreversible oxygen loss and increase average Li insertion/extraction voltage.[12,13,19,41,87] Fluorination and Li-for-Mn substitution also separates the composition where all octahedral sites are filled from the composition where all Mn^{3+} is Jahn-Teller active, limiting the way in which these two effects strengthen the two-phase reaction in $LiMn_2O_4$. The materials presented in this work exhibit cation disorder that is no longer confined to the 16d site but also involves the 8a and 16c sites. Since the two-phase reaction at ~ 3 V upon lithiation for a classic well-ordered $LiMn_2O_4$ cathode originates from a collective migration of Li from the 8a site to the 16c site, the partial cation (transition metal) disorder introduced between the 16d and the 16c sites is expected to reduce this collective behavior and possibly convert the two-phase reaction into a solid-solution reaction. Indeed, nearly smooth voltage profiles are observed in the materials we tested, indicating the absence of two-phase regions, along with exceptionally high capacity and energy density. The discovery opens up the vast space between the perfectly ordered spinel and the fully cation-disordered end member. To facilitate rational cathode design in this space, it is desirable to identify the chemical and structural variables that control the degree of order and understand their impact on performance.

In this study, we successfully synthesized the $Li_{1.4+x}Mn_{1.6}O_{3.7}F_{0.3}$ compositional series ($0.07 < x < 1$) using a mechanochemical method. These materials exhibit much higher capacity (> 350 mAh g^{-1}) and energy density (> 1,000 Wh kg^{-1}) than the prototype $LiMn_2O_4$ obtained under the same synthesis conditions. We find that the Li over-stoichiometry content x introduced during synthesis is a useful handle for tuning the degree of cation disorder. As x increases, the structure evolves from spinel-like cation order to almost complete cation disorder. Accordingly, the electrochemical voltage profile becomes more sloping in the 3 V region. The modified cation order also affects the Li transport kinetics and redox mechanism, which our computational analysis attributes to the modified short-range and long-range structural order.

4.2 Methodology

4.2.1 Experimental methodology

4.2.1.1 Synthesis

$LiMn_2O_4$, $Li_{1.47}Mn_{1.6}O_{3.7}F_{0.3}$, $Li_{1.68}Mn_{1.6}O_{3.7}F_{0.3}$, $Li_2Mn_{1.6}O_{3.7}F_{0.3}$ and $Li_{2.4}Mn_{1.6}O_{3.7}F_{0.3}$ were synthesized by high-energy ball-milling. For synthesizing $LiMn_2O_4$ and $Li_{2.4}Mn_{1.6}O_{3.7}F_{0.3}$, one gram of stoichiometric Li_2O, Mn_2O_3, MnO_2, and LiF were mixed into a 50-mL stainless-steel jar with five 10-mm and ten 5-mm stainless-steel balls. The jar was sealed with safety closure clamps in an Ar-filled glove box. After high-energy ball milling at rotational speed of 450 rpm for 10 hours (or 28h), using a Retsch PM200 planetary ball, the phase-pure $LiMn_2O_4$ (or $Li_{2.4}Mn_{1.6}O_{3.7}F_{0.3}$) was obtained. For $Li_{1.47}Mn_{1.6}O_{3.7}F_{0.3}$, $Li_{1.68}Mn_{1.6}O_{3.7}F_{0.3}$ and $Li_2Mn_{1.6}O_{3.7}F_{0.3}$, the precursor Li_2MnO_3 was first synthesized by a solid-state method (firing stoichiometric Li_2CO_3 and MnO_2 at 800 °C in air for 16 hours). Then, stoichiometric Li_2MnO_3, Mn_2O_3, MnO_2 and MnF_2 or MnF_3 were used as precursors. The rest procedure is the same as the previous one except for synthesis time, 21, 24 and 26 hours for $Li_{1.47}Mn_{1.6}O_{3.7}F_{0.3}$, $Li_{1.68}Mn_{1.6}O_{3.7}F_{0.3}$ and $Li_2Mn_{1.6}O_{3.7}F_{0.3}$.

4.2.1.2 Electrochemistry

All cathode films were fabricated in an Ar-filled glove box. 70 mg active material was first mixed with 20 mg Super C65 carbon black (Timcal) in a mortar by hand for 30 minutes. The components were then mixed with 10 mg polytetrafluoroethylene (Dupont) and rolled into a thin film to be used as a cathode. The cathode was cut by a 5/16 inches-diameter punch and the loading density of the cathode film was 3-4 mg cm^{-2}. To assemble the coin cells (CR2032), 0.1 mL of commercialized 1 M $LiPF_6$ in ethylene carbonate (EC) and dimethyl carbonate (DMC) solution (volume ratio 1:1, Sigma-Aldrich, battery grade) was used as electrolyte, glass microfibers (Whatman) were used as separators and FMC Li round metal foil (7/16 inches in diameter) was used as anode. The assembly process was also carried out in the Ar-filled glove box. After sealing the coin cells, they were rested for 6 hours before being tested on an Arbin battery cycler at room temperature. GITT measurements were performed by charging/discharging the cell for 1 hour at a current density of 10 mA g^{-1} followed by relaxing for 6 h to reach a quasi-equilibrium state.

4.2.1.3 Structure characterization

Synchrotron XRD patterns were measured at Beamline 11-BM of Advanced Photon Source. All the *ex-situ* samples were electrode powder composed of active materials and Super C65 in a weight ratio of 9:1. The loose powder mixture was cycled at 5 mA g^{-1}, followed by equilibrating at the designated voltage until the residual current was below 0.2 mA g^{-1}. The cycled powder was then washed with dimethyl carbonate and dried in vacuum. Neutron powder diffraction experiments were performed at the Spallation Neutron Source in Oak Ridge National Laboratory on the Nanoscale Ordered Materials Diffractometer. All the synchrotron and neutron data refinements were carried out using the TOPAS software package. SEM images were collected using a Zeiss Gemini Ultra-55 Analytical Field Emission SEM at the Molecular Foundry in Lawrence Berkeley National Lab (LBNL). The selected area electron diffraction (SEAD) and HRTEM were collected using a FEI Themis Z probe corrected transmission electron microscope with an accelerating voltage of 200 kV.

4.2.1.4 Operando Mn K-edge X-ray Absorption Spectroscopy.

Operando X-ray absorption spectroscopy (XAS) measurements at Mn K-edge were performed in a transition mode at Beamline 20-BM-B of the Advanced Photon Source, Argonne National Laboratory. A Si (111) monochromator was used for selecting the incident beam energy. A Rh-coated mirror was applied to get harmonic rejection. For the *operando* measurement, the modified *in-situ* cell was cycled within the voltage window of 1.5 - 4.8 V at a cycling rate of 30 mA g^{-1}. All electrode films were made in the same way as described in the electrochemistry section. The energy calibration was accomplished by simultaneously measuring the spectra of Mn metal foil. The cell was held at the top of charge or end of discharge for one hour to ensure a full scan. Normalization and calibration of raw data were carried out by Athena software.[129]

4.2.1.5 Mapping of resonant inelastic x-ray scattering

mRIXS of O *K*-edge and Mn *L*-edge was measured in the iRIXS endstation at Beamline 8.0.1 of Advanced Light Source [130], Lawrence Berkeley National Laboratory. The beam spot size is about 25*100 mm^2. Mapping data were collected by the ultrahigh efficiency modular spectrometer [131], with an excitation energy step of 0.2 eV. The resolution of the excitation energy is 0.35 eV, and that of the emission energy is 0.25 eV. All *ex-situ* samples were electrode films, composed of active materials, carbon black and PTFE in a weight ratio of 70:20:10. The electrode films were charged or discharged to a certain state of charge in a coin cell at 50 mA g^{-1} and held at that voltage for 6 hours. The cells were disassembled, and the films were washed with DEC in an Ar-filled glovebox. Final 2D maps were achieved via a multistep data processing including normalization to beam flux and collecting time, integration and combination, etc., which has been elaborated on in previous work.[59] Mn-*L* iPFY was achieved through the formula iPFY = a /PFY_O, where a is a normalization coefficient, PFY_O was extracted by integrating the fluorescence intensity within the O-*K* emission energy range (495 to 510 eV) on the Mn-*L* mRIXS (dotted rectangle in Fig. 2B). Quantitative fitting of Mn-L iPFY was performed via linear combination with the standard experimental spectra of $Mn^{2+/3+/4+}$, as demonstrated and detailed before.[132]

4.2.1.6 Solid-State Nuclear Magnetic Resonance Spectroscopy (ssNMR)

^{19}F and ^{7}Li ssNMR data were collected on the $Li_{1.47}Mn_{1.6}O_{3.7}F_{0.3}$ and $Li_2Mn_{1.6}O_{3.7}F_{0.3}$ pristine powders using a Bruker Avance 300 MHz (7.05 T) super wide-bore NMR spectrometer with Larmor frequencies of 282.40 MHz and 116.64 MHz, respectively, at room temperature. The data were obtained at 30 kHz magic-angle spinning (MAS) using a 2.5 mm double-resonance HX probe. ^{19}F and ^{7}Li NMR data were referenced against 1M aqueous solutions of sodium fluoride (NaF, $\delta(^{19}F) = -118$ ppm) and lithium chloride (LiCl, $\delta(^{7}Li) = 0$ ppm) and these samples were also used for pulse calibration. Lineshape analysis was carried out within the Bruker Topspin software using the SOLA lineshape simulation package.

The resonant frequency range of ^{19}F nuclei in $Li_{1.47}Mn_{1.6}O_{3.7}F_{0.3}$ and $Li_2Mn_{1.6}O_{3.7}F_{0.3}$ was larger than the excitation bandwidth of the RF pulse used in the NMR experiment. To obtain the full spectrum, ten spin echo sub-spectra were collected for each sample. These were obtained by varying the carrier frequency in steps of 300 ppm (84.73 kHz) from −1500 to 1200 ppm, where the step size was slightly less than the excitation bandwidth of the RF pulse. Individual sub-spectra were processed using a zero-order phase correction and then added to give an overall sum spectrum in absorption mode that required no further phase correction. This method – termed 'spin echo mapping' [70], 'frequency stepping' [68,69], or 'VOCS' (Variable Offset Cumulative Spectrum) [71] – is able to uniformly excite the broad ^{19}F signals by providing a large excitation bandwidth. Individual ^{19}F spin echo spectra were collected using a 90° RF pulse of 1.95 μs and a 180° RF pulse of 3.9 μs at 190 W, with a recycle delay of 60 ms. Additionally, a ^{19}F spin echo spectrum of LiF was obtained using similar RF pulses for comparison with spectra collected on the partially-(dis)ordered spinel samples using a recycle delay of 5 s at 30 kHz MAS.

^{7}Li spin echo spectra were acquired on all samples using a 90° radiofrequency (RF) pulse of 0.43 μs and a 180° RF pulse of 0.86 μs at 300 W. A recycle delay of 80 ms was used for the partially-(dis)ordered spinel samples. ^{7}Li pj-MATPASS (projected Magic-Angle Turning Phase-Adjusted Sideband Separation) [133] isotropic spectra were also acquired on all samples using a 90° RF pulse of 0.43 μs at 100 W, with a recycle delay of 50 ms.

4.2.1.7 Differential Electrochemical Mass Spectrometry (DEMS)

Outgassing of $Li_{1.47}Mn_{1.6}O_{3.7}F_{0.3}$ and $Li_2Mn_{1.6}O_{3.7}F_{0.3}$ cathodes during the first cycle of galvanostatic charge of discharge was monitored on a custom-built DEMS system, which was operated as described in a previous study.[134] Modified Swagelok-type cells were prepared in an Ar-filled glove box. The composition of cathodes and anodes were identical to those used for the coin cell tests in this study. For each DEMS cell, one sheet of Celgard 2500 (polypropylene) and one sheet of QM-A quartz microfiber filters (Whatman) were used as separators with 80 μL of 1 M $LiPF_6$ (Gotion) in EC/DEC (BASF, 1:1 v/v) added as the electrolyte. DEMS cells were cycled at a constant current rate of 0.1 Li^+ h^{-1} (16.44 mA g^{-1} for $Li_{1.47}Mn_{1.6}O_{3.7}F_{0.3}$ and 16.08 mA g^{-1} for $Li_2Mn_{1.6}O_{3.7}F_{0.3}$) under a static head of argon pressure (approximately 1.2 bar) at room temperature. Accumulated gas in the cell was purged by 500 μL of pulsed Ar gas every 10 minutes. Swept-out gas was sent to a holding chamber, where it was subsequently leaked to a mass-spectrometry chamber for analysis. The setup is calibrated for O_2 and CO_2 in the carrier gas Ar.

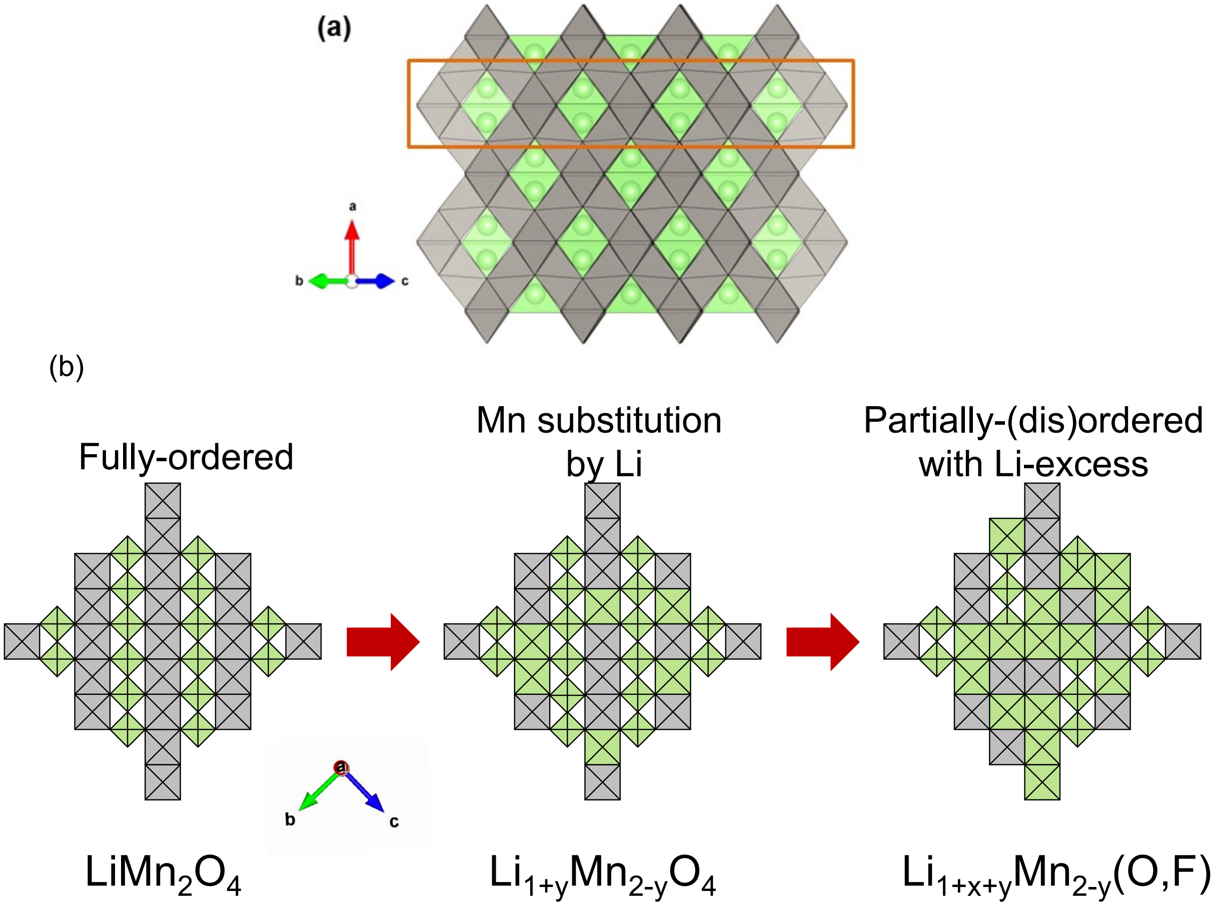

Figure 4-1. Design of partially-(dis)ordered spinel cathodes with Li over-stoichiometry *x* and Mn substitution by Li *y*. (a) Structure of fully-ordered $LiMn_2O_4$ (grey octahedra = MnO_6, green tetrahedra = LiO_4, green spheres = Li ions). The atomic slab outlined by the orange square is viewed from above and depicted in detail in (b) as fully ordered (left), with some Mn substituted by Li (middle), and with partial disorder and Li over-stoichiometry. The bold green squares represent face sharing Li_{tet}-Li_{oct}.

4.3 Results

4.3.1 Design, synthesis and structural characterizations

To obtain spinel-type cathodes with a large practical capacity, we follow the design rules depicted in **Figure 4-1**. A fully ordered spinel has well-percolating Li diffusion channels (**Figure 4-1a** and **4-1b**(left)) but suffers from a kinetically-slow and structurally destructive two-phase reaction associated with the collective Li 8a-to-16c transition when $LiMn_2O_4$ is lithiated to $Li_2Mn_2O_4$. A three-pronged strategies is employed to suppress or reduce the two-phase region, represented by a general stoichiometry of $Li_{1+x+y}Mn_{2-y}(O,F)_4$: 1) Substitution of some Mn on the 16d site to facilitate Mn/Li disorder and facilitate the incorporation of excess Li; 2) Introduction of extra Li ($x > 0$) to occupy some of the previously empty 16c sites and create some face sharing Li_{tet}-Li_{oct} which are believed to create fast Li-ion transport pathways in spinel-like materials [135]; 3) Creation of Mn disorder among the 16c/16d sites by ball milling to reduce the spinel-like order. We selected a 20% Li substitution on 16d site ($y = 0.4$ in $Li_{1+x+y}Mn_{2-y}(O,F)_4$) based on previous percolation analysis and focus on the tuning of x in this study.

Three partially-(dis)ordered spinels $Li_{1.47}Mn_{1.6}O_{3.7}F_{0.3}$ (0.07 excess cations per spinel formula unit) , $Li_{1.68}Mn_{1.6}O_{3.7}F_{0.3}$ (0.28 excess cations) and $Li_2Mn_{1.6}O_{3.7}F_{0.3}$ (0.6 excess cations) were synthesized by a mechanochemical ball-milling method. Fluorination was used to charge-compensate the Li substitution, increase the TM capacity by lowering the Mn valence, and improve cyclability.[19,41,136] Synchrotron X-ray diffraction (SXRD) patterns in **Figure 4-2a** indicate that the three compounds can be indexed to a single-phase spinel structure with various degrees of cation disorder. After normalizing the intensity of each SXRD pattern by that of the corresponding (400) peak, we observe a weakening (111) diffraction peak at a *d* spacing between 4 and 5 Å as the Li over-stoichiometry x increases from 0.07 to 0.6. This result, according to Rietveld refinement, indicates that Li over-stoichiometry creates Mn disorder between the 16c and 16d sites. To obtain the Li occupancies, neutron diffraction (ND), which is sensitive to light elements, was conducted. The Mn site occupancies are obtained from refinement of the SXRD pattern (**Table 4-3 – 4-5**) and fixed when refining the ND data **Figure 4-2b, 4-3, 4-4 and 4.5**. The final cation occupancies in the 8a, 16c and 16d sites are summarized in **Table 1**. Other refinement details can be found in **Tables 4-2 – 4-5**. This combined neutron/synchrotron XRD indicates that as the Li over-stoichiometry is increased the structure evolves from being mostly spinel-like-ordered, towards a hybrid spinel-rocksalt type of disorder with more cations on the octahedral site. All evidence indicates that this is a single-phase structure and not a composite of a spinel and rocksalt structure.

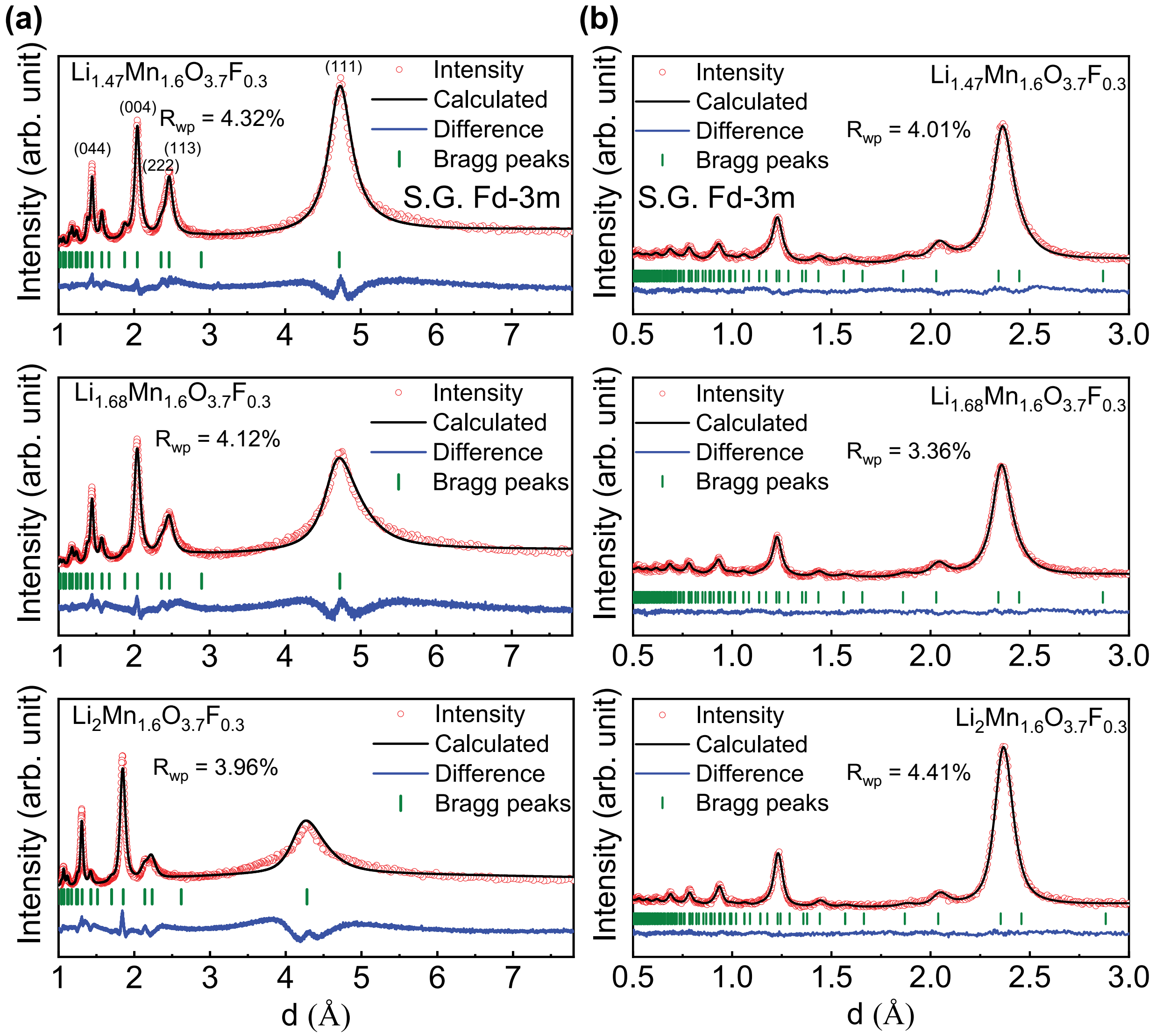

Figure 4-2. Refinement of three partially-(dis)ordered spinels. Rietveld refinement of the crystal structure using (a) synchrotron X-ray diffraction data ($\lambda = 0.4579$ Å) and (b) time-of-flight neutron diffraction data, of $Li_{1.47}Mn_{1.6}O_{3.7}F_{0.3}$, $Li_{1.68}Mn_{1.6}O_{3.7}F_{0.3}$ and $Li_2Mn_{1.6}O_{3.7}F_{0.3}$.

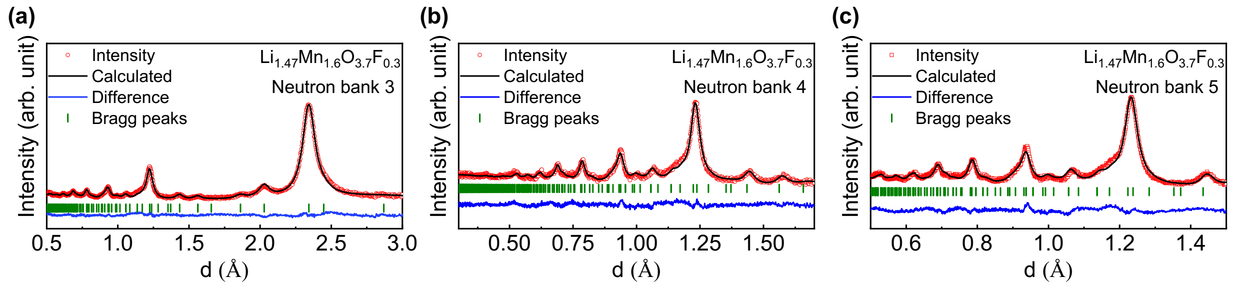

Figure 4-3. Rietveld refinement of crystal structure for $Li_{1.47}Mn_{1.6}O_{3.7}F_{0.3}$, ($2\theta$ = 67° (a), 122° (b), 154° (c)) using time-of-flight neutron diffraction data at room temperature, with experimental data shown in red dots, calculated pattern in black line, difference curve in blue line and Bragg position in olive vertical bars.

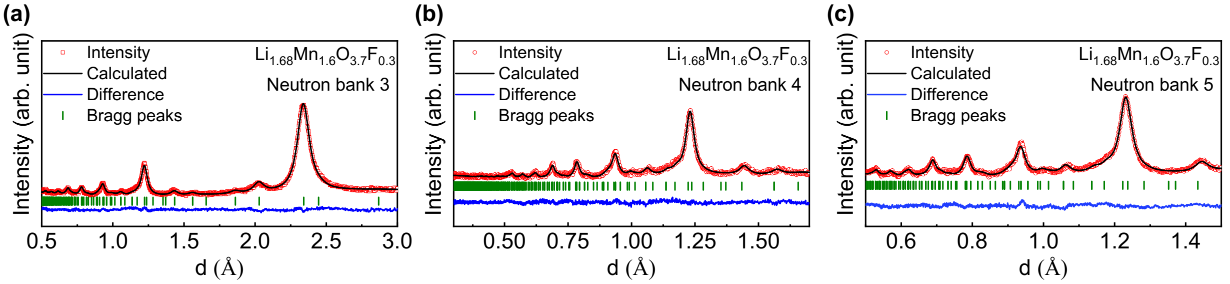

Figure 4-4. Rietveld refinement of crystal structure for $Li_{1.68}Mn_{1.6}O_{3.7}F_{0.3}$, ($2\theta = 67^{\circ}$ (a), 122° (b), 154° (c)) using time-of-flight neutron diffraction data at room temperature, with experimental data shown in red dots, calculated pattern in black line, difference curve in blue line and Bragg position in olive vertical bars.

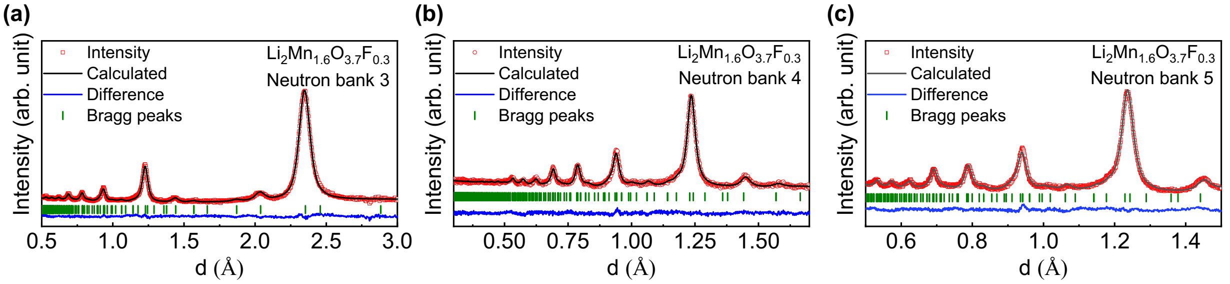

Figure 4-5. Rietveld refinement of crystal structure for $Li_2Mn_{1.6}O_{3.7}F_{0.3}$, ($2\theta = 67^{\circ}$ (a), 122° (b), 154° (c)) using time-of-flight neutron diffraction data at room temperature, with experimental data shown in red dots, calculated pattern in black line, difference curve in blue line and Bragg position in olive vertical bars.

Table 4-1. Structural information based on synchrotron and neutron powder diffraction refinement.

Atom	Wyckoff symbol	*x*	*y*	*z*	B_{iso}	$Li_{1.47}Mn_{1.6}O_{3.7}F_{0.3}$ occupancy	$Li_{1.68}Mn_{1.6}O_{3.7}F_{0.3}$ occupancy	$Li_2Mn_{1.6}O_{3.7}F_{0.3}$ occupancy
Li1	8a	0.125	0.125	0.125	0.80(2)	0.65(5)	0.57(5)	0.18(6)
Li2	16d	0.5	0.5	0.5	0.80(2)	0.10(2)	0.25(2)	0.44(2)
Li3	16c	0	0	0	0.80(2)	0.31(2)	0.31(2)	0.47(2)
Mn1	16d	0.5	0.5	0.5	0.83(9)	0.74(2)	0.67(5)	0.56(2)
Mn2	16c	0	0	0	0.83(9)	0.06(2)	0.12(5)	0.24(2)
O1	32e	0.259(3)	0.259(3)	0.259(3)	0.66(3)	0.925	0.925	0.925
F1	32e	0.259(3)	0.259(3)	0.259(3)	0.66(3)	0.075	0.075	0.075

Table 4-2. Details about neutron powder diffraction refinement

Compounds	$Li_{1.47}Mn_{1.6}O_{3.7}F_{0.3}$	$Li_{1.68}Mn_{1.6}O_{3.7}F_{0.3}$	$Li_2Mn_{1.6}O_{3.7}F_{0.3}$
Space group	F*d*-3*m*	F*d*-3*m*	F*d*-3*m*
Temperature	300 K	300 K	300 K
Formula units/cell	8	8	8
Lattice parameter a (Å)	8.1179(0)	8.1136(0)	8.1526(0)
Cell volume ($Å^3$)	534.97(2)	534.12(2)	541.86(2)
R_{wp} (%)	4.01	3.63	4.41
GoF	1.16	1.13	1.42

Table 4-3. Extra structure parameter for $Li_{1.47}Mn_{1.6}O_{3.7}F_{0.3}$ from neutron powder diffraction refinement

Atom	Wyckoff symbol	x	y	z	B_{iso}	Occupancy
Li1	8a	0.125	0.125	0.125	0.80(2)	0.65(5)
Li2	16d	0.5	0.5	0.5	0.80(2)	0.10(2)
Li3	16c	0	0	0	0.80(2)	0.31(2)
Mn1	16d	0.5	0.5	0.5	0.83(9)	0.74(2)
Mn2	16c	0	0	0	0.83(9)	0.060(2)
O1	32e	0.26131	0.26131	0.26131	0.66(3)	0.925
F1	32e	0.26131	0.26131	0.26131	0.66(3)	0.075

Table 4-4. Extra structure parameter for $Li_{1.68}Mn_{1.6}O_{3.7}F_{0.3}$ from neutron powder diffraction refinement

Atom	Wyckoff symbol	x	y	z	B_{iso}	Occupancy
Li1	8a	0.125	0.125	0.125	0.80(2)	0.57(5)
Li2	16d	0.5	0.5	0.5	0.80(2)	0.25(2)
Li3	16c	0	0	0	0.80(2)	0.31(2)
Mn1	16d	0.5	0.5	0.5	0.83(9)	0.67(5)
Mn2	16c	0	0	0	0.83(9)	0.12(5)
O1	32e	0.26131	0.26131	0.26131	0.66(3)	0.925
F1	32e	0.26131	0.26131	0.26131	0.66(3)	0.075

Table 4-5. Extra structure parameter for $Li_2Mn_{1.6}O_{3.7}F_{0.3}$ from neutron powder diffraction refinement

Atom	Wyckoff symbol	x	y	z	B_{iso}	Occupancy
Li1	8a	0.125	0.125	0.125	0.80(2)	0.18(6)
Li2	16d	0.5	0.5	0.5	0.80(2)	0.44(2)
Li3	16c	0	0	0	0.80(2)	0.47(2)
Mn1	16d	0.5	0.5	0.5	0.83(9)	0.56(2)
Mn2	16c	0	0	0	0.83(9)	0.24(2)
O1	32e	0.26131	0.26131	0.26131	0.66(3)	0.925
F1	32e	0.26131	0.26131	0.26131	0.66(3)	0.075

Scanning electron microscopy (SEM) was applied to characterize the particle morphology. We do not include the characterization of $Li_{1.68}Mn_{1.6}O_{3.7}F_{0.3}$ as it was reported in previous work.[59] As shown in **Figure 4-6 a–b**, $Li_{1.47}Mn_{1.6}O_{3.7}F_{0.3}$ and $Li_2Mn_{1.6}O_{3.7}F_{0.3}$ have a primary particle size of 100–200 nm post mechanochemical synthesis, which is comparable to that in $Li_{1.68}Mn_{1.6}O_{3.7}F_{0.3}$.[59] In the lower-magnification SEM images, agglomeration of primary particles into secondary particles was observed (**Figure 4-7**). To verify the compositional homogeneity, scanning transmission electron microscopy (STEM) and energy dispersion spectroscopy (EDS) mapping were performed and the results are presented in Figure 3c–d. All the detectable elements, Mn, O, and F, are uniformly distributed in $Li_{1.47}Mn_{1.6}O_{3.7}F_{0.3}$ and $Li_2Mn_{1.6}O_{3.7}F_{0.3}$. To verify whether the structure is a single-phase partially-(dis)ordered spinel, high-resolution transmission electron microscopy (HRTEM) and electron diffraction (ED) were performed. The characteristic *d* spacing of ~ 4.8 Å, which corresponds to the spinel (111) planes, is marked by white lines in the HRTEM images (**Figure 3e, f**). The ED patterns of both $Li_{1.47}Mn_{1.6}O_{3.7}F_{0.3}$ and $Li_2Mn_{1.6}O_{3.7}F_{0.3}$ can be indexed to a spinel crystal structure.

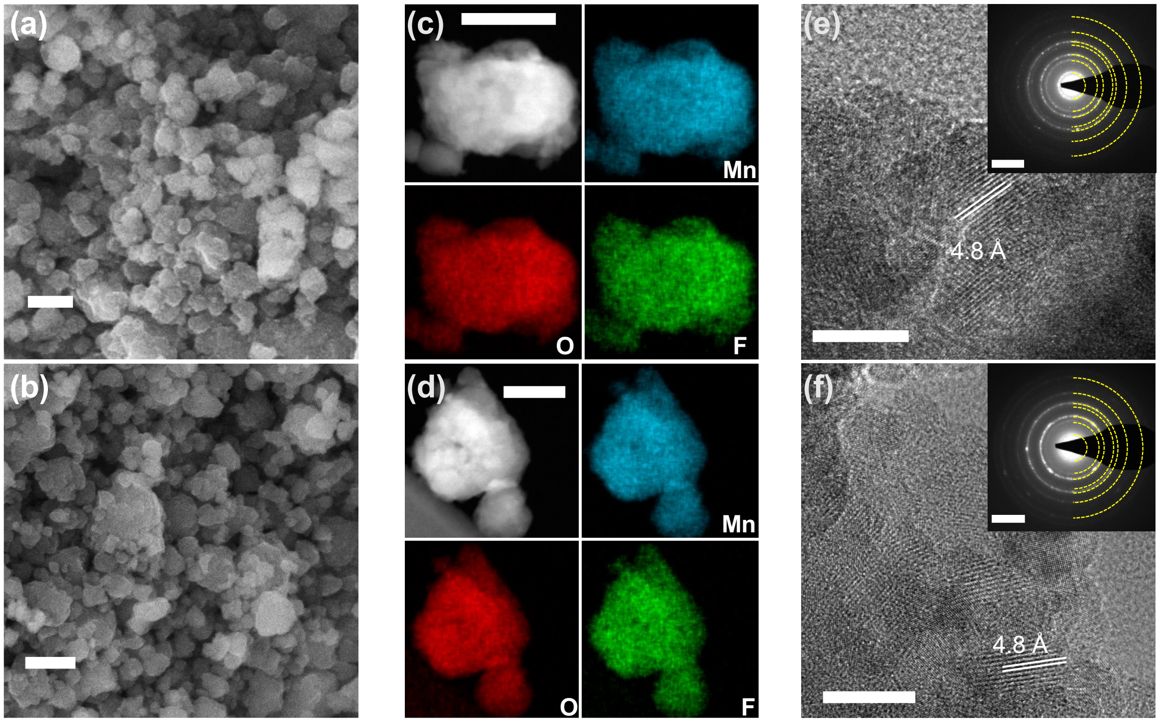

Figure 4-6. SEM, STEM/EDS and HRTEM/ED of two partially-(dis)ordered spinel compounds. SEM images of the as-synthesized (a) $Li_{1.47}Mn_{1.6}O_{3.7}F_{0.3}$ and (b) $Li_2Mn_{1.6}O_{3.7}F_{0.3}$ (scale bars, 200 nm). STEM images and EDS mapping of the elements Mn, O and F (c) $Li_{1.47}Mn_{1.6}O_{3.7}F_{0.3}$ and (d) $Li_2Mn_{1.6}O_{3.7}F_{0.3}$ (scale bars, 30 nm). HRTEM images of (e) $Li_{1.47}Mn_{1.6}O_{3.7}F_{0.3}$ and (f) $Li_2Mn_{1.6}O_{3.7}F_{0.3}$ (scale bars, 10 nm). Insets: ED patterns (scale bars, 5 nm^{-1}). The selected area electron diffraction patterns can be indexed to a spinel lattice, with the *d* spacings measured to be 4.8, 2.5, 2.1, 1.6, 1.5, 1.2 and 1.0 Å.

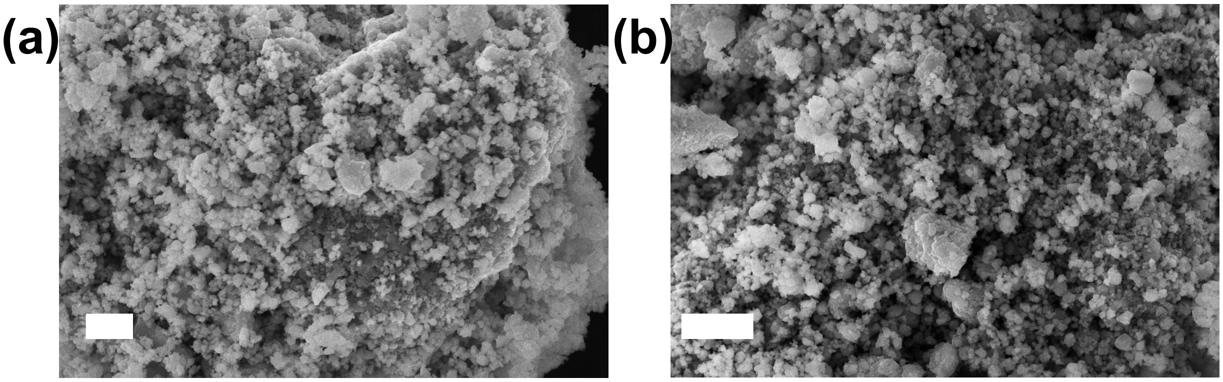

Figure 4-7. Scanning electron microscope (SEM) images of (a) $Li_{1.47}Mn_{1.6}O_{3.7}F_{0.3}$ and (b) $Li_2Mn_{1.6}O_{3.7}F_{0.3}$ which shows the agglomeration of primary particles into secondary particles (scale bars, 1 μm).

^{19}F and ^{7}Li solid-state nuclear magnetic resonance (ssNMR) measurements were conducted to further verify the integration of F in the bulk structure (**Figure 4-8**). The spectra obtained on the $Li_{1.47}Mn_{1.6}O_{3.7}F_{0.3}$ and $Li_2Mn_{1.6}O_{3.7}F_{0.3}$ pristine powders show two distinct components: a broad, paramagnetic signal and a sharp, diamagnetic signal. The broad signal corresponds to ^{19}F nuclei in the bulk of the cathode materials. Their interaction with nearby paramagnetic Mn ions leads to a shift of the ^{19}F resonant frequency away from that of diamagnetic LiF at −204 ppm and to significant spectral broadening. Additionally, for both compounds, the observed paramagnetic lineshape comprises several broad and overlapping ^{19}F signals assigned to a wide variety of ^{19}F local environments in the partially-(dis)ordered spinel lattice. The sharp signal centered at −204 ppm is assigned to a diamagnetic LiF impurity phase present in small amounts in these two samples. We note that NMR signals from ^{19}F nuclei directly bonded to paramagnetic Mn species in the bulk cathode materials are too broad (and short-lived) to be observed experimentally, which prevents the exact quantification of the LiF impurity phase in these samples. If anything, the amount of LiF impurity phase obtained from ^{19}F NMR data is overestimated, indicating that the majority of F ions are incorporated into the bulk of the partially disordered spinel compounds.

The integration on quantitative ^{7}Li spin echo spectra was performed to further characterize the Li local environments. By integrating the sharp signal close to 0 ppm in each spectra the fraction of Li present in diamagnetic environments (*e.g.* in Li_2CO_3, Li_2O, or LiF) was found to be 2% and 1% (+/− 1%) for $Li_{1.47}Mn_{1.6}O_{3.7}F_{0.3}$ and $Li_2Mn_{1.6}O_{3.7}F_{0.3}$, respectively. This intensity provides the upper limit for the amount of impurity phases present in the samples, as the signal could also arise from the formation of large diamagnetic Li-rich (Mn-poor) domains within the disordered oxide matrix.[60] Overall, the fraction of diamagnetic ^{7}Li environments in these disordered spinel samples is no more than 3% of the total Li content, we conclude that there is excellent F solubility in the $Li_{1.47}Mn_{1.6}O_{3.7}F_{0.3}$ and $Li_2Mn_{1.6}O_{3.7}F_{0.3}$ spinel compositions.

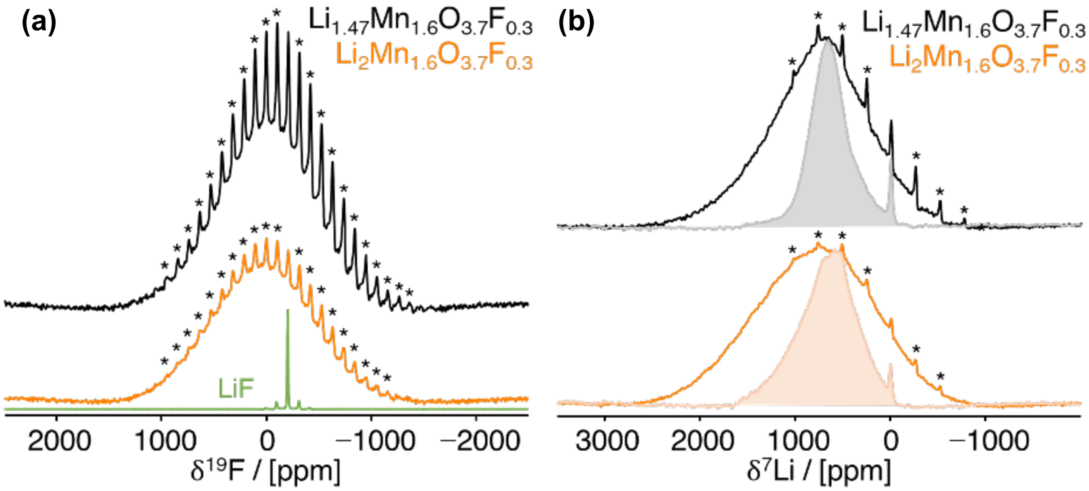

Figure 4-8. ssNMR spectra obtained on the as-synthesized partially-(dis)ordered spinel materials. (a) ^{19}F ssNMR spectra obtained by summing multiple spin echo sub-spectra acquired at different excitation frequencies to ensure homogeneous excitation of the broad lineshape. For comparison, a ^{19}F spectrum collected on LiF powder is overlaid. (b) ^{7}Li spin echo (line) and pj-MATPASS (shaded, for clarity) ssNMR spectra of the as-synthesized materials. All spectra are scaled according to the moles of Li in the rotor and number of scans. The asterisks indicate the spinning sidebands.

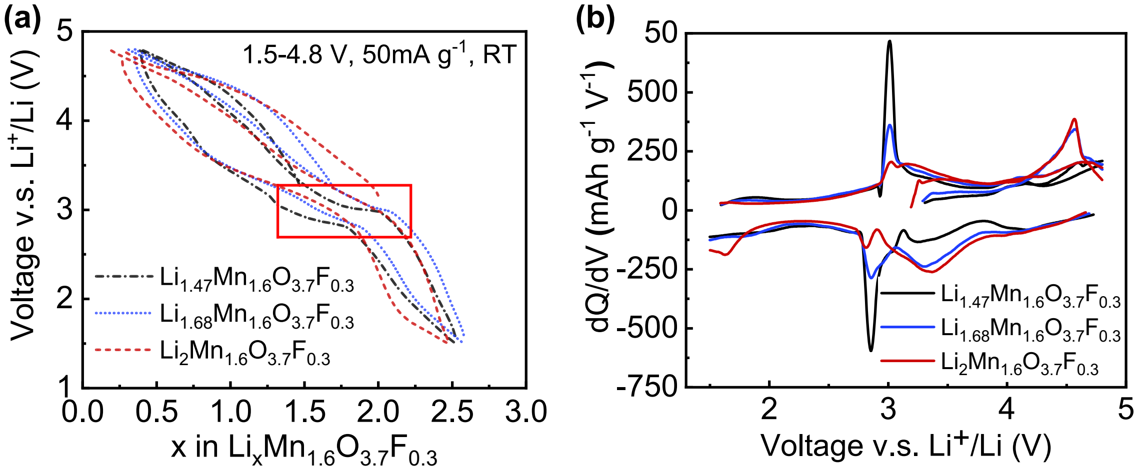

Figure 4-9. Galvanostatic charge and discharge performance. (a) voltage profile during first cycle and the second charge of $Li_{1.47}Mn_{1.6}O_{3.7}F_{0.3}$ (black dash dot), $Li_{1.68}Mn_{1.6}O_{3.7}F_{0.3}$ (blue dot) and $Li_2Mn_{1.6}O_{3.7}F_{0.3}$ (red dash). (b) Corresponding dQ/dV curves when cycled between 1.5 and 4.8 V at 50 mA g^{-1}.

4.3.1 Voltage profiles modified by structural order

The three partially (dis)ordered spinels $Li_{1.4+x}Mn_{1.6}O_{3.7}F_{0.3}$ (x = 0.07, 0.28, and 0.6) exhibit distinct voltage profiles. As shown in **Figure 4-9a**, both the small voltage step near 4 V and the plateau-like feature near 3 V gradually disappear as x increases from 0.07 to 0.6, leading to a smoother and more sloping profile. Such variation is better captured by the dQ/dV curves shown in **Figure 4-9b**. In a perfectly-ordered $LiMn_2O_4$ spinel, the 3 V plateau upon lithiation is associated with the collective 8a-to-16c O transition resulting in a two-phase reaction between a cubic phase and a tetragonal phase.[54] Our voltage curves show no true plateau region anymore in $Li_{1.47}Mn_{1.6}O_{3.7}F_{0.3}$ and the pseudo plateau near 3 V is significantly narrower than that in ordered spinel, suggesting suppression of the two-phase reaction. As more cation disorder is introduced with the $Li_2Mn_{1.6}O_{3.7}F_{0.3}$ composition, the pseudo plateau disappears. Instead, more Li is extracted or inserted between 3.1 and 3.7 V. As a result, the average voltage as calculated from the first discharge process slightly increases from 2.99 V for $x = 0.07$ to 3.08 V for $x = 0.6$. There is no discernible voltage plateau near 4 V, likely due to the partial occupancy of the octahedral 16c sites, which reduces the tetrahedral Li occupation in the face-sharing 8a sites.

The room-temperature galvanostatic cycling performance is shown in **Figure 4-10a–c**. In the three cathode materials, the amount of available Li capacity is the same, which equals 2.4 Li per f.u. between the two limiting compositions of $Mn_{1.6}O_{3.7}F_{0.3}$ and $Li_{2.4}Mn_{1.6}O_{3.7}F_{0.3}$. Therefore, when cycled in a wide voltage range between 1.5 and 4.8 V, all three cathode materials exhibit comparably high gravimetric capacity > 350 mAh g^{-1} and energy density > 1,000 Wh kg^{-1}. But more capacity and energy is delivered at high voltages for the materials with a higher initial Li over-stoichiometry level. $Li_2Mn_{1.6}O_{3.7}F_{0.3}$ delivers a capacity of 226 mAh g^{-1} (813 Wh kg^{-1}) above 3 V, which decreases to 201 mAh g^{-1} (726 Wh kg^{-1}) for $Li_{1.68}Mn_{1.6}O_{3.7}F_{0.3}$ and 163 mAh g^{-1} (598 Wh kg^{-1}) for $Li_{1.47}Mn_{1.6}O_{3.7}F_{0.3}$. To measure the long-term stability, the three cathode materials were cycled at 50 mA g^{-1} in the 1.5–4.8 V (red squares) and 2.0–4.4 V (blue circles) ranges for 30 continuous cycles. The results are shown in **Figure 4-10d–f**. $Li_{1.47}Mn_{1.6}O_{3.7}F_{0.3}$ shows better capacity retention than the more Li-over-stoichiometric $Li_{1.68}Mn_{1.6}O_{3.7}F_{0.3}$ and $Li_2Mn_{1.6}O_{3.7}F_{0.3}$, in the 1.5–4.8 V range. To characterize any irreversible oxygen release and its relations to capacity loss, differential electrochemical mass spectrometry (DEMS) was performed on two representative compositions, $Li_{1.47}Mn_{1.6}O_{3.7}F_{0.3}$ and $Li_2Mn_{1.6}O_{3.7}F_{0.3}$ (**Figure 4-11**). Both compounds showed minimal oxygen loss with $Li_2Mn_{1.6}O_{3.7}F_{0.3}$ showing the higher oxygen loss. The results correlate with the observation of slightly less capacity retention between 1.5-4.8V for the more cation-disordered $Li_2Mn_{1.6}O_{3.7}F_{0.3}$ than for the more ordered $Li_{1.47}Mn_{1.6}O_{3.7}F_{0.3}$, indicating that unstable oxygen redox and oxygen loss at high voltage might be one origin of the capacity degradation. In a narrower voltage window of 2.0–4.4 V, $Li_{1.47}Mn_{1.6}O_{3.7}F_{0.3}$, $Li_{1.68}Mn_{1.6}O_{3.7}F_{0.3}$ and $Li_2Mn_{1.6}O_{3.7}F_{0.3}$ show enhanced capacity retention of 90.7%, 88.7% and 93.8%, respectively, after 30 cycles, with an initial capacity of ~200 mAh g^{-1}.

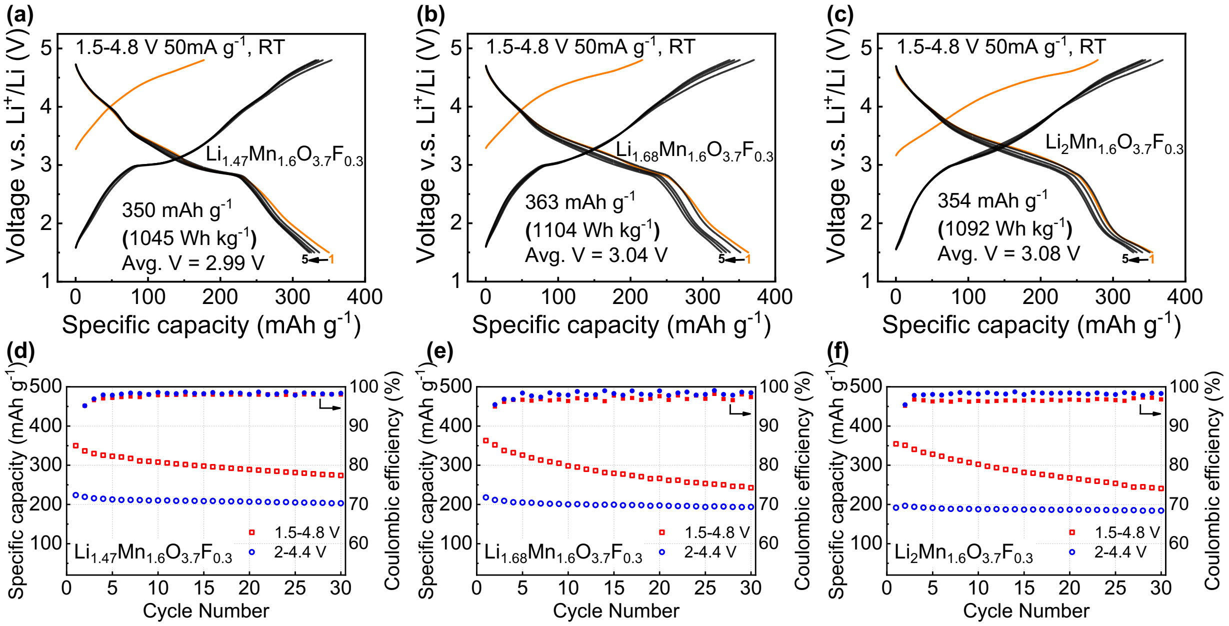

Figure 4-10. Galvanostatic cycling performance. Voltage profiles during the first 5 cycles of (a) $Li_{1.47}Mn_{1.6}O_{3.7}F_{0.3}$, (b) $Li_{1.68}Mn_{1.6}O_{3.7}F_{0.3}$, and (c) $Li_2Mn_{1.6}O_{3.7}F_{0.3}$. The initial discharge capacity, energy density and average discharge voltage are denoted in each figure. Capacity retention and Coulombic efficiency over 30 cycles of (d) $Li_{1.47}Mn_{1.6}O_{3.7}F_{0.3}$, (e) $Li_{1.68}Mn_{1.6}O_{3.7}F_{0.3}$, and (f) $Li_2Mn_{1.6}O_{3.7}F_{0.3}$, in two voltage ranges, 1.5 – 4.8V (red open squares) and 2 – 4.4 V (blue open circles).

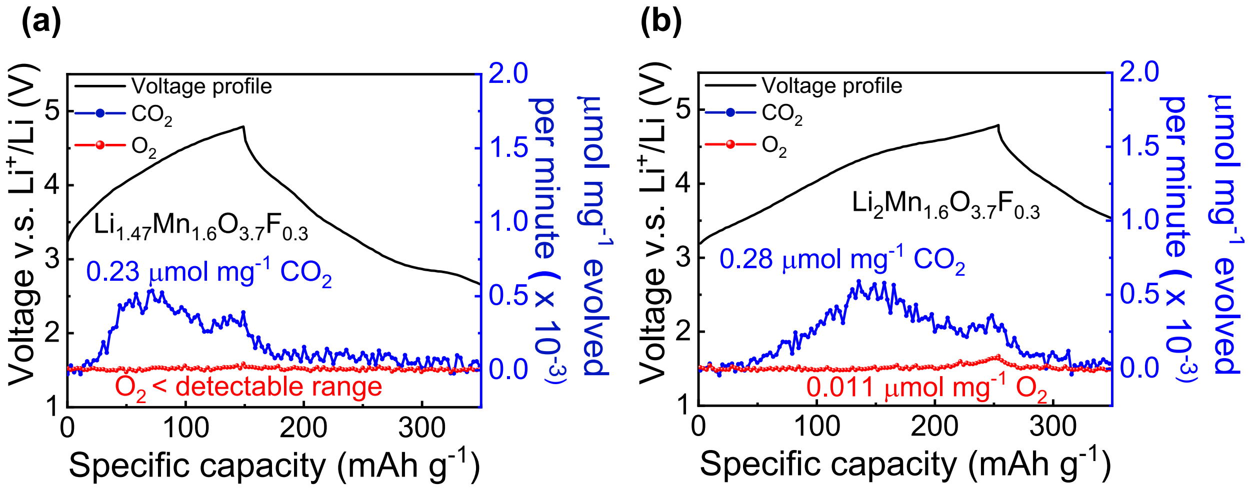

Figure 4-11. Operando DEMS results for (a) $Li_{1.47}Mn_{1.6}O_{3.7}F_{0.3}$ and (b) $Li_2Mn_{1.6}O_{3.7}F_{0.3}$. Voltage profile, amount of O_2 and CO_2 evolved during the first cycle are shown in black solid lines, red dots and blue dots. The current density for galvanostatic cycling during the operando DEMS is 0.1 f.u. of Li^+ h^{-1} (i.e. 16.44 mA g^{-1} for $Li_{1.47}Mn_{1.6}O_{3.7}F_{0.3}$ and 16.08 mA g^{-1} for $Li_2Mn_{1.6}O_{3.7}F_{0.3}$).

4.3.2 Rate capability

Modifying the cation order is expected to directly alter the local atomic arrangement and the percolation of Li migration channels in the structure [34], which both dictate the Li transport properties. We therefore investigated the rate capability of the three spinel oxyfluorides with various degrees of cation disorder, at current densities from 100 to 7,500 mA g^{-1}. A baseline material $LiMn_2O_4$ and a completely cation-disordered rocksalt (also known as DRX) $Li_{2.4}Mn_{1.6}O_{3.7}F_{0.3}$, synthesized by the same mechanochemical method, are included for comparison. Similar Li-Mn-O-F DRXs have been extensively studied and reported before.[137] The XRD pattern of the as-synthesized $LiMn_2O_4$ can be indexed to a cubic spinel structure (**Figure 4-12a**). When cycled at a low current density of 50 mA g^{-1}, the voltage profile of the material exhibits the 3 V and 4 V plateaus characteristic of the octahedral and tetrahedral Li insertion/extraction in a classic $LiMn_2O_4$ spinel cathode (**Figure 4-12**). Each rate test was done on a fresh cell and the voltage profiles of the second cycles at the given rates are shown in Figure 7a. The rate performance of the series is compared in a Ragone plot in **Figure 4-13**.

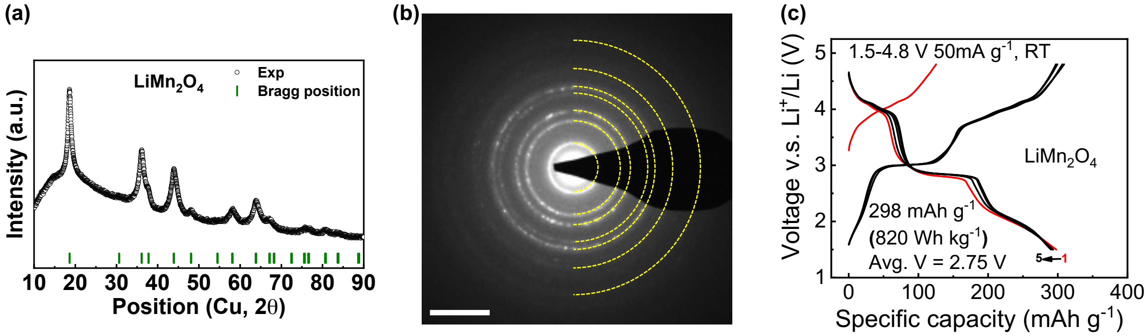

Figure 4-12. Structural and electrochemical characterization of mechanochemically synthesized $LiMn_2O_4$. (a) XRD pattern of the as-synthesized $LiMn_2O_4$, with peaks matching the expected Bragg positions for a cubic $LiMn_2O_4$ spinel. (b) Electron diffraction pattern of the as-synthesized $LiMn_2O_4$. Scale bar, 5/nm. The selected area electron diffraction patterns can be indexed to a spinel lattice, with the *d* spacings measured to be 4.8, 2.5, 2.1, 1.6, 1.5, 1.2 and 1.0 Å. (c) Voltage profiles during the first 5 cycles for $LiMn_2O_4$. The initial discharge capacity, energy density and average discharge voltage are denoted.

All four Li-Mn oxyfluorides with various initial Li over-stoichiometry show better rate capability than the baseline $LiMn_2O_4$. In $LiMn_2O_4$, a voltage plateau at ~2.8 V is observed at low rate, but this plateau shrinks at higher rates. Previously, ultrahigh rate capability was demonstrated in $Li_{1.68}Mn_{1.6}O_{3.7}F_{0.3}$ at up to 20 A g^{-1} using a high carbon loading of 50 wt%.[59] In this work, we kept a cathode formulation of 70:20:10 (wt%) active material, carbon black and Teflon. We found that while $Li_{1.68}Mn_{1.6}O_{3.7}F_{0.3}$ delivers the highest capacity at 100 mA g^{-1}, $Li_{1.47}Mn_{1.6}O_{3.7}O_{0.3}$ shows better rate capability by providing the highest capacity at 2,000 mA g^{-1}. $Li_{1.47}Mn_{1.6}O_{3.7}O_{0.3}$ retains a capacity of 158 mAh g^{-1} at 7,500 mA g^{-1}, corresponding to ~48% of the capacity at 100 mA g^{-1}. In addition, as the Li over-stoichiometry increases from 0.07 to 1.0 in the four Li-Mn oxyfluorides, a decrease in rate capability is observed.

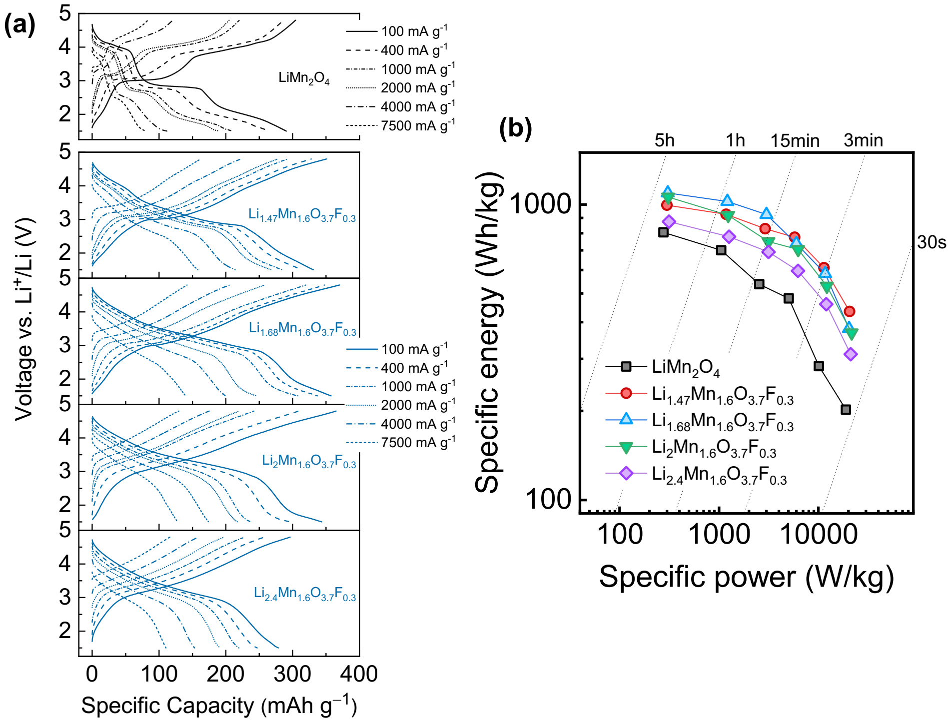

Figure 4-13. Rate capability measurements. (a) Galvanostatic voltage profiles of (top to bottom) LiMn$_2$O$_4$, Li$_{1.47}$Mn$_{1.6}$O$_{3.7}$F$_{0.3}$, Li$_{1.68}$Mn$_{1.6}$O$_{3.7}$F$_{0.3}$, Li$_2$Mn$_{1.6}$O$_{3.7}$F$_{0.3}$, and Li$_{2.4}$Mn$_{1.6}$O$_{3.7}$F$_{0.3}$ at various rates, from 100 to 7,500 mA g^{-1}. (b) Ragone plot comparing the specific energy and power. The loading density of the cathode films was 2-3 mg cm^{-2}, containing 70 wt% active materials, 20 wt% carbon black and 10 wt% Teflon.

4.3.2 Redox mechanism

The extraction or insertion of Li ions is accompanied by local charge compensation, the mechanism of which alters with variations in structural and chemical order. To probe the detailed redox mechanism, *in-situ* hard X-ray absorption spectroscopy (XAS) and *ex-situ* soft X-ray mappings of resonant inelastic X-ray scattering (mRIXS) measurements were carried out. We selected Li$_{1.47}$Mn$_{1.6}$O$_{3.7}$F$_{0.3}$ and Li$_2$Mn$_{1.6}$O$_{3.7}$F$_{0.3}$ as two representative compositions with a low and high Li over-stoichiometry level.

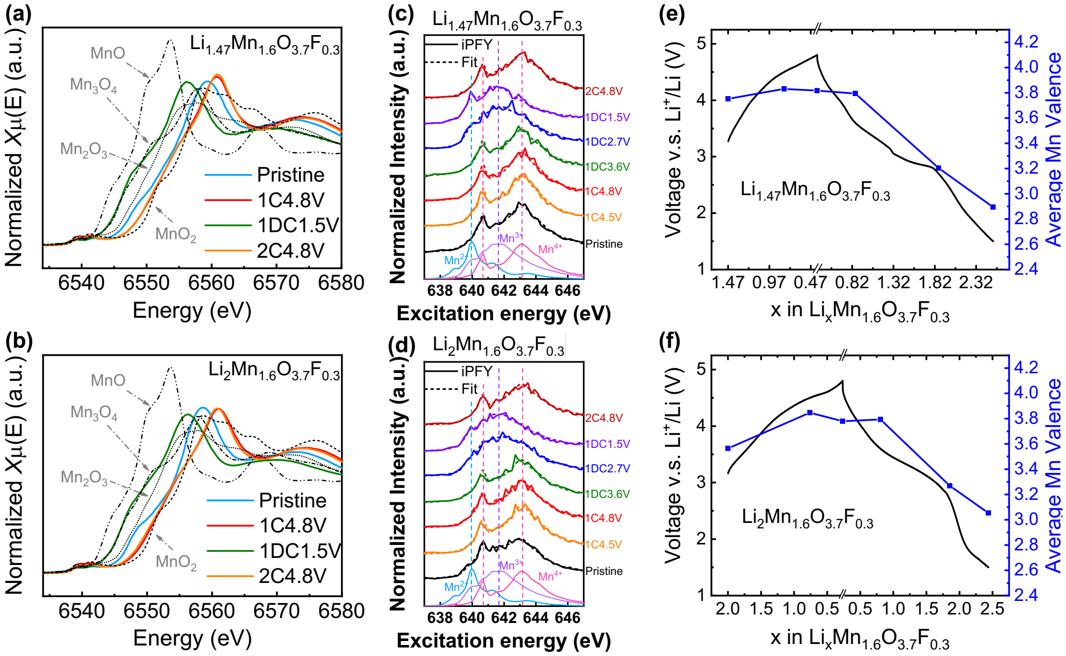

Figure 4-14. Redox mechanism of $Li_{1.47}Mn_{1.6}O_{3.7}F_{0.3}$ and $Li_2Mn_{1.6}O_{3.7}F_{0.3}$. Operando Mn K-edge X-ray absorption near edge spectra (XANES) of (a) $Li_{1.47}Mn_{1.6}O_{3.7}F_{0.3}$ and (b) $Li_2Mn_{1.6}O_{3.7}F_{0.3}$ during the first cycle and second charge. The blue, red, olive and orange curves represent the pristine, first charge to 4.8 V (1C4.8V), first discharge to 1.5 V (1DC1.5V) and second charge to 4.8 V (2C4.8V), respectively. *Ex-situ* Mn *L*$_3$-edge mRIXS-iPFY spectra of (c) $Li_{1.47}Mn_{1.6}O_{3.7}F_{0.3}$ and (d) $Li_2Mn_{1.6}O_{3.7}F_{0.3}$ at seven states of charge and discharge during the first and second cycle. Standard spectra of Mn^{2+}, Mn^{3+} and Mn^{4+} are included as references. The dash vertical lines highlight peak positions based on the standard spectra. Quantification of Mn valance (blue squares) based on mRIXS-iPFY overlaid on voltage profiles (black curves) during the first cycle in (e) $Li_{1.47}Mn_{1.6}O_{3.7}F_{0.3}$ and (f) $Li_2Mn_{1.6}O_{3.7}F_{0.3}$.

The X-ray absorption near-edge structure (XANES) is ideal for tracking the Mn valence change in operando because of its excellent bulk sensitivity and short data collection time. **Figure 4-14a–b** shows the Mn *K*-edge XANES spectra of $Li_{1.47}Mn_{1.6}O_{3.7}F_{0.3}$ and $Li_2Mn_{1.6}O_{3.7}F_{0.3}$ at selected states of charge during operando cycling. The complete operando spectra are shown in the **Figure 4-15 to 4-17**. By comparing their edge positions with those of the references (MnO, Mn_2O_3 and MnO_2), the Mn valence at various states of charge (SOC) can be estimated. In the pristine sample Mn is between 3+ and 4+ and is slightly higher in $Li_{1.47}Mn_{1.6}O_{3.7}F_{0.3}$ than in $Li_2Mn_{1.6}O_{3.7}F_{0.3}$. The observation agrees with our expectation of $Mn^{3.89+}$ in $Li_{1.47}Mn_{1.6}O_{3.7}F_{0.3}$ and $Mn^{3.56+}$ in $Li_2Mn_{1.6}O_{3.7}F_{0.3}$ deduced from the composition. During the first charge, Mn in both samples is oxidized to approximately Mn^{4+}, while upon discharge, the edge positions reverse to an energy between that in Mn_3O_4 and Mn_2O_3. During the second charge, the Mn *K*-edge reversibly shifts again to a position close to that of 4+, indicating a reversible Mn redox process. However, the main edge of XANES spectra cannot be used to precisely quantify the oxidation state because it measures dipole transitions from 1*s* to 4*p* orbitals, which do not involve the 3*d* valence states.

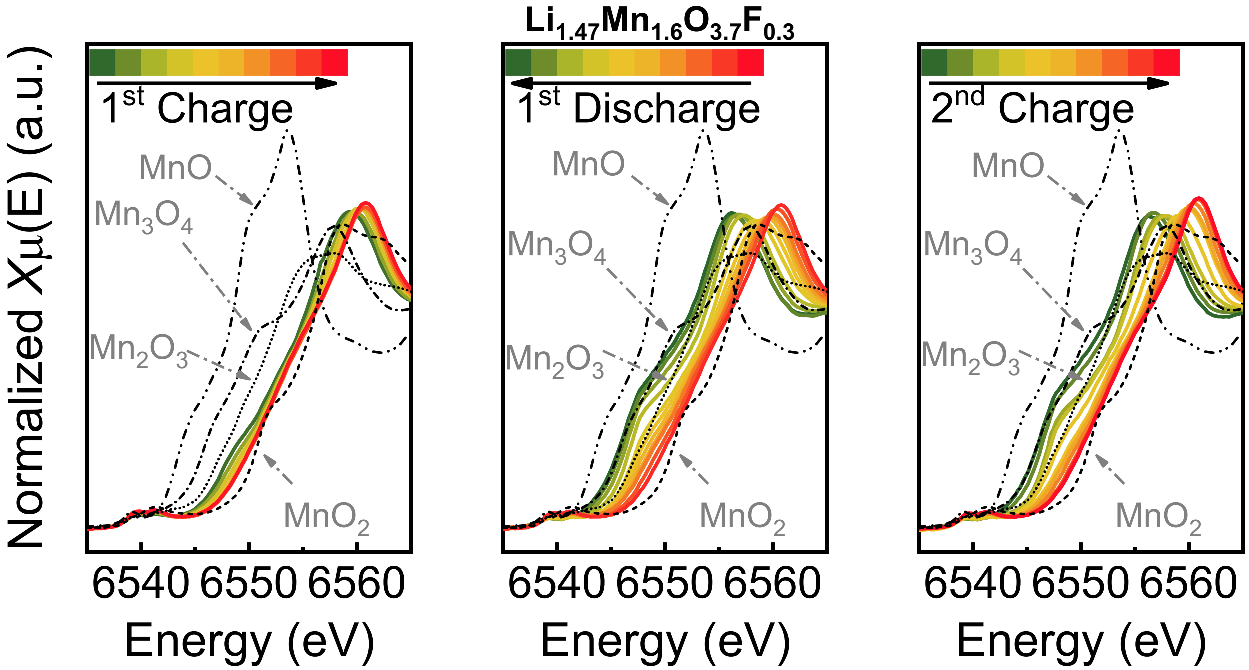

Figure 4-15. Operando X-ray absorption near edge spectroscopy of $Li_{1.47}Mn_{1.6}O_{3.7}F_{0.3}$. The spectra of MnO, Mn_3O_4, Mn_2O_3 and MnO_2 are included as references for Mn^{2+}, $Mn^{8/3+}$, Mn^{3+} and Mn^{4+}, respectively.

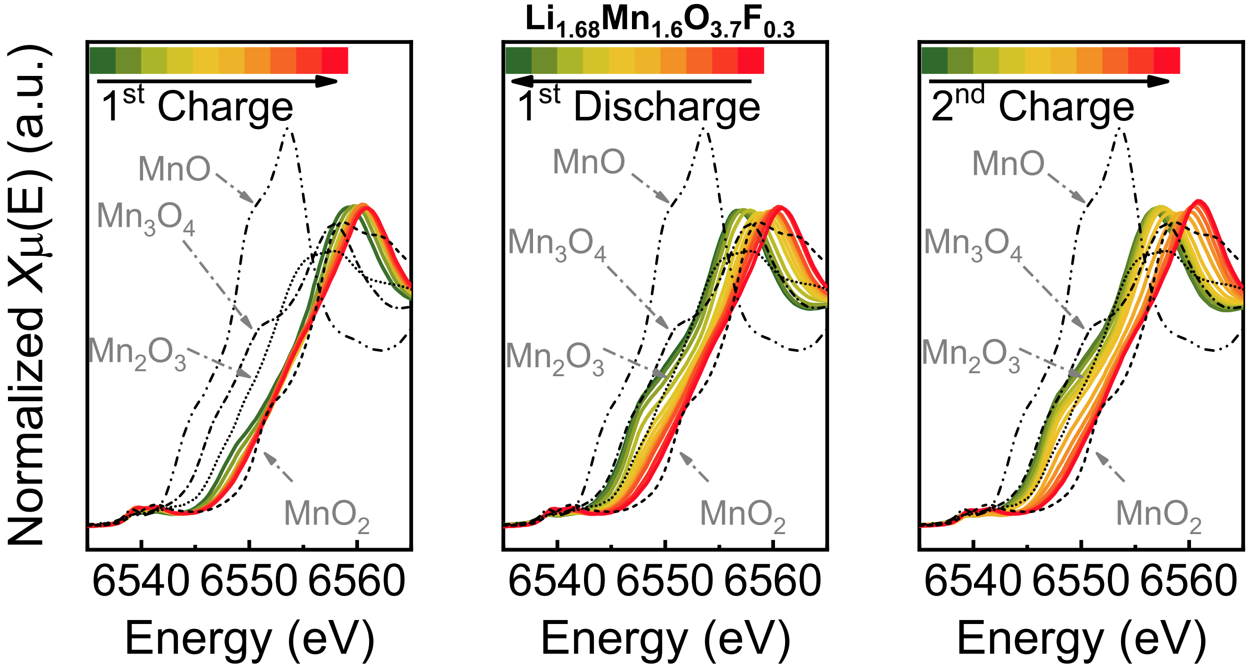

Figure 4-16. Operando X-ray absorption near edge spectroscopy of $Li_{1.68}Mn_{1.6}O_{3.7}F_{0.3}$. The spectra of MnO, Mn_3O_4, Mn_2O_3 and MnO_2 are included as references for Mn^{2+}, $Mn^{8/3+}$, Mn^{3+} and Mn^{4+}, respectively.

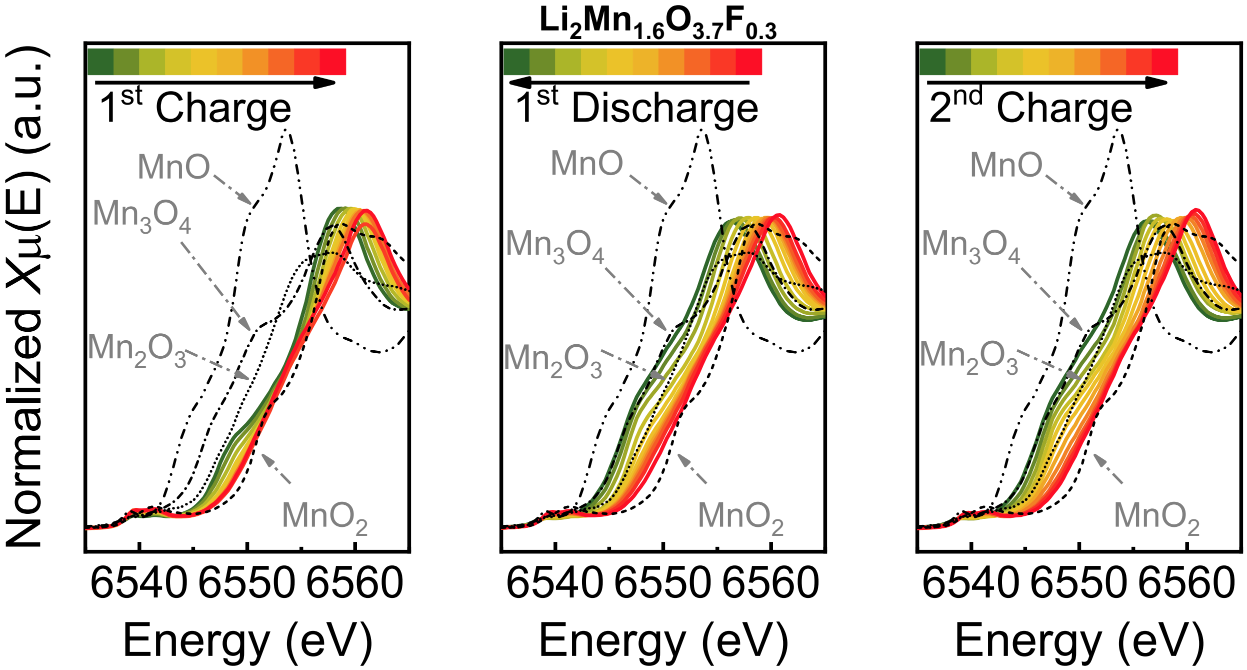

Figure 4-17. Operando X-ray absorption near edge spectroscopy of $Li_2Mn_{1.6}O_{3.7}F_{0.3}$. The spectra of MnO, Mn_3O_4, Mn_2O_3 and MnO_2 are included as references for Mn^{2+}, $Mn^{8/3+}$, Mn^{3+} and Mn^{4+}, respectively.

We also utilized *ex-situ* mRIXS at the Mn *L*-edge to quantify the evolution of Mn valences upon cycling. The technique directly probes the excitation from Mn 2*p* core states to 3*d* valence states. The Mn *L*-edge spectra can be obtained from the inverse partial fluorescence yield (iPFY) signal of the Mn RIXS map, which is a non-distorted bulk probe of the Mn 3*d* states.[130,138,139] The quantification was done by fitting the experimental L_3-edge as a linear combination of $Mn^{2+/3+/4+}$ reference spectra to generate the Mn valences (**Figure 4-14c-d**). The results are plotted in **Figure 4-14e–f** together with the electrochemical profile. The Mn valence in the pristine state is 3.75+ for $Li_{1.47}Mn_{1.6}O_{3.7}F_{0.3}$ and 3.56+ for $Li_2Mn_{1.6}O_{3.7}F_{0.3}$. Note that the actual pristine Mn states can be slightly lower than theoretical value due to the inert atmosphere used in synthesis, and the deviation is usually more significant for compounds with a higher Mn valence.[59] The Mn valence in the two materials increases to ~3.84+ when charged to 4.5 V and slightly dropped when further charged to 4.8 V, a phenomenon that has been previously observed and is associated with the complex interplay between O and TM oxidation processes at the top of charge.[140,141] At the beginning of discharge, the Mn valence remains constant until 3.6 V, suggesting the dominance of O reduction in this region. Once passed 3.6 V, the Mn valence decreases almost linearly and therefore the capacity in this region is contributed mainly by Mn reduction. At the bottom of discharge, the Mn valence is determined to be 2.89+ for $Li_{1.47}Mn_{1.6}O_{3.7}F_{0.3}$ and 3.05+ for $Li_2Mn_{1.6}O_{3.7}F_{0.3}$. Based on the characterized Mn valence change during discharge, the Mn reduction process contributes 1.48 e^-/f.u. to the observed 2.13 Li/f.u. capacity for $Li_{1.47}Mn_{1.6}O_{3.7}F_{0.3}$ (and 1.16 e^-/f.u. to the observed 2.20 Li/f.u. capacity for $Li_2Mn_{1.6}O_{3.7}F_{0.3}$). The discrepancy between the TM and overall capacity points to the participation of O redox.[142]

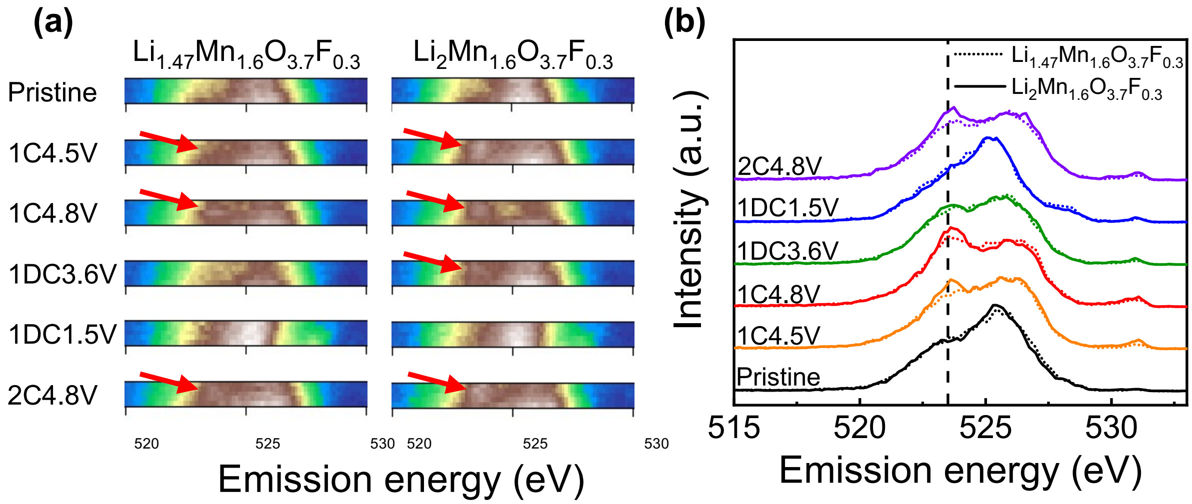

Figure 4-18. O Redox mechanism investigated by mapping of resonant inelastic X-ray scattering (mRIXS)**.** a. *Ex-situ* O K-edge mRIXS at selected states during the first cycle and the top of charge during the second cycle (top to bottom). Along the vertical axis is the excitation energy with a 1 eV window around 531 eV. b. Corresponding O mRIXS cuts at 531.0 eV excitation energy.

To more directly examine the contribution from anionic redox, mRIXS measurements at the O *K*-edge were conducted. Previous studies have established that a characteristic feature at 523.7 eV emission energy and 531.0 eV excitation energy is a fingerprint of bulk O oxidation.[138,142,143] We therefore mapped the RIXS signal in the vicinity of this region for a series of SOCs during the first cycle for $Li_{1.47}Mn_{1.6}O_{3.7}F_{0.3}$ and $Li_2Mn_{1.6}O_{3.7}F_{0.3}$. The results are shown in Figure 9a. In both compounds, the characteristic feature (highlighted by red arrows) is already present at 4.5 V and becomes stronger at 4.8 V (full mapping in **Figure 4-19**). During discharge, the feature reversibly fades and vanishes at 1.5 V. The two compounds with a different degree of cation disorder show different intensity of oxidized O at the same SOC, which is manifested in the RIXS cuts of O *K*-edge at the 531.0 eV excitation energy in **Figure 4-18b**. The black dashed line at 523.7 eV highlights the emission energy at which the oxidized O signal is expected to appear. At 4.5 V, $Li_2Mn_{1.6}O_{3.7}F_{0.3}$ shows a more intense oxidized O peak than $Li_{1.47}Mn_{1.6}O_{3.7}F_{0.3}$, indicating more O oxidation. The feature is also noticeably stronger for $Li_2Mn_{1.6}O_{3.7}F_{0.3}$ when further charged to 4.8 V and later discharged to 3.6 V. After vanishing at the end of discharge, the signal reappears when charged the second time to 4.8 V (**Figure 4-18a**) and shows a similar lineshape to that of 1C4.8V (**Figure 4-18b**), suggesting the reversible nature of the O redox processes.

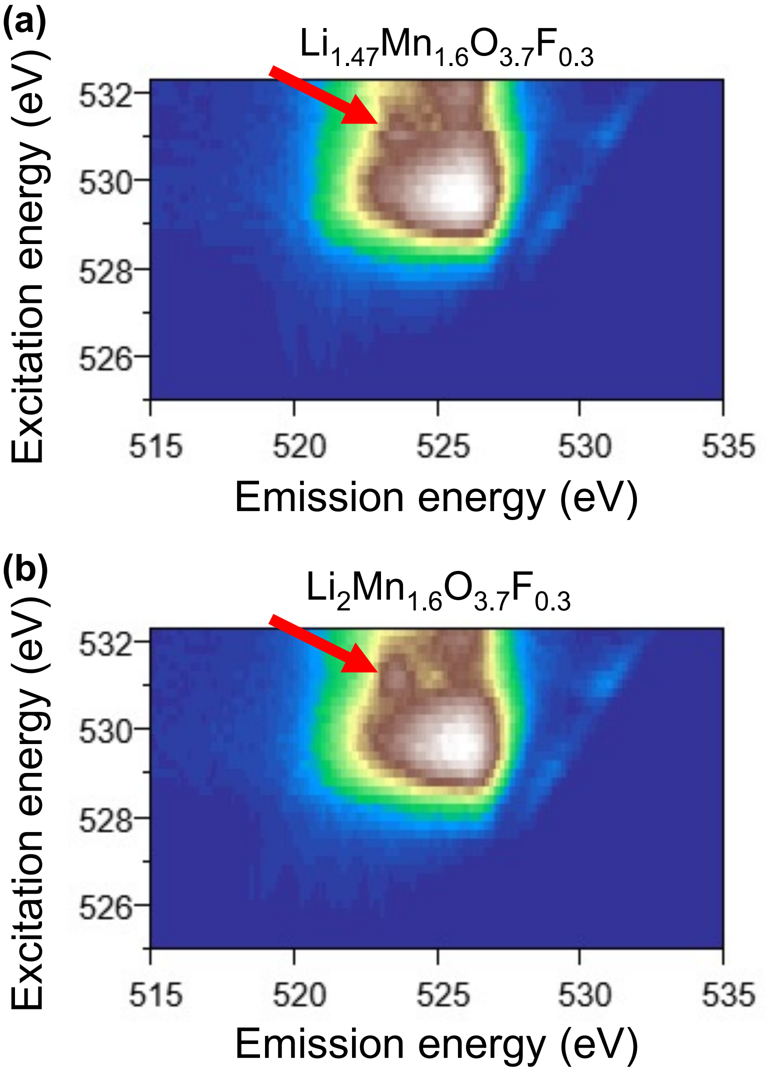

Figure 4-19. Ex-situ O K-edge mRIXS collected at 4.8 V during initial charge of (a) $Li_{1.47}Mn_{1.6}O_{3.7}F_{0.3}$ and (b) $Li_2Mn_{1.6}O_{3.7}F_{0.3}$

4.3 Discussion

Our work shows the remarkable potential of optimizing electrochemical performance by tuning cation disorder. In this work, we show three partially-(dis)ordered spinel compounds with high specific capacity, over 350 mAh g^{-1}, and specific energy over 1,000 Wh kg^{-1}. Among the three, $Li_{1.68}Mn_{1.6}O_{3.7}F_{0.3}$ was reported as an ultrahigh-power-density cathode in our previous work.[59] Here, by carefully tuning the cation disorder level, we find that $Li_{1.47}Mn_{1.6}O_{3.7}F_{0.3}$ delivers a superior specific energy compared to $Li_{1.68}Mn_{1.6}O_{3.7}F_{0.3}$ (**Figure 4-13b**) and many other state-of-the-art Li-ion cathodes.[59] While previous cathode discovery has focused on well-ordered compounds [144,145], and more recently on cation-disordered compounds [12,35,85,146], the current work shows the benefits of exploring the large space of partially ordered structures, where cation ordering, in addition to crystal structure, can be used as a design handle. By creating three compositions with increasing cation/anion ratio we bridge the gap between stoichiometric spinels (having a 3 to 4 cation/anion ratio) and rocksalts (with a 1 to 1 cation/anion ratio). While spinels are expected to have the highest intrinsic Li mobility due to their remarkable percolation of Li diffusion channels with low migration energy [34], the presence of the first order transition that displaces lithium from the 8a to 16c site is an extrinsic barrier to high rate charging, and furthermore leads to mechanically induced capacity degradation. These insights explain why remaining close to the spinel composition but introducing enough cation over-stoichiometry to remove the two-phase region, as in the $Li_{1.47}Mn_{1.6}O_{3.7}F_{0.3}$ composition, leads to the highest rate capability.

The three compounds evaluated here have the same Mn/anion and O/F ratio but only differ by their Li content in the synthesis. This difference may not appear important as the Li content will be changed upon electrochemical cycling, but our results indicate that the over-stoichiometry of cations (regulated by the amount of lithium) is needed to control the amount of Mn 16c/16d disorder in the synthesis. When the cation excess is low, more spinel-like material is obtained as evidenced by the stronger (111) reflection in the XRD (**Figure 4-2**), while a higher Li content brings the material closer to the rocksalt structure.

As we show in this work, tuning the degree of cation order alters the voltage profile, the rate capability, and the amount of oxygen redox (and hence the cycling stability). The voltage profile changes because the Gibbs free energy E as a function of Li content x_{Li} is modified by cation (dis)order and so is the voltage profile $\sim\frac{\delta E(x_{\mathrm{Li}})}{\delta x_{\mathrm{Li}}}$.[111,112] The chemical potential of Li in a fully-ordered spinel $LiMn_2O_4$ remains constant as the spinel is lithiated in the two-phase region, which leads to a voltage plateau of ~1 Li/f.u. near 3 V. However, in partially-disordered $Li_{1.47+x}Mn_{1.6}O_{3.7}F_{0.3}$, the voltage profile is sloping near 3 V, suggesting that the two-phase region is replaced by a solid solution reaction. *Ex-situ* synchrotron XRD in **Figure 4-20** further corroborates that both $Li_{1.47}Mn_{1.6}O_{3.7}F_{0.3}$ and $Li_2Mn_{1.6}O_{3.7}F_{0.3}$ retain cubic symmetry and are free of two phases when discharged to 2.9 and 2.7 V. The suppression of the two-phase region is consistent with fundamental ideas in statistical mechanics which have shown that at critical levels of site-energy disorder, a first order transition first collapses into a second order transition, and then becomes even fully suppressed for even larger site disorder.[147,148] In our materials the Mn 16c/16d disorder creates a statistical distribution of local environments which creates the site-energy disorder for Li and results in a sloping voltage profile.[111,112] Therefore, as x increases from 0.47 to 2, a very broad hump gradually appears in the dQ/dV plots and more capacity is delivered above 3 V (**Figure 4-9**).

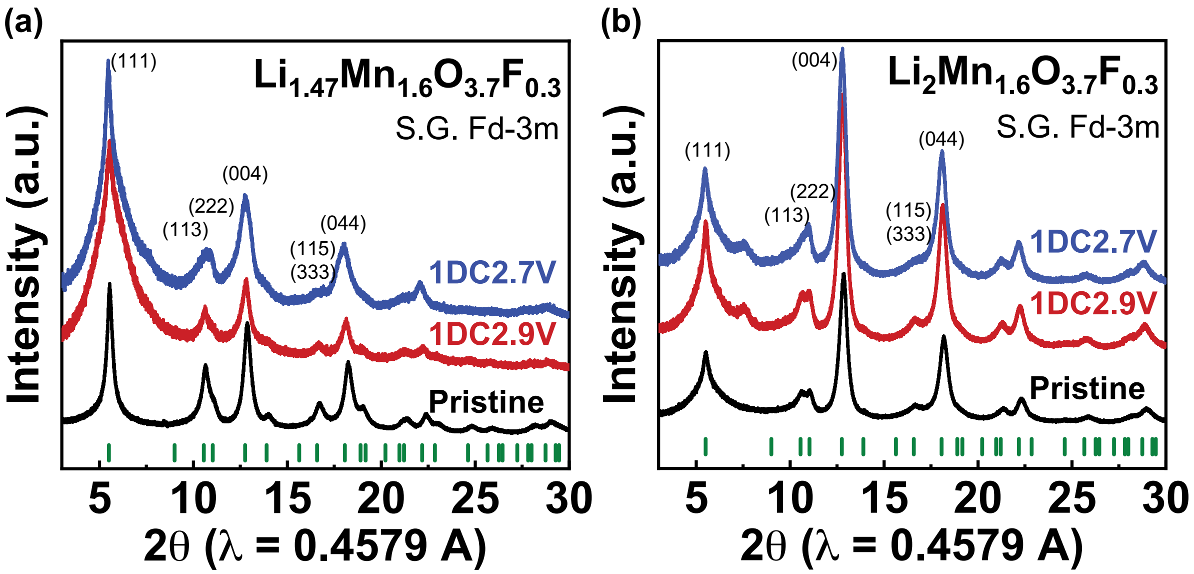

Figure 4-20. *Ex-situ* synchrotron XRD of cycled cathode samples. Synchrotron XRD patterns of the pristine and cycled samples of (a) $Li_{1.47}Mn_{1.6}O_{3.7}F_{0.3}$ and (b) $Li_2Mn_{1.6}O_{3.7}F_{0.3}$ The selected states of charge are pristine, first-cycle discharge to 2.9 V (red) and 2.7 V (blue). The green bar indicates the diffraction peak of spinel structure.

Consistent with our understanding of percolation in partially disordered spinels versus disordered rocksalts, rate capability is also affected by the cation order. In all but layered cathode materials [149], Li transport occurs through so-called 0-TM channels, which are tetrahedral sites that do not face-share with any TMs and their percolation.[10,34] Cation order in a rocksalt-type structure strongly affects the amount of such 0-TM channels and their percolation.[10,34,50,66,67,150] Of all the well-known cation orderings that can be found in a rocksalt host [4], spinel has the most favorable TM ordering for creating 0-TM channels, making it tolerant to a substantial amount of cation disorder. **Figure 4-21a** shows the calculated 0-TM percolated Li capacity in a rocksalt-type structure containing 20% Li-for-Mn substitution, when a fully spinel-ordered cation sublattice becomes increasingly disordered (black dots). The results are compared with those in a layered structure with the same Li-excess (red squares). As shown by these percolation simulations, the structure with a spinel-like cation order always has a higher accessible Li capacity, which monotonously decreases with cation disorder and eventually converges with that of the layered structure at complete cation disorder (that is, a DRX structure), rationalizing its high rate capability.

Finally, spinel-type ordering seems to have a previously unrecognized benefit in that it suppresses oxygen redox. We find that the amount of reversible O redox used in the spinel cathodes with various degrees of cation order is different, even though they have the same Mn content and the same average anion valence. As shown from the O *K*-edge mRIXS results in **Figure 4-18**, the more cation-disordered $Li_2Mn_{1.6}O_{3.7}F_{0.3}$ exhibits a stronger oxidized O feature at high voltage than the more spinel-like-ordered $Li_{1.47}Mn_{1.6}O_{3.7}F_{0.3}$. To elucidate the origin of such difference, we computationally analyzed the local environments surrounding O ions in a $Li_xMn_{1.6}O_{3.7}F_{0.3}$ spinel with an increasing degree of cation disorder. We focus on the linear Li-O-Li configurations in the structures because they are a major contributor to the unhybridized high-energy orphaned O states, which can be oxidized and reduced in a typical electrochemical voltage window.[87] In our simulations, we treat Li and vacancies as equivalent (Li-O-Li = Vacancy-O-Li = Vacancy-O-Vacancy) since neither hybridizes with the O 2*p* orbitals. We find that at 0% disorder, that is, Mn ions confined to the 16d sites, nearly 50% of O ions already have at least one Li-O-Li configuration. More disorder on the cation sublattice transfers Mn ions to the 16c sites until 16c and 16d are equally occupied for the case of 100% cation mixing. In this fully random state the fraction of O ions with at least one Li-O-Li configuration is increased to > 70% (**Figure 4-21b**). These results suggest that cation disorder increases the occurrence of Li-rich local environments around O ions makes a higher fraction of them prone to oxidation, consistent with our observation in mRIXS (**Figure 4-18**).

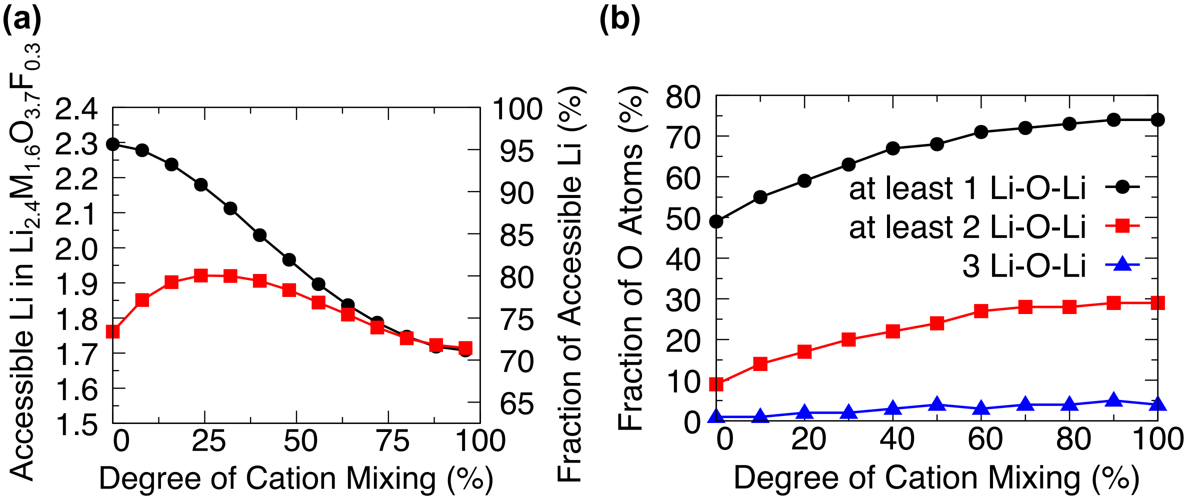

Figure 4-21. Amount of accessible Li and O local environments as a function of cation mixing (or disorder). a. The amount of kinetically accessible Li through 0-TM percolation in $Li_{2.4}TM_{1.6}O_{3.7}F_{0.3}$ varies with the degree of cation mixing for spinel-type (black dots) or layered (red squares) cation arrangement. The two plots converge at 100% cation mixing, which corresponds to complete cation disorder. b. The fraction of O atoms that have at least 1 linear Li-O-Li, at least 2 linear Li-O-Li or 3 linear Li-O-Li configurations in $Li_{2.4}TM_{1.6}O_4$. The influence of the low-level fluorination is neglected.

4.3 Conclusions

In this work, we successfully synthesized a series of Mn-based $Li_{1.4+x}Mn_{1.6}O_{3.7}F_{0.3}$ oxyfluorides with a varying degree of cation order (x = 0.07, 0.28, 0.6, and 1.0) through a mechanochemical method. High specific energy density > 1,000 Wh kg^{-1} (specific capacity > 350 mAh g^{-1}) is achieved in the three partially-(dis)ordered spinel cathodes with significant contribution from reversible O redox. As the Li-over-stoichiometry x in the synthesis increases, the structure transitions from mostly spinel-type to more disordered rocksalt. The cation disorder suppresses the two-phase region associated with the voltage plateau near 3 V and converts it into a solid solution. Through its effect on the local environments the tunable cation order also has a profound effect on rate capability, voltage profile, and redox mechanism. $Li_{1.47}Mn_{1.6}O_{3.7}F_{0.3}$ was found to exhibit the highest rate capability with > 158 mAh g^{-1} delivered at 7.5 A g^{-1}, while the more rocksalt-like $Li_2Mn_{1.6}O_{3.7}F_{0.3}$ utilizes the most O redox in the same voltage window.

Our work emphasizes the importance of exploring the continuum of structure space between well-known ordered compounds. While in our work these materials were produced by mechanochemical synthesis, understanding better how to access thermodynamically stable and metastable partial order by alternative synthesis methods, and how to integrate them into high loading composite cathodes, would be highly desirable to further explore this promising space.

Chapter 5 Summary and outlook

Compared to traditional commercialized layered rocksalt cathodes, DRX cathodes broaden the chemical space that can be used for Li-ion batteries, including some inexpensive and earth-abundant TMs such as Mn, Ti, V and Cr. Therefore, DRX materials are promising to resolve the sustainability and cost issues of cobalt and nickel as the Li-ion industry grows to 1TWh of production per year for which approximately one million tons of combined cobalt or nickel will be required. However, unlike the well-defined 2-D percolation pathway in layered rocksalt cathodes, the Li percolation relies on the 3-D quasi-randomly distributed 0-TM in the DRX structure. Although long-range disordered, the structure can process short-range order and even be partially ordered in a relatively longer scale. The local cation order controls the Li transport in these DRX cathodes in a significant way because the feasible Li hops require that the intermediate tetrahedral sites along the Li diffusion path are coordinated only by Li or vacancies. Extensive research efforts are needed to understand the correlation between local ordering and overall electrochemical performance. In this thesis, three strategies to modify local ordering in DRX cathodes were carefully evaluated, including metal doping on cation sublattices, synthesis condition control and cation partially order.

In Chapter 2, the role of cation doping on controlling the SRO and extractable Li in fluorinated DRX cathodes is carefully investigated. Due to the 'locking effect' caused by strong bonding between Li and F, not all the Li can be extracted even when charged to 4.8 V, which compromises the electrochemical performance. The screening based on the bonding strength and ionic radius was performed to identify the suitable dopant to free the locked Li. Mg was chosen due to its strong bonding with F and similar ionic radius with Li. A detailed theoretical investigation of Li–F SRO using DFT calculations and CE-MC simulations confirmed that Mg doping results in a greater fraction of extractable Li ions by reducing the frequency of the Li_6F configuration. We verified our hypothesis by comparing the electrochemical performance of $Li_{1.25}Mn_{0.45}Ti_{0.3}O_{1.8}F_{0.2}$ and $Li_{1.25}Mg_{0.1}Mn_{0.45}Nb_{0.2}O_{1.8}F_{0.2}$. Although both compounds have the same Li-excess level, Mn valence and Mn content, the Mg-doped compound has higher capacity. Finally, we extended the discussion to a related group of compositions: $Li_{1.333}Mn_{0.667}O_{1.333}F_{0.667}$ (LMF), $Li_{1.233}Mg_{0.1}Mn_{0.667}O_{1.333}F_{0.667}$ (ls-LMF), $Li_{1.333}Mg_{0.1}Mn_{0.567}O_{1.333}F_{0.667}$ (ms-LMF) and $Li_{1.28}Mg_{0.11}Mn_{0.61}O_{1.333}F_{0.667}$ (ls-LMF). We demonstrated that the improved accessible Li, enabled by Mg doping, can also be traded to improve cycle life. The results showed that Mg-doping strategy should be considered in fluorinated cathodes, to optimize DRX oxyfluoride cathodes.

In Chapter 3, the solid-state synthesis mechanism of a typical DRX oxyfluoride, $Li_{1.2}Mn_{0.55}Ti_{0.25}O_{1.85}F_{0.15}$ (LMTF), were studied to investigate the formation of long-range order and short-range order. Experimentally, through *in-situ* TEM, *ex-situ* XRD and PDF analysis, the formation of long-range disorder followed by short-range order during the synthesis was clearly demonstrated. This phenomenon was further understood by performing *ab initio* calculations for the formation energy of DRX with random structure and with SRO to estimate the reaction kinetics. Based on both experimental and simulation results, the SRO feature can be eliminated by simply shortening sintering time and quenching from high temperature. With this strategy, the SRO-free LMTF (35 min) sample exhibited a capacity of >310 mAh g^{-1} and a specific energy close to 1000 Wh kg^{-1} and enables discharge up to 2 A g^{-1}, which is much better than SRO-rich LMTF (4h).

In Chapter 4, cation to anion ratio in synthesis was identified as a key parameter for tuning the structure continuously from a well-ordered spinel, through a partially ordered spinel, to a rocksalt. A series of well selected partially-(dis)ordered spinel cathodes with different degree of over-stoichiometry, $Li_{1.4+x}Mn_{1.6}O_{3.7}F_{0.3}$ (x = 0.07, 0.28, and 0.6), was synthesized via a mechanochemical method. The degree of cation disorder continuously varies with cation to anion ratio, which modifies the voltage profile, rate capability, and charge-compensation mechanism in a rational and predictable way. The results indicate that spinel-type order is most beneficial for achieving high-rate performance as long as the first-order phase transition at ~ 3 V is suppressed. Besides, we also found that more rocksalt-like disorder facilitates O redox, which can increase capacity. These findings reveal an important tuning handle for achieving high energy and power in the vast space of partially ordered cathode materials.

We found that introducing spinel order to DRX might be the best way to optimize the electrochemical performance, as it greatly improves the energy density and power density. However, the partial ordering can only be achieved by mechanochemical high-energy ball-milling method, which cannot be practically applied in industry. Therefore, it is significantly important to better understand how to access thermodynamically stable and metastable partial order by alternative synthesis methods. In the future, low temperature synthesis methods might be worth studying as the low temperature can only activate cation migration without destroy the anion framework to form impurity phases. Therefore, the partially disordered spinel cathodes might form at low temperature if the structure of precursors and synthesis condition are well optimized.

References

1 Van der Ven, A., Bhattacharya, J. & Belak, A. A. Understanding Li diffusion in Li-intercalation compounds. *Accounts of chemical research* **46**, 1216-1225 (2013).

2 Olivetti, E. A., Ceder, G., Gaustad, G. G. & Fu, X. K. Lithium-Ion Battery Supply Chain Considerations: Analysis of Potential Bottlenecks in Critical Metals. *Joule* **1**, 229-243, doi:10.1016/j.joule.2017.08.019 (2017).

3 Summaries, M. C. Mineral commodity summaries. *US Geological Survey: Reston, VA, USA* **200** (2021).

4 Wu, E. J., Tepesch, P. D. & Ceder, G. Size and charge effects on the structural stability of LiMO2 (M= transition metal) compounds. *Philosophical Magazine B* **77**, 1039-1047 (1998).

5 Whittingham, M. S. Lithium batteries and cathode materials. *Chemical reviews* **104**, 4271-4302 (2004).

6 Goodenough, J. B. & Kim, Y. Challenges for rechargeable Li batteries. *Chemistry of materials* **22**, 587-603 (2010).

7 Turcheniuk, K., Bondarev, D., Singhal, V. & Yushin, G. (Nature Publishing Group, 2018).

8 Obrovac, M. N., Mao, O. & Dahn, J. R. Structure and electrochemistry of LiMO2 (M= Ti, Mn, Fe, Co, Ni) prepared by mechanochemical synthesis. *Solid State Ionics* **112**, 9-19 (1998).

9 Ji, H. W. *et al.* Computational Investigation and Experimental Realization of Disordered High-Capacity Li-Ion Cathodes Based on Ni Redox. *Chemistry of Materials* **31**, 2431-2442, doi:10.1021/acs.chemmater.8b05096 (2019).

10 Ji, H. *et al.* Hidden structural and chemical order controls lithium transport in cation-disordered oxides for rechargeable batteries. *Nat Commun* **10**, 592, doi:10.1038/s41467-019-08490-w (2019).

11 Chen, D., Kan, W. H. & Chen, G. Understanding Performance Degradation in Cation-Disordered Rock-Salt Oxide Cathodes. *Advanced Energy Materials*, 1901255 (2019).

12 Lee, J. *et al.* Reversible Mn 2+/Mn 4+ double redox in lithium-excess cathode materials. *Nature* **556**, 185 (2018).

13 Kitchaev, D. A. *et al.* Design principles for high transition metal capacity in disordered rocksalt Li-ion cathodes. *Energy & Environmental Science* **11**, 2159-2171, doi:10.1039/c8ee00816g (2018).

14 Kan, W. H. *et al.* Understanding the Effect of Local Short-Range Ordering on Lithium Diffusion in Li1.3Nb0.3Mn0.4O2 Single-Crystal Cathode. *Chem* **4**, 2108-2123, doi:10.1016/j.chempr.2018.05.008 (2018).

15 Kan, W. H. *et al.* Unravelling Solid-State Redox Chemistry in Li1.3Nb0.3Mn0.4O2 Single-Crystal Cathode Material. *Chemistry of Materials* **30**, 1655-1666, doi:10.1021/acs.chemmater.7b05036 (2018).

16 House, R. A. *et al.* Lithium manganese oxyfluoride as a new cathode material exhibiting oxygen redox. *Energy & Environmental Science* **11**, 926-932, doi:10.1039/c7ee03195e (2018).

17 Urban, A., Abdellahi, A., Dacek, S., Artrith, N. & Ceder, G. Electronic-Structure Origin of Cation Disorder in Transition-Metal Oxides. *Phys Rev Lett* **119**, 176402, doi:10.1103/PhysRevLett.119.176402 (2017).

18 Takeda, N. *et al.* Reversible Li storage for nanosize cation/anion-disordered rocksalt-type oxyfluorides: LiMoO 2 – x LiF (0 ≤ x ≤ 2) binary system. *Journal of Power Sources* **367**, 122-129, doi:10.1016/j.jpowsour.2017.09.060 (2017).

19 Lee, J. *et al.* Mitigating oxygen loss to improve the cycling performance of high capacity cation-disordered cathode materials. *Nat Commun* **8**, 981, doi:10.1038/s41467-017-01115-0 (2017).

20 Hoshino, S. *et al.* Reversible Three-Electron Redox Reaction of Mo3+/Mo6+ for Rechargeable Lithium Batteries. *Acs Energy Letters* **2**, 733-738, doi:10.1021/acsenergylett.7b00037 (2017).

21 Freire, M., Lebedev, O. I., Maignan, A., Jordy, C. & Pralong, V. Nanostructured Li 2 MnO 3: a disordered rock salt type structure for high energy density Li ion batteries. *Journal of Materials Chemistry A* **5**, 21898-21902 (2017).

22 Yabuuchi, N., Tahara, Y., Komaba, S., Kitada, S. & Kajiya, Y. Synthesis and Electrochemical Properties of Li4MoO5-NiO Binary System as Positive Electrode Materials for Rechargeable Lithium Batteries. *Chemistry of Materials* **28**, 416-419, doi:10.1021/acs.chemmater.5b04092 (2016).

23 Yabuuchi, N. *et al.* Origin of stabilization and destabilization in solid-state redox reaction of oxide ions for lithium-ion batteries. *Nat Commun* **7**, 13814, doi:10.1038/ncomms13814 (2016).

24 Urban, A., Seo, D.-H. & Ceder, G. Computational understanding of Li-ion batteries. *npj Computational Materials* **2**, 16002 (2016).

25 Urban, A., Matts, I., Abdellahi, A. & Ceder, G. Computational Design and Preparation of Cation-Disordered Oxides for High-Energy-Density Li-Ion Batteries. *Advanced Energy Materials* **6**, 1600488 (2016).

26 Chen, R. *et al.* Identifying the redox activity of cation-disordered Li-Fe-V-Ti oxide cathodes for Li-ion batteries. *Phys Chem Chem Phys* **18**, 7695-7701, doi:10.1039/c6cp00131a (2016).

27 Chen, R. *et al.* High-Performance Low-Temperature Li+ Intercalation in Disordered Rock-Salt Li–Cr–V Oxyfluorides. *ChemElectroChem* **3**, 892-895 (2016).

28 Yabuuchi, N. *et al.* High-capacity electrode materials for rechargeable lithium batteries: Li3NbO4-based system with cation-disordered rocksalt structure. *Proc Natl Acad Sci U S A* **112**, 7650-7655, doi:10.1073/pnas.1504901112 (2015).

29 Wang, R. *et al.* A disordered rock-salt Li-excess cathode material with high capacity and substantial oxygen redox activity: Li1.25Nb0.25Mn0.5O2. *Electrochemistry Communications* **60**, 70-73, doi:10.1016/j.elecom.2015.08.003 (2015).

30 Lee, J. *et al.* A new class of high capacity cation-disordered oxides for rechargeable lithium batteries: Li-Ni-Ti-Mo oxides. *Energy & Environmental Science* **8**, 3255-3265, doi:10.1039/c5ee02329g (2015).

31 Glazier, S. L., Li, J., Zhou, J., Bond, T. & Dahn, J. R. Characterization of disordered Li (1+ x) Ti2 x Fe (1–3 x) O2 as positive electrode materials in Li-Ion batteries using percolation theory. *Chemistry of Materials* **27**, 7751-7756 (2015).

32 Chen, R. *et al.* Li+ intercalation in isostructural Li 2 VO 3 and Li 2 VO 2 F with O 2− and mixed O 2−/F− anions. *Physical Chemistry Chemical Physics* **17**, 17288-17295 (2015).

33 Chen, R. *et al.* Disordered Lithium-Rich Oxyfluoride as a Stable Host for Enhanced Li+ Intercalation Storage. *Advanced Energy Materials* **5**, 1401814 (2015).

34 Urban, A., Lee, J. & Ceder, G. The Configurational Space of Rocksalt-Type Oxides for High-Capacity Lithium Battery Electrodes. *Advanced Energy Materials* **4**, 1400478 (2014).

35 Lee, J. *et al.* Unlocking the potential of cation-disordered oxides for rechargeable lithium batteries. *Science* **343**, 519-522 (2014).

36 Zheng, S. *et al.* Novel Ordered Rocksalt-Type Lithium-Rich Li2Ru1–x Ni x O3− δ (0.3≤ x≤ 0.5) Cathode Material with Tunable Anionic Redox Potential. *ACS Applied Energy Materials* **2**, 5933-5944 (2019).

37 Yu, Z. *et al.* Synthesis and Redox Mechanism of Cation-Disordered, Rock-Salt Cathode-Material Li-Ni-Ti-Nb-O Compounds for a Li-Ion Battery. *ACS Appl Mater Interfaces* **11**, 35777-35787, doi:10.1021/acsami.9b12822 (2019).

38 Yang, M. *et al.* Cation-Disordered Lithium-Excess Li-Fe-Ti Oxide Cathode Materials for Enhanced Li-Ion Storage. *ACS Appl Mater Interfaces* **11**, 44144-44152, doi:10.1021/acsami.9b14137 (2019).

39 Wang, R. *et al.* Research on the kinetic properties of the cation disordered rock-salt Li-excess Li1.25Nb0.25Mn0.5O2 material. *Solid State Ionics* **339**, 114999, doi:ARTN
114999
10.1016/j.ssi.2019.06.007 (2019).

40 Takeda, N., Ikeuchi, I., Natsui, R., Nakura, K. & Yabuuchi, N. Improved Electrode Performance of Lithium-Excess Molybdenum Oxyfluoride: Titanium Substitution with Concentrated Electrolyte. *Acs Applied Energy Materials* **2**, 1629-1633, doi:10.1021/acsaem.9b00135 (2019).

41 Lun, Z. *et al.* Improved Cycling Performance of Li-Excess Cation-Disordered Cathode Materials upon Fluorine Substitution. *Advanced Energy Materials* **9**, 1802959 (2019).

42 Kan, W. H. *et al.* Evolution of Local Structural Ordering and Chemical Distribution upon Delithiation of a Rock Salt Structured Li1.3Ta0.3Mn0.4O2 Cathode. *Advanced Functional Materials* **29**, 1808294 (2019).

43 Källquist, I. *et al.* Degradation mechanisms in Li2VO2F Li-rich disordered rock-salt cathodes. *Chemistry of Materials* (2019).

44 Jones, M. A. *et al.* Short-range ordering in a battery electrode, the 'cation-disordered'rocksalt Li 1.25 Nb 0.25 Mn 0.5 O 2. *Chemical Communications* **55**, 9027-9030 (2019).

45 Van der Ven, A. & Ceder, G. Lithium diffusion in layered Li x CoO2. *Electrochemical and Solid-State Letters* **3**, 301 (2000).

46 Van der Ven, A. & Ceder, G. Lithium diffusion mechanisms in layered intercalation compounds. *Journal of power sources* **97**, 529-531 (2001).

47 Catti, M. Ab initio study of Li+ diffusion paths in the monoclinic Li 0.5 CoO 2 intercalate. *Physical Review B* **61**, 1795 (2000).

48 Kang, K., Meng, Y. S., Breger, J., Grey, C. P. & Ceder, G. Electrodes with high power and high capacity for rechargeable lithium batteries. *Science* **311**, 977-980 (2006).

49 Kang, K. & Ceder, G. Factors that affect Li mobility in layered lithium transition metal oxides. *Physical Review B* **74**, 094105 (2006).

50 Clément, R. J., Kitchaev, D., Lee, J. & Ceder, G. Short-range order and unusual modes of nickel redox in a fluorine-substituted disordered rocksalt oxide lithium-ion cathode. *Chemistry of Materials* **30**, 6945-6956 (2018).

51 De Fontaine, D. An analysis of clustering and ordering in multicomponent solid solutions—II fluctuations and kinetics. *Journal of Physics and Chemistry of Solids* **34**, 1285-1304 (1973).

52 Ducastelle, F. in *Interatomic Potential and Structural Stability* 133-142 (Springer, 1993).

53 Reinhard, L. & Moss, S. Recent studies of short-range order in alloys: the Cowley theory revisited. *Ultramicroscopy* **52**, 223-232 (1993).

54 Thackeray, M. M., David, W. I. F., Bruce, P. G. & Goodenough, J. B. Lithium insertion into manganese spinels. *Materials Research Bulletin* **18**, 461-472 (1983).

55 Gummow, R. J., De Kock, A. & Thackeray, M. M. Improved capacity retention in rechargeable 4 V lithium/lithium manganese oxide (spinel) cells. (1994).

56 Lee, E.-S., Nam, K.-W., Hu, E. & Manthiram, A. Influence of cation ordering and lattice distortion on the charge–discharge behavior of LiMn1. 5Ni0. 5O4 spinel between 5.0 and 2.0 V. *Chemistry of Materials* **24**, 3610-3620 (2012).

57 Liu, Y. *et al.* Low-Temperature Synthesized Li4Mn5O12-Like Cathode with Hybrid Cation-and Anion-Redox Capacities. *Chemical Communications* (2019).

58 Thackeray, M. M. *et al.* Spinel electrodes from the Li-Mn-O system for rechargeable lithium battery applications. *Journal of The Electrochemical Society* **139**, 363 (1992).

59 Ji, H. W. *et al.* Ultrahigh power and energy density in partially ordered lithium-ion cathode materials. *Nature Energy* **5**, 213-221, doi:10.1038/s41560-020-0573-1 (2020).

60 Richards, W. D., Dacek, S. T., Kitchaev, D. A. & Ceder, G. Fluorination of Lithium-Excess Transition Metal Oxide Cathode Materials. *Advanced Energy Materials* **8**, 1701533 (2018).

61 Fu, X. *et al.* Perspectives on Cobalt Supply through 2030 in the Face of Changing Demand. *Environ Sci Technol* **54**, 2985-2993, doi:10.1021/acs.est.9b04975 (2020).

62 Meng, Y. S. & Arroyo-de Dompablo, M. E. Recent advances in first principles computational research of cathode materials for lithium-ion batteries. *Accounts of chemical research* **46**, 1171-1180 (2013).

63 Baur, C. *et al.* Improved cycling stability in high-capacity Li-rich vanadium containing disordered rock salt oxyfluoride cathodes. *Journal of Materials Chemistry A* **7**, 21244-21253 (2019).

64 Naylor, A. J. *et al.* Stabilization of Li-Rich Disordered Rocksalt Oxyfluoride Cathodes by Particle Surface Modification. *ACS applied energy materials* **3**, 5937-5948 (2020).

65 Mozhzhukhina, N. *et al.* Short-range ordering in the Li-rich disordered rock salt cathode material Li2VO2F revealed by Raman spectroscopy. *Journal of Raman Spectroscopy* **51**, 2095-2101 (2020).

66 Lun, Z. Y. *et al.* Design Principles for High-Capacity Mn-Based Cation-Disordered Rocksalt Cathodes. *Chem* **6**, 153-168, doi:10.1016/j.chempr.2019.10.001 (2020).

67 Ouyang, B. *et al.* Effect of Fluorination on Lithium Transport and Short-Range Order in Disordered-Rocksalt-Type Lithium-Ion Battery Cathodes. *Advanced Energy Materials* **10**, 1903240 (2020).

68 Pell, A. J., Clément, R. J., Grey, C. P., Emsley, L. & Pintacuda, G. Frequency-stepped acquisition in nuclear magnetic resonance spectroscopy under magic angle spinning. *The Journal of chemical physics* **138**, 114201 (2013).

69 O'Dell, L. A., Rossini, A. J. & Schurko, R. W. Acquisition of ultra-wideline NMR spectra from quadrupolar nuclei by frequency stepped WURST–QCPMG. *Chemical physics letters* **468**, 330-335 (2009).

70 Sananes, M. T., Tuel, A., Volta, J. C. & Hutchings, G. J. Characterization of different precursors and activated vanadium phosphate catalysts by [sup 31] P NMR spin echo mapping. *Journal of Catalysis;(United States)* **148** (1994).

71 Massiot, D. *et al.* 71Ga and 69Ga nuclear magnetic resonance study of β-Ga2O3: resolution of four-and six-fold coordinated Ga sites in static conditions. *Solid State Nuclear Magnetic Resonance* **4**, 241-248 (1995).

72 Van der Ven, A., Aydinol, M., Ceder, G., Kresse, G. & Hafner, J. First-principles investigation of phase stability in Li x CoO 2. *Physical Review B* **58**, 2975 (1998).

73 Tepesch, P., Garbulsky, G. & Ceder, G. Model for configurational thermodynamics in ionic systems. *Physical review letters* **74**, 2272 (1995).

74 Nelson, L. J., Hart, G. L., Zhou, F. & Ozoliņš, V. Compressive sensing as a paradigm for building physics models. *Physical Review B* **87**, 035125 (2013).

75 van de Walle, A. & Ceder, G. Automating first-principles phase diagram calculations. *Journal of Phase Equilibria* **23**, 348-359 (2002).

76 Kresse, G. & Furthmüller, J. Efficient iterative schemes for ab initio total-energy calculations using a plane-wave basis set. *Physical review B* **54**, 11169 (1996).

77 Kresse, G. & Joubert, D. From ultrasoft pseudopotentials to the projector augmented-wave method. *Physical review b* **59**, 1758 (1999).

78 Perdew, J. P., Burke, K. & Ernzerhof, M. Generalized gradient approximation made simple. *Physical review letters* **77**, 3865 (1996).

79 Wang, L., Maxisch, T. & Ceder, G. Oxidation energies of transition metal oxides within the GGA+ U framework. *Physical Review B* **73**, 195107 (2006).

80 Jain, A. *et al.* Formation enthalpies by mixing GGA and GGA+ U calculations. *Physical Review B* **84**, 045115 (2011).

81 Jain, A. *et al.* Commentary: The Materials Project: A materials genome approach to accelerating materials innovation. *APL materials* **1**, 011002 (2013).

82 Hume-Rothery, W. & Powell, H. M. On the theory of super-lattice structures in alloys. *Zeitschrift für Kristallographie-Crystalline Materials* **91**, 23-47 (1935).

83 Shannon, R. D. Revised effective ionic radii and systematic studies of interatomic distances in halides and chalcogenides. *Acta crystallographica section A: crystal physics, diffraction, theoretical and general crystallography* **32**, 751-767 (1976).

84 Chen, D. *et al.* Role of Redox-Inactive Transition-Metals in the Behavior of Cation-Disordered Rocksalt Cathodes. *Small* **16**, e2000656, doi:10.1002/smll.202000656 (2020).

85 Clément, R. J., Lun, Z. & Ceder, G. Cation-disordered rocksalt transition metal oxides and oxyfluorides for high energy lithium-ion cathodes. *Energy & Environmental Science* **13**, 345-373 (2020).

86 Kataoka, R., Kojima, T. & Takeichi, N. Electrochemical property of Li-Mn cation disordered Li-Rich Li2MnO3 with NaCl type structure. *Journal of The Electrochemical Society* **165**, A291 (2018).

87 Seo, D. H. *et al.* The structural and chemical origin of the oxygen redox activity in layered and cation-disordered Li-excess cathode materials. *Nat Chem* **8**, 692-697, doi:10.1038/nchem.2524 (2016).

88 Andersson, J.-O., Helander, T., Höglund, L., Shi, P. & Sundman, B. Thermo-Calc & DICTRA, computational tools for materials science. *Calphad* **26**, 273-312 (2002).

89 Ong, S. P., Wang, L., Kang, B. & Ceder, G. Li− Fe− P− O2 phase diagram from first principles calculations. *Chemistry of Materials* **20**, 1798-1807 (2008).

90 Sopoušek, J. *et al.* Au-Ni nanoparticles: Phase diagram prediction, synthesis, characterization, and thermal stability. *Calphad* **58**, 25-33 (2017).

91 Shoemaker, D. P. *et al.* In situ studies of a platform for metastable inorganic crystal growth and materials discovery. *Proceedings of the National Academy of Sciences* **111**, 10922-10927 (2014).

92 Martinolich, A. J. & Neilson, J. R. Toward reaction-by-design: achieving kinetic control of solid state chemistry with metathesis. *Chemistry of Materials* **29**, 479-489 (2017).

93 Duan, Y. *et al.* Insights into Li/Ni ordering and surface reconstruction during synthesis of Ni-rich layered oxides. *Journal of Materials Chemistry A* **7**, 513-519 (2019).

94 Bianchini, M. *et al.* The interplay between thermodynamics and kinetics in the solid-state synthesis of layered oxides. *Nature materials* **19**, 1088-1095 (2020).

95 Miura, A. *et al.* Observing and Modeling the Sequential Pairwise Reactions that Drive Solid-State Ceramic Synthesis. *Advanced Materials*, 2100312 (2021).

96 Todd, P. K. *et al.* Selectivity in Yttrium Manganese Oxide Synthesis via Local Chemical Potentials in Hyperdimensional Phase Space. *Journal of the American Chemical Society* **143**, 15185-15194 (2021).

97 Yabuuchi, N. Material Design Concept of Lithium-Excess Electrode Materials with Rocksalt-Related Structures for Rechargeable Non-Aqueous Batteries. *The Chemical Record* **19**, 690-707 (2019).

98 Reed, J. & Ceder, G. Role of electronic structure in the susceptibility of metastable transition-metal oxide structures to transformation. *Chemical reviews* **104**, 4513-4534 (2004).

99 Lun, Z. *et al.* Cation-disordered rocksalt-type high-entropy cathodes for Li-ion batteries. *Nat Mater* **20**, 214-221, doi:10.1038/s41563-020-00816-0 (2021).

100 Sanchez, J. M., Ducastelle, F. & Gratias, D. Generalized cluster description of multicomponent systems. *Physica A: Statistical Mechanics and its Applications* **128**, 334-350, doi:https://doi.org/10.1016/0378-4371(84)90096-7 (1984).

101 Wolverton, C. & de Fontaine, D. Cluster expansions of alloy energetics in ternary intermetallics. *Physical Review B* **49**, 8627-8642, doi:10.1103/PhysRevB.49.8627 (1994).

102 Nelson, L. J., Hart, G. L. W., Zhou, F. & Ozoliņš, V. Compressive sensing as a paradigm for building physics models. *Physical Review B* **87**, 035125, doi:10.1103/PhysRevB.87.035125 (2013).

103 Lun, Z. *et al.* Design Principles for High-Capacity Mn-Based Cation-Disordered Rocksalt Cathodes. *Chem*, doi:https://doi.org/10.1016/j.chempr.2019.10.001 (2019).

104 Ouyang, B. *et al.* Effect of Fluorination on Lithium Transport and Short-Range Order in Disordered-Rocksalt-Type Lithium-Ion Battery Cathodes. *Advanced Energy Materials* **10**, 1903240, doi:https://doi.org/10.1002/aenm.201903240 (2020).

105 Kitchaev, D. A. *et al.* Design principles for high transition metal capacity in disordered rocksalt Li-ion cathodes. *Energy & Environmental Science* **11**, 2159-2171, doi:10.1039/c8ee00816g (2018).

106 Ji, H. *et al.* Computational Investigation and Experimental Realization of Disordered High-Capacity Li-Ion Cathodes Based on Ni Redox. *Chemistry of Materials* **31**, 2431-2442, doi:10.1021/acs.chemmater.8b05096 (2019).

107 Zunger, A., Wei, S. H., Ferreira, L. G. & Bernard, J. E. Special quasirandom structures. *Physical Review Letters* **65**, 353-356, doi:10.1103/PhysRevLett.65.353 (1990).

108 Shin, D., van de Walle, A., Wang, Y. & Liu, Z.-K. First-principles study of ternary fcc solution phases from special quasirandom structures. *Physical Review B* **76**, 144204, doi:10.1103/PhysRevB.76.144204 (2007).

109 Wei, S. H., Ferreira, L. G., Bernard, J. E. & Zunger, A. Electronic properties of random alloys: Special quasirandom structures. *Physical Review B* **42**, 9622-9649, doi:10.1103/PhysRevB.42.9622 (1990).

110 Urban, A., Matts, I., Abdellahi, A. & Ceder, G. Computational Design and Preparation of Cation-Disordered Oxides for High-Energy-Density Li-Ion Batteries. *Advanced Energy Materials* **6**, 1600488, doi:10.1002/aenm.201600488 (2016).

111 Abdellahi, A., Urban, A., Dacek, S. & Ceder, G. The Effect of Cation Disorder on the Average Li Intercalation Voltage of Transition-Metal Oxides. *Chemistry of Materials* **28**, 3659-3665, doi:10.1021/acs.chemmater.6b00205 (2016).

112 Abdellahi, A., Urban, A., Dacek, S. & Ceder, G. Understanding the Effect of Cation Disorder on the Voltage Profile of Lithium Transition-Metal Oxides. *Chemistry of Materials* **28**, 5373-5383, doi:10.1021/acs.chemmater.6b01438 (2016).

113 Kresse, G. & Joubert, D. From ultrasoft pseudopotentials to the projector augmented-wave method. *Physical Review B* **59**, 1758-1775, doi:10.1103/PhysRevB.59.1758 (1999).

114 Kresse, G. & Furthmüller, J. Efficiency of ab-initio total energy calculations for metals and semiconductors using a plane-wave basis set. *Computational Materials Science* **6**, 15-50, doi:https://doi.org/10.1016/0927-0256(96)00008-0 (1996).

115 Dudarev, S. L., Botton, G. A., Savrasov, S. Y., Humphreys, C. J. & Sutton, A. P. Electron-energy-loss spectra and the structural stability of nickel oxide: An LSDA+U study. *Physical Review B* **57**, 1505-1509, doi:10.1103/PhysRevB.57.1505 (1998).

116 Wang, L., Maxisch, T. & Ceder, G. Oxidation energies of transition metal oxides within the GGA+U framework. *Physical Review B* **73**, 195107, doi:10.1103/PhysRevB.73.195107 (2006).

117 De Ridder, R., Van Tendeloo, G. & Amelinckx, S. A cluster model for the transition from the short-range order to the long-range order state in fcc based binary systems and its study by means of electron diffraction. *Acta Crystallographica Section A: Crystal Physics, Diffraction, Theoretical and General Crystallography* **32**, 216-224 (1976).

118 Chupas, P. J. *et al.* A versatile sample-environment cell for non-ambient X-ray scattering experiments. *Journal of Applied Crystallography* **41**, 822-824 (2008).

119 Miura, A. *et al.* Selective metathesis synthesis of MgCr 2 S 4 by control of thermodynamic driving forces. *Materials horizons* **7**, 1310-1316 (2020).

120 McDermott, M. J., Dwaraknath, S. S. & Persson, K. A. A graph-based network for predicting chemical reaction pathways in solid-state materials synthesis. *Nature communications* **12**, 1-12 (2021).

121 Xu, C., Reeves, P. J., Jacquet, Q. & Grey, C. P. Phase Behavior during Electrochemical Cycling of Ni-Rich Cathode Materials for Li-Ion Batteries. *Advanced Energy Materials* **11**, 2003404 (2021).

122 Orlova, E. D., Savina, A. A., Abakumov, S. A., Morozov, A. V. & Abakumov, A. M. Comprehensive Study of Li+/Ni2+ Disorder in Ni-Rich NMCs Cathodes for Li-Ion Batteries. *Symmetry* **13**, 1628 (2021).

123 Zhang, X. *et al.* Catalytically active single-atom niobium in graphitic layers. *Nature communications* **4**, 1-7 (2013).

124 Deng, J. *et al.* Triggering the electrocatalytic hydrogen evolution activity of the inert two-dimensional MoS 2 surface via single-atom metal doping. *Energy & Environmental Science* **8**, 1594-1601 (2015).

125 Li, Z. *et al.* Iridium single-atom catalyst on nitrogen-doped carbon for formic acid oxidation synthesized using a general host–guest strategy. *Nature chemistry* **12**, 764-772 (2020).

126 Reed, J., Ceder, G. & Van Der Ven, A. Layered-to-spinel phase transition in Li x MnO2. *Electrochemical and Solid State Letters* **4**, A78 (2001).

127 Lee, E. & Persson, K. A. Solid-Solution Li Intercalation as a Function of Cation Order/Disorder in the High-Voltage Li x Ni0. 5Mn1. 5O4 Spinel. *Chemistry of Materials* **25**, 2885-2889 (2013).

128 Bianchini, M., Suard, E., Croguennec, L. & Masquelier, C. Li-Rich Li1+ x Mn2–x O4 Spinel Electrode Materials: An Operando Neutron Diffraction Study during Li+ Extraction/Insertion. *The Journal of Physical Chemistry C* **118**, 25947-25955 (2014).

129 Ravel, B. & Newville, M. ATHENA, ARTEMIS, HEPHAESTUS: data analysis for X-ray absorption spectroscopy using IFEFFIT. *Journal of synchrotron radiation* **12**, 537-541 (2005).

130 Qiao, R. *et al.* High-efficiency in situ resonant inelastic x-ray scattering (iRIXS) endstation at the Advanced Light Source. *Review of Scientific Instruments* **88**, 033106 (2017).

131 Chuang, Y.-D. *et al.* Modular soft x-ray spectrometer for applications in energy sciences and quantum materials. *Review of Scientific Instruments* **88**, 013110 (2017).

132 Li, Q. *et al.* Quantitative probe of the transition metal redox in battery electrodes through soft x-ray absorption spectroscopy. *Journal of Physics D: Applied Physics* **49**, 413003 (2016).

133 Hung, I., Zhou, L., Pourpoint, F. d. r., Grey, C. P. & Gan, Z. Isotropic high field NMR spectra of Li-ion battery materials with anisotropy> 1 MHz. *Journal of the American Chemical Society* **134**, 1898-1901 (2012).

134 McCloskey, B. D., Bethune, D. S., Shelby, R. M., Girishkumar, G. & Luntz, A. C. Solvents' critical role in nonaqueous lithium–oxygen battery electrochemistry. *The Journal of Physical Chemistry Letters* **2**, 1161-1166 (2011).

135 Zhang, W. *et al.* Kinetic pathways of ionic transport in fast-charging lithium titanate. *Science* **367**, 1030-1034 (2020).

136 Yue, Y. *et al.* Tailoring the Redox Reactions for High-Capacity Cycling of Cation-Disordered Rocksalt Cathodes. *Advanced Functional Materials*, 2008696 (2021).

137 Lun, Z. *et al.* Design principles for high-capacity Mn-based cation-disordered rocksalt cathodes. *Chem* **6**, 153-168 (2020).

138 Yang, W. & Devereaux, T. P. Anionic and cationic redox and interfaces in batteries: Advances from soft X-ray absorption spectroscopy to resonant inelastic scattering. *Journal of Power Sources* **389**, 188-197 (2018).

139 Achkar, A. J. *et al.* Bulk sensitive x-ray absorption spectroscopy free of self-absorption effects. *Physical Review B* **83**, 081106 (2011).
140 Luo, K. *et al.* Anion redox chemistry in the cobalt free 3d transition metal oxide intercalation electrode Li [Li0. 2Ni0. 2Mn0. 6] O2. *Journal of the American Chemical Society* **138**, 11211-11218 (2016).
141 Sathiya, M. *et al.* Reversible anionic redox chemistry in high-capacity layered-oxide electrodes. *Nature materials* **12**, 827 (2013).
142 Dai, K. *et al.* High Reversibility of Lattice Oxygen Redox Quantified by Direct Bulk Probes of Both Anionic and Cationic Redox Reactions. *Joule* **3**, 518-541 (2019).
143 Zhuo, Z. *et al.* Spectroscopic signature of oxidized oxygen states in peroxides. *The journal of physical chemistry letters* **9**, 6378-6384 (2018).
144 Tian, Y. *et al.* Promises and Challenges of Next-Generation “Beyond Li-ion” Batteries for Electric Vehicles and Grid Decarbonization. *Chemical reviews* (2020).
145 Manthiram, A. A reflection on lithium-ion battery cathode chemistry. *Nature Communications* **11**, 1-9 (2020).
146 Lun, Z. *et al.* Cation-disordered rocksalt-type high-entropy cathodes for Li-ion batteries. *Nature Materials*, 1-8 (2020).
147 Fisher, M. E. & Berker, A. N. Scaling for first-order phase transitions in thermodynamic and finite systems. *Physical Review B* **26**, 2507 (1982).
148 Nienhuis, B., Berker, A. N., Riedel, E. K. & Schick, M. First-and second-order phase transitions in Potts models: renormalization-group solution. *Physical Review Letters* **43**, 737 (1979).
149 Van der Ven, A., Deng, Z., Banerjee, S. & Ong, S. P. Rechargeable Alkali-Ion Battery Materials: Theory and Computation. *Chemical Reviews* (2020).
150 Zhong, P. C. *et al.* Increasing Capacity in Disordered Rocksalt Cathodes by Mg Doping. *Chemistry of Materials* **32**, 10728-10736, doi:10.1021/acs.chemmater.0c04109 (2020).